Production engine emission sensor modeling for in-use measurement and on-board diagnostics

by

Masoud Aliramezani

A thesis submitted in partial fulfillment of the requirements for the degree of

Doctor of Philosophy

Department of Mechanical Engineering
University of Alberta

Abstract

Production engine emission sensors have become essential for on-board measurement in the exhaust gas and for engine feedback control.

To help design future amperometric sensors, first the diffusion mechanism of a zirconia-based amperometric NO_x sensor was examined by studying the effect of sensor temperature on sensor output. The multi component molecular diffusion mechanism was experimentally found to be the dominant diffusion mechanism that affects the diffusive flow through the sensor diffusion barriers. A sensor model was developed based on this dominant diffusion mechanism to predict NO_x concentration which was validated with the experiments at different Diesel engine operating conditions with different species concentrations.

Then, a physics-based sensor model that includes diffusion and electrochemical submodels is developed. It is shown that NO is partly reduced in the O_2 sensing chamber which affects NO concentration in the O_2 sensing chamber and in the NO_x sensing chamber. Therefore, the electrochemical model is developed to simulate partial reduction of NO_x on the O_2 sensing electrode and reduction of NO_x on the NO_x sensing electrode. A transport model that simulates diffusion of the gas species through the sensor diffusion barriers and sensor chambers is coupled to the electrochemical submodels. Experiments at different engine operating conditions with different NO_x concentrations from 0 to 2820 ppm have been performed to validate the model accuracy at different operating conditions. The model results closely match the experiments with a maximum 12% error for the NO_x sensing pumping current.

Cross-sensitivity of electrochemical sensors to the other exhaust gas contaminations, especially NH_3, is still a challenge for the automotive industry. A dynamic NO_x sensor model is developed to remove ammonia cross sensitivity from production NO_x sensors mounted downstream of Diesel-engine selective catalytic reduction

(SCR) systems. The model is validated for large amounts of ammonia slip during different engine transients. A three-state nonlinear control oriented SCR model is also developed to predict the NH_3 concentration downstream of the SCR (NH_3 slip). NH_3 slip is then used as an input for modeling the cross sensitivity of a production NO_x sensor and calculating the actual NO_x concentration in the presence of NH_3 contamination.

A limiting-current-type amperometric hydrocarbon sensor for rich conditions (in the absence of O_2) is also developed. The transient performance and stability of the sensor are optimized by changing the sensor temperature, the reference cell potential, and the stabilizing cell potential at a high propane concentration (5000 ppm - balanced with nitrogen). Then, the sensor steady state behavior is studied to find the diffusion-rate-determined operating region. The sensor is shown to have a linear sensitivity to propane concentration from 0 to 3200 ppm. The sensor response time to different step changes from zero propane concentration to 5000 ppm propane concentration is studied. It is shown that propane concentration does not have a significant effect on the sensor response time.

Sensor and engine On Board Diagnostics (OBD) is the last part of this thesis. A physics-based model was developed and then employed to predict the sensor output for oxygen as a function of sensor temperature and oxygen concentration. A temperature perturbation method was also developed based on the model to calibrate the sensor output with respect to oxygen concentration. The model accurately matched the experimental results in steady state and transient. A two step sensor diagnostics procedure based on the sensor temperature perturbation method was then proposed. A self-calibration procedure was also implemented inside the diagnostics procedure using temperature perturbation at *engine-off*. This self-recalibration only requires an external relative humidity measurement.

Finally, based on experimental data, a Multi-Input Multi-Output (MIMO) control oriented diesel engine model is developed to predict engine NO_x emission and brake mean effective pressure (BMEP). The steady state engine NO_x is modeled as a function of the injected fuel amount, the injection rail pressure and the engine speed. The BMEP is assumed to be a function of the injected fuel amount and engine speed. Then, an engine dynamic model was developed by adding first order lags to the static NO_x and BMEP models. This two-state control oriented model is used to represent the dynamic model. The engine response to step changes of injection pressure and injected fuel amount are examined and compared with the experimental data. The developed control oriented model can be used for both engine and NO_x sensor on board diagnostics and for engine control with NO_x sensor feedback.

Acknowledgements

I am heartily grateful to my supervisor, Dr. Bob Koch, for his guidance, encouragement, and support through my years as a Ph.D. student. Apart from his valuable technical support, he helped me to improve my professional development skills by supporting me in being heavily involved with the University of Alberta governance and the Graduate Students' Association. He has always given me valuable advice for my future professional life and supported me to get a chance to teach an undergraduate course during my Ph.D. I appreciate everything he has done for me.

I am grateful to Dr. Bob Hayes for his technical support and Dr. Marc Secanell for his valuable comments during the model development phase of my thesis project.

Thanks to all my friends and colleagues who helped me in the last five years throughout this memorable journey with their kind supports. I would like to especially thank Bernie Faulkner, Giffin Symko, David Gordon, Kai Bailey, Kashayar Ebrahimi, Robert Klikach and Armin Norouzi.

I cannot thank my wife Alaleh Boroomand enough for her patience, care and support throughout my Ph.D. Lastly, I am heartily thankful to my parents Morteza and Masoumeh and my sister Yeganeh for everything they have done to support me since the time I decided to start this journey.

TABLE OF CONTENTS

List of Tables

LIST OF FIGURES

CHAPTER 1

INTRODUCTION

This Chapter details the motivation of this thesis as well as the problems addressed in this thesis and provides an overview of the solution.

1.1 Diesel engine main emissions

The high efficiency, fuel economy advantages at full-load and part-load conditions as well as the long lifetime of Direct Injection (DI) Diesel engines has made them interesting for power generation systems and particularly for the automotive industry [1, 2]. However, new engine control strategies and after treatment systems are needed to meet the stringent emission regulations [3–5].

1.1.1 Nitrogen oxides (NO_x)

The high combustion temperatures and the lean air-fuel mixture of Diesel engines leads to a relatively high NO_x emission. The NO_x emission in Diesel engines mainly consists of Nitrogen monoxide (NO) and Nitrogen dioxide (NO_2). Typically, the engine exhaust contains 70%-90% NO and 10%-30% NO_2 [6]. In the presence of Diesel Oxidation Catalyst (DOC) the NO_2/NO ratio increases after the DOC to approximately 1 [7].

1.1.2 Particulate matter (PM)

PMs are complex structures formed by soot, hydrocarbons (resulting from fuel and lubrication) and other minor materials [8]. The composition of PMs varies with the engine operating condition [9, 10]. PM emissions and NO_x emissions are connected by a tradeoff [11]. In general, PM concentration decreases when NO_x increases [12].

1.1.3 Carbon dioxide (CO_2)

Based on a study carried out in 2015, the top ten world CO_2 emitter countries were China, United States, India, Russia, Japan, Germany, South Korea, Iran, Canada, and Saudi Arabia, respectively, for which the overal contribution is more than two-thirds of the world CO_2 emission [13]. Road transport currently contributes about 20% of the European Unions (EU) total CO_2 emissions [14]. CO_2 formation is proportional to the fuel consumption and therefore, apart from the CO_2 emission regulations [15], CO_2 emission limits are also driven by the fuel economy demanded by the users. NO_x, PM and CO_2 are the most critical emissions of Diesel engines [16].

1.1.4 Carbon monoxide (CO)

CO is a colourless, odourless, non-irritating but highly toxic gas which is a sub-product of the combustion [17, 18]. Diesel engines typically operate at lean condition (higher air-fuel ratio than the stoichiometric air-fuel ratio), therefore, CO emission is a less critical emission than NO_x and PM, although it is still one of the most important emissions of Diesel engines [19].

1.1.5 Unburned Hydrocarbon (UHC)

UHCs are a product of an incomplete combustion of the injected fuel due to low temperature or locally or globally rich conditions inside the cylinder [20]. This includes non-burnt HC and partially oxidised HC. Typically, the UHC and CO emissions increase and decrease with each other in a Diesel engine [21].

1.2 Spark Ignition (SI) engine main emissions

For SI engines the primary pollutants are NO_x, (primarily nitric oxide, NO), CO and UHCs [22]. In addition, the PM emission of direct injection SI engines is also high and critical [23, 24]. Similar to Diesel engines, CO_2 emission represents the engine fuel consumption, although this relation is also a function of fuel type [22, 25].

Three-Way Catalyst (TWC) is a proven aftertreatment system that significantly reduces UHC, CO and NO_x emissions of SI engines that work with stoichiometric air-fuel ratio [26]. Although aftertreatment systems of SI engines are not the focus of this research, the emission measurement methods discussed here can be used for Diesel or SI engines and other applications.

1.3 Motivation

The main objective of this research is to understand the working principle of the existing production amperometric sensors used in the automotive industry and to develop new sensors with different sensitivities by only changing the sensor operating parameters. The results of this research help to reduce the sensor cross sensitivity to undesired species (such as NH_3) and to increase the sensor sensitivity to desired species (such as NO_x and unburned hydrocarbons).

1.3.1 Emission regulations for Diesel and SI engines

The second phase of EPA regulation for on-board diagnostic (OBD-II) requires monitoring the performance of aftertreatment systems and turning on the Check Engine light if the tailpipe emission levels remain 50 % higher than the standard for more than a specific period of time [3]. Maintaining emission standards has become increasingly difficult due to the stringent emission regulations [26].

The National Highway Traffic Safety Administration (NHTSA) and the Environmental Protection Agency (EPA) have recently issued regulations to reduce vehicular emissions for vehicles manufactured by the end of 2025. The EPA regulations limits production of CO_2 to less than 101.3 g/km (163 g/mile) of which is equivalent to an average fuel consumption of 4.32 L/100 km (54.5 mpg) [27]. The stringent regulations also strictly limit the NO_x and particulate emissions [3].

EU Non-Road Mobile Machinery (NRMM) Stage V, introduced a limit on the number of particles (PN) of 1 [$\times 10^{12}$/kW.hr] equivalent to a particulate mass limit of 15 mg/kW-hr for land-based engines with output power between 19 and 560 kW [28]. The NO_x limit for the main engine category remains unchanged compared with Stage IV at 400 [mg/kW.hr] while for engines with output powers higher than 560 kW, must be lower than 3.5 [g/kW.hr].

1.3.2 The need of on-board emission measurement in combustion engines

According to the stringent emission regulations [29, 30], any fault in any emission-relevant device must be detected and reported through on-board diagnostics (OBD) [31]. The first OBD standard was passed as a law in 1970 by the US congress to reduce the adverse effect of vehicular emissions on the environment [32]. In 1996, an updated standard (OBD II) was introduced. OBD II standard mandates monitoring of any electronic powertrain system or component that provides input to, or receives commands from the electronic control unit (ECU) [31].

Real-time measurement of the actual engine-out and tailpipe emissions has become essential for engine combustion control and for exhaust aftertreatment systems efficiency [33, 34]. As a case in point, high NO_x and particulate matter emissions are challenges of meeting emission standards with Diesel engines [3–5]. Exhaust Gas

Recirculation (EGR) [35, 36], Selective Catalytic Reduction (SCR) system [36, 37] and Low Temperature Combustion (LTC) [38, 39] are the most effective methods to control and reduce $\mathrm{NO_x}$ emissions and realtime emission measurement plays a pivotal role in improving the performance of these systems [40]. Exhaust gas sensors are used upstream and/or downstream of after-treatment systems to monitor their performance and efficiency [32, 41]. To meet increasingly stringent emission standards, the accuracy of the emission sensors also needs to be increased [42–46]. This requires reliable on-board diagnostics of emission sensors in addition to the other aftertreatment components.

Finally, many experimental studies have shown that the actual vehicular emissions can be much higher than the emission levels passed through standard certification tests. For instance, more than half of the randomly selected Euro 6 diesel cars tested with Exhaust Gas Recirculation (EGR) or Selective Catalytic Reduction (SCR) systems, had $\mathrm{NO_x}$ emissions six times higher than the certified level [47]. Another study showed that out of three tested vehicles, the best (urea-SCR) was 3-4 times higher than the certified level in portable emissions measurement system (PEMS) testing while the highest actual emission was 5-7 times higher than the certified level [48]. The European Commission has agreed to use portable emissions measurement system for measuring the actual emissions for diesel $\mathrm{NO_x}$ and Gasoline Direct Injection (GDI) PN [49].

1.3.3 Thesis outline

The remainder of this thesis is organized as follows:

- Chapter 2 provides a background on Diesel exhaust gas aftertreatment and electrochemical sensors.
- Chapter 3 details the experimental setup used for engine testing and sensor

testing including emission measurement equipment.

- Chapter 4 describes the diffusion mechanism in the NO_x sensor as a function of sensor temperature and is partially based on publication [50].
- Chapter 5, provides a more detailed electrochemical model of the amperometric NO_x sensor and is based on [51].
- Chapter 6 investigates cross sensitivity of the NO_x sensor to ammonia and converting the NO_x sensor to measure HC and looking at cross sensitivity to NO_x and O_2. This chapter is based on publication [33], [52] and [53].
- Chapter 7 utilizes the NO_x sensor for diagnostics and is based on publications [54] and [55].
- Finally in chapter 8 conclusions are drawn.

1.3.4 Contributions

To summarize, the main contributions of this thesis are:

1. Setting up a medium duty Diesel engine for experimental analysis.
2. Developing a comprehensive physics-based model of an amperometric NO_x-O_2 sensor.
3. Developing a sensor test rig where 6 gases can be mixed using mass flow controllers which control the flow over the sensor.
4. Converting the NO_x sensor a variable-potential limiting-current-type amperometric hydrocarbon sensor to measure propane concentration in rich condition.
5. Investigating cross sensitivity of the NO_x sensor to ammonia using an SCR model.

6. Investigating the effect of operating parameters of an amperometric NO_x-O_2 sensor on the sensor response.
7. Developing a phenomenological sensor diagnostics strategy used for diagnosing sensor errors and for recalibrating the sensor at engine off.
8. Developing a Diesel engine control oriented NO_x emission model to be used for feedback control and On-Board Diagnostics (OBD).

The journal papers and conference papers that resulted from this work are listed in Appendix A.

CHAPTER 2

BACKGROUND

This chapter provides an overview of the topics of this thesis that are discussed in the context of research in the literature.

2.1 Diesel Exhaust Aftertreatment

2.1.1 Diesel Particulate Filter (DPF)

Diesel Particulate Filters (DPF)s are used to trap particulate matters (PM) from the exhaust gas and to increase the reactivity of the trapped particles during DPF regeneration [56]. DPFs are capable of removing more than 90% of the PMs [57]. DPF physically filters the PMs which consequently increases the pressure drop over the filter. The increase of pressure drop increases engine back pressure and reduces the engine thermal efficiency [58]. To compensate this effect, the PMs should be removed by reacting and burning them through a DPF regeneration process.

Active regeneration and passive regeneration are the two main methods of removing PMs from the DPF [59, 60]. Active regeneration is achieved by periodically increasing the exhaust gas temperature to more than 550°C by fuel post-injection [59]. On a production vehicle, active DPF regeneration is done every few minutes during a normal urban driving cycle [61, 62]. Passive regeneration takes place on a catalyst-coated DPF where PMs are oxidized on the surface of the catalyst with O_2 and NO_2 [60].

2.1.2 Diesel Oxidation Catalyst (DOC)

Diesel Oxidation Catalyst (DOC) is a honeycomb monolith catalyst that is used to oxidize CO and HCs. The DOC also regulates NO/NO_2 ratio in the exhaust gas. The DOC's honeycomb shaped monolith is usually washcoated with Pt or Pt/Pd on an Al_2O_3 support, with CeO_2 and zeolite components [63–65].

The reactions details inside the DOC are complex and not fully understood due to the complicated species interactions and the numerous intermediary reactions [66].

2.1.3 Selective Catalytic Reduction Catalyst (SCR)

Urea-based Selective Catalytic Reduction (SCR) is an effective technique to reduce the NO_x emissions and to satisfy future emission standard regulations [67, 68]. A schematic of an SCR system is shown in Figure 2.1. The 32.5% urea solution (*AdBlue* or *Diesel Exhaust Fluid*) is injected into the upstream of the catalytic converter. The amount of injected Adblue is determined using open-loop or closed-loop SCR control strategies that can include NO_x and/or ammonia (NH_3) sensors for control strategies [69–71].

2.1.3.1 Chemistry of the De-NOx SCR process

The main NO_x reduction reactions of SCR are described as [72]:

$$4NH_3 + 4NO + O_2 \rightarrow 4N_2 + 6H_2O \tag{2.1}$$

$$2NH_3 + NO + NO_2 \rightarrow 2N_2 + 3H_2O \tag{2.2}$$

$$8NH_3 + 6NO_2 \rightarrow 7N_2 + 12H_2O \tag{2.3}$$

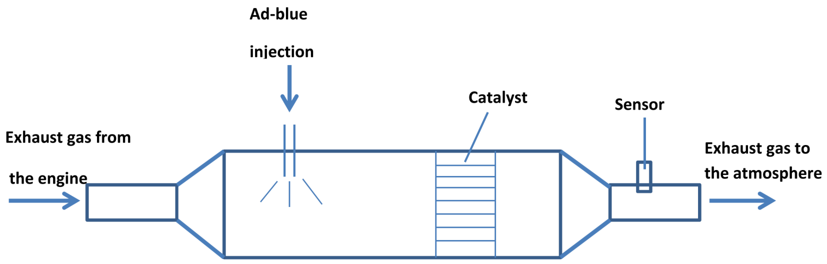

Figure 2.1: SCR system schematic

NO is the dominant component of the engine-out NO_x emission and in the absence of DOC, the NO concentration would be more than 90% of overall exhaust NO_x (10% NO_2 - this ratio also depends on the engine operating condition) [7]. The reaction rate of Eqn. (2.1) is considered fast, so it is called the standard SCR reaction. Eqn. (2.2) is also called a fast SCR reaction, typically the fastest and the most preferred NO_x reduction reaction [73]. A DOC increases the amount of NO_2 by the following reaction:

$$2NO + O_2 \rightarrow 2NO_2 \tag{2.4}$$

If the DOC is placed upstream of the SCR and if the amount of NO_2 is increased above a NO_2/NO ratio of one, then the slow reaction of Eqn. (2.3) takes place [73].

Measuring the NO_x concentration in the exhaust gas is essential for closed-loop control of SCR systems [69, 74, 75]. However, the commercial NO_x sensors are cross-sensitive to ammonia (NH_3). Therefore, the NO_x sensor reading can differ from the actual value [76]. Determining the actual NO_x concentration is a challenge for controlling urea injection of SCR systems.

Cross sensitivity of commercial NO_x sensors to NH_3, makes it difficult to achieve maximum NO_x conversion in SCR control. Further, the time delay in the urea or ammonia injection and SCR catalyst dynamics are the other important factors that limit the performance of closed-loop SCR control [77].

2.2 Electrochemical gas sensors

The non homogeneous air-fuel mixture increases particulate matters [78] and the high temperature inside the combustion chamber of Diesel engines increase the NO_x [3, 79]. Different methods have been developed to reduce NO_x emissions, including Exhaust Gas Recirculation (EGR) [80], selective catalytic reduction (SCR) system [7] and Low Temperature Combustion (LTC) [38]. New engine control strategies and after treatment systems are needed to meet increasingly stringent NO_x and particulate emission regulations [3]. In-use sensors that continuously monitor emissions are used in real-time feedback for combustion control to minimize the engine-out emissions produced during the combustion process [81]. In addition, measuring the actual NO_x concentration is essential for urea injection control of SCR systems but because of the cross sensitivity of NO_x sensors to NH_3[33], it is difficult to achieve the maximum NO_x conversion in SCR closed-loop control [69, 82].

Solid-state electrochemical gas sensors have many remarkable properties that make them of special interest for a variety of applications such as automotive [33, 83], biotechnology [84, 85], medical [86] and many other industries [87–89]. The reliability, small size, fast response and low price of solid-state electrochemical sensors make them ideal for automotive industry [54, 90, 91]. Potentiometric gas sensors, mixed potential gas sensors, impedancemetric gas sensors and amperometric gas sensors are the main types of electrochemical gas sensors. The working principle and the characteristics of each type of gas sensors are explained next.

2.2.1 Potentiometric gas sensors

The operating principles of potentiometric gas sensors is based on thermodynamic kinetics and concentration gradients of species between a reference electrode and a working electrode. Species or multi-phase mixtures that create a constant electrochemical activity are used as the reference electrochemical cell. Therefore, it is essential to isolate the reference electrode from the measuring gas [92, 93].

For instance, when a solid electrolyte (e.g. Yttria-Stabilized Zirconia, YSZ) is exposed to an environment with partial pressure of oxygen equal to p_{O_2}, the following reaction takes place at the three-phase boundary (TPB) between the gas (g), the electrolyte (YSZ) and the electrode (Pt) [94]:

$$O_2(g) + 4e^-(Pt) \rightleftharpoons 2O^{2-}(YSZ) \tag{2.5}$$

The electromotive force (emf) between electrodes is expressed by the Nernst equation [95]:

$$emf = \frac{\bar{R}T}{4F} ln\left(\frac{p_{O2,s}}{p_{O2,ref}}\right) \tag{2.6}$$

where $p_{O2,s}$ and $p_{O2,ref}$ are the partial pressure of O_2 in the sample gas and the reference gas, $\bar{R}$ is the gas constant, T is temperature in K, and F is the Faraday constant. Typically a reference gas mixture provides a constant oxygen partial pressure on the reference electrode for a given temperature. Knowing the partial pressure of O_2 at the reference side, the partial pressure of O_2 in the sample gas can be determined using Eqn. (2.6). This is the working principle of a potentiometric O_2 sensor. A similar approach can be used to measure the concentration of any electrochemically active species.

2.2.1.1 Mixed potential gas sensors

A mixed potential gas sensor is a specific type of potentiometric gas sensor that consists of two electrodes that have different catalytic activity and are exposed to the same measuring gas. The different catalytic activities of the electrodes create different steady state potential from the electrochemically active species. The resulting potential difference is used to measure the concentration of specific species. The main advantage of mixed potential sensor is that the sensor does not need a perfectly isolated reference electrode [96].

2.2.2 Impedancemetric gas sensors

Impedancemetric gas sensors measure the sensor impedance spectroscopy over a range of frequencies (AC measurements) to measure concentration of specific species [97, 98]. The impedance spectroscopy has been a promising technique to measure species concentration by investigating the effect of frequency on the individual components of the sensor electrochemical cell.

If the electrolyte, electrode-electrolyte interface and the bulk reactions that take place inside the sensor chambers have sufficiently different time constants, the effect of cell potential frequency on these components can be distinguished by impedance spectroscopy [99].

Impedancemetric YSZ gas sensors has been reported to have sensitivity to NO_x [98, 100, 101], water vapor [102], combustible hydrogen-containing gases [103], CO [98, 104], and hydrocarbons [98, 105].

Most of the impedancemetric sensors are operated in low frequencies (< 100 Hz) since the sensor response for different species at different concentrations overlap in high frequency range [98].

2.2.3 Amperometric gas sensors

Solid electrolyte amperometric sensors are used for on-board exhaust measurement of the NO_x concentration at wet condition and this makes them ideal for combustion engine emission measurement systems [106]. Amperometric sensors are increasingly used in commercial combustion engines to meet the stringent emission regulations [40]. They are used in conjunction with combustion improvement methods for thermal efficiency and engine emission reduction [25, 38, 107]. Amperometric sensors generate an output that is linearly dependant on the concentration of the measuring gas, which makes them suitable for detecting high gas concentrations [50, 87].

In general, both the electrode reactions inside the sensor chambers and the diffusion of exhaust gas species through the sensor diffusion barriers affect the sensor output [108, 109]. When the sensor reaction dynamics are much faster than the diffusion of species into the sensing chambers, the sensor is called limiting current type [110]. In this case, the sensor output is proportional to the diffusion of species through the sensor barriers into the sensor chambers. The diffusion mechanism of species through an amperometric NO_x sensor has been found to be the normal multi-component diffusion mechanism through the sensor diffusion barriers [50].

The effect of electrochemical properties of electrodes on the sensing behavior of solid state electrochemical gas sensors has been studied in detail [111–114]. The sensitivity of amperometric sensors to gas species and the reliability of these sensors are directly affected by electrochemical properties [115]. These properties include electrode material [116–118], electrode potential [119], electrolyte properties [120–122] and properties of the diffusion barrier [50, 54, 123, 124].

Typical current-voltage response of an amperometric sensor as the cell voltage (V_P) is varied [50, 125, 126] is shown in Figure 2.2 for a NO_x sensor. A detailed description and schematic of sensor is given later in the thesis. The response is divided into six regions that depend on the sensing cell voltage. In region I, the cell voltage is lower than the reversible potential and not high enough to cause reduction of species on the cathode. Therefore, the reverse reaction (oxidation) takes place causing a negative cell current. When the cell voltage is just above the reversible potential, activation polarization becomes the rate-determining step. This phase is labeled as region II. In region III, the cell current varies almost linearly with voltage, based on Ohm's law. In this region, the Ohmic loss dominates the cell voltage-current relation. As the cell voltage increases further, the current-voltage relation becomes non-linear in region IV and then the cell current finally reaches a saturation level determined by the diffusion rate of oxygen into the chamber (region V). In region V the pumping rate of (O^{2-}) ions from the cell has reached its maximum level since all available reducible molecules are being reduced on the cathode as soon as they reach the electrode surface. The transition phase from ohmic behavior to the limiting current region is marked as region IV.

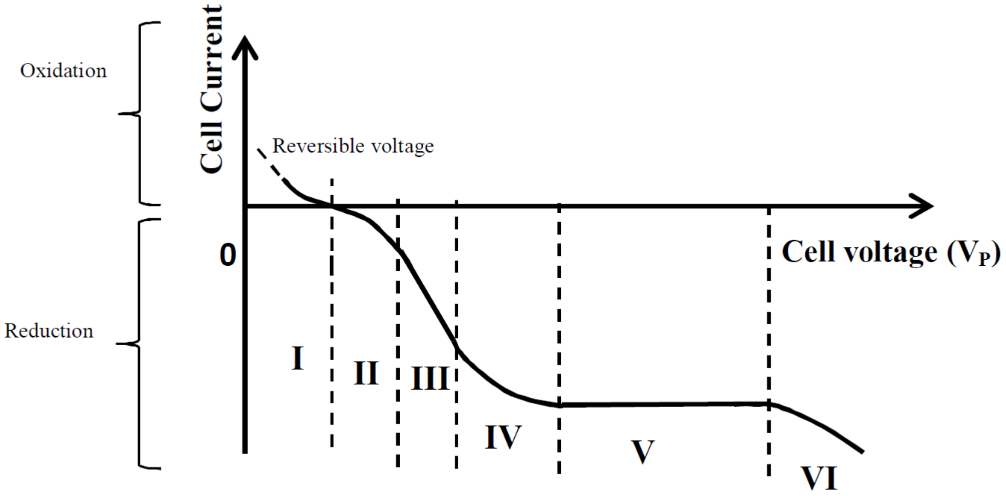

Figure 2.2: Typical electrode current vs potential relation

Further increases in the cell voltage, results in the partial pressure of the reduced species (in this case, NO) to become lower according to Nernst equation [95]. If the partial pressure of the reduced species (NO) decreases to less than a certain value ($\approx 10^{-33}$ atm), electrolyte decomposition takes place [127]. This causes a further increase in the O^{2-} pumping rate and therefore the cell current increases (region VI) which can potentially damage the sensor. The sensor behavior in this region is not studied in this work as it is not useful when measuring NO_x.

This thesis is focused on amperometric gas sensors to provide a deeper understanding of the working principles and performance of this type of electrochemical gas sensors. The goal is to use production sensors, which are readily available and only modify the inputs to the sensor.

Chapter 3

Experimental Setup

This Chapter details the experimental setup used and includes a detailed explanation of the Diesel engine, the Spark Ignition engine, the sensor test rig setup, the Fourier-Transform Infrared Spectroscopy (FTIR) and the amperometric NO_x-O_2 *sensor. The experimental data is used for sensor model and engine model validation.*

3.1 Sensor and interfaces

The sensors used in the experiments were all production Bosch sensors with ECM electronics [128]. Most of the experimental studies are carried out on an ECM NO_x sensor (P/N: 06-05). The sensor parameters and operating condition were changed using the corresponding control module (*ECM-NOxCANt* P/N: 02-07). The *ECM-NOxCANt*, Type T Module (NOxCANt) is an integratable NO_x, O_2 and λ measurement system than can be used on combustion systems, all engine types and the corresponding aftertreatment systems. The *NOxCANt* is connected to the electrochemical NO_x sensor mounted on the engine exhaust pipe or on the sensor test rig. The module facilitates measuring the sensor output current, for O_2 and NO_x and controls all the main sensor parameters such as the sensor temperature and the sensing cell voltages. The sensor and the control module are shown in Figure 3.1. The module specifications are listed in Table 3.1

Figure 3.1: ECM production NO_x sensor and the corresponding control module

The module and the sensor(s) are connected via Controller Area Network (CAN bus[1]).

The sensor calibration information is stored in memory chips located in the sensor connectors. This facilitates sensors recalibration to ensure accurate and verifiable measurement of emissions concentration. A PC software (ECM Configuration tool, shown in Figure 3.2) is used to set-up the sensor, view output variables, calibrate the sensor and change the sensor operating parameters. It should be noted that not all the sensor operating parameters can be changed through CAN bus and the corresponding PC software. For some tests the module hardware was modified to change some of the sensor operating parameters.

The sensor controller module is connected to a PC via *Kvaser Light HS* CAN

---

[1] CAN is a multi-node, multi-master serial communication standard for connecting different electronic devices (also called nodes) to each other. A minimum of two nodes are required for the CAN network to work. The node can be a simple sensor or an actuator or a complex control unit such as engine electronic control unit (ECU) [130]. All nodes are connected to each other through a two-wire bus. The wires are typically shielded to reduce the electrical noise [131]

Table 3.1: ECM-NOxCANt module specifications [129]

Input	ECM Amperometric NO_x sensor
Ranges	NO_x: 0 to 5000 [ppm], λ (Lambda): 0.40 to 25, AFR: 6.0 to 364, O_2: 0 to 25 [%]
Accuracies	NO_x: ± 5 [ppm] (0 to 200 [ppm]), ± 20 [ppm] (200 to 1000 [ppm]), ± 2.0 % (elsewhere)
Response Time	Less than 1 s for NO_x. Less than 150 ms for λ, AFR, O_2
Fuel Type	Programmable H:C, O:C, N:C ratios, and H_2
CAN	High Speed according to ISO 11898
Configuration	Via CAN Bus with Configuration Software. Programmable Node ID.
Module	145mm × 120mm × 40mm, Environmentally Sealed
Environmental	-55 to +125^{o}C for the module, 950^{o}C (maximum continuous) NO_x sensor
Power	11 to 28 VDC, 1.2A at 12V (steady-state), 4A at 12V for 30s (start-up)

interface (shown in Figure 3.3). The interface is connected to the PC through a USB port.

3.2 Internal Combustion Engines

To study the sensor behavior over a wide range of exhaust emission concentrations, the sensor is mounted in the exhaust pipe of a four cylinder medium duty Tier III diesel engine (Cummins QSB 4.5 160) and in the exhaust pipe of a four cylinder port injection spark ignition engine fueled with natural gas (GM Vortec 3000) as shown in Figure 3.4. To measure the engine raw emissions, the emission sensors were installed upstream of the engine aftertreatment systems .

3.2.1 Diesel engine setup

The Diesel engine used in the experimental studies is a 4 cylinder medium duty diesel engine (Cummins QSB4.5 160 - Tier 3/Stage IIIA), shown in Figure 3.5. The Engine characteristics are listed in Table 3.2.

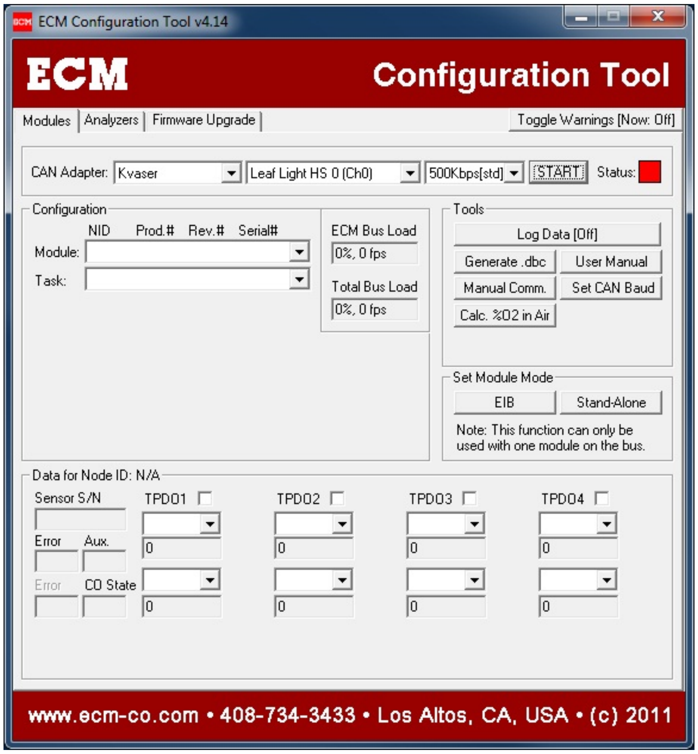

ECM Configuration Tool v4.14

CAN Adapter: Kvaser

Leaf Light HS 0 (Ch0)

500Kbps[std]

ECM Bus Load: 0%, 0 fps

Total Bus Load: 0%, 0 fps

Note: This function can only be used with one module on the bus.

Data for Node ID: N/A

www.ecm-co.com • 408-734-3433 • Los Altos, CA, USA • (c) 2011

Figure 3.2: PC software used to connect to sensor modules

Table 3.2: Diesel engine characteristics [132]

Engine type	In-Line, 4-Cylinder
Displacement	4.5 L
Bore × Stroke	102 mm × 120 mm
Peak Torque	460 lb-ft (624 Nm) @ 1500 rpm
Peak power	165 hp (123kW) @ 2000 rpm
Aspiration	Turbocharged and Charge Air Cooled
Certification Level	Tier 3 / Stage IIIA

3.2.1.1 Cummmins Engine Control Unit (ECU)

The Cummmins ECU (Fig. 3.6a) controls the Diesel engine by reading the stock sensors mounted on the production Cummins engine including the intake manifold temperature, intake manifold pressure, injection rail pressure, coolant temperature, etc and controlling all of the engine main actuators and operating parameters, includ-

Figure 3.3: *Kvaser Light HS* CAN interface

ing but not limited to the injection timing(s), turbocharge boost pressure, injection amount. To monitor and record the engine main variables and operating parameters, the ECU is connected to a computer using a J1939 connector (Fig. 3.6b) and a hardware interface (INLINE 6 - Fig. 3.6c).

3.2.1.2 Intake manifold temperature controller

To examine the engine performance and emissions in a repeatable fashion, it is essential to maintain constant intake manifold air temperature. Since the intake manifold air temperature is strongly effected by the engine boost, small changes in atmospheric pressure, room temperature and other effects change the intake manifold temperature. Thus, a PID controller[2] (Fig. 3.7a) in which the intake manifold temperature, measured with a thermocouple, is used to control the water flow rate of the intercooler (Fig. 3.7b). An electronically controlled proportioning valve[3] (Fig. 3.7c) is the actuator that varies the water flow rate of the intercooler.

---

[2] `http://www.omega.ca/pptst_eng/CNI8_SERIES.html`

[3] `http://www.omega.ca/pptst_eng/PV14.html`

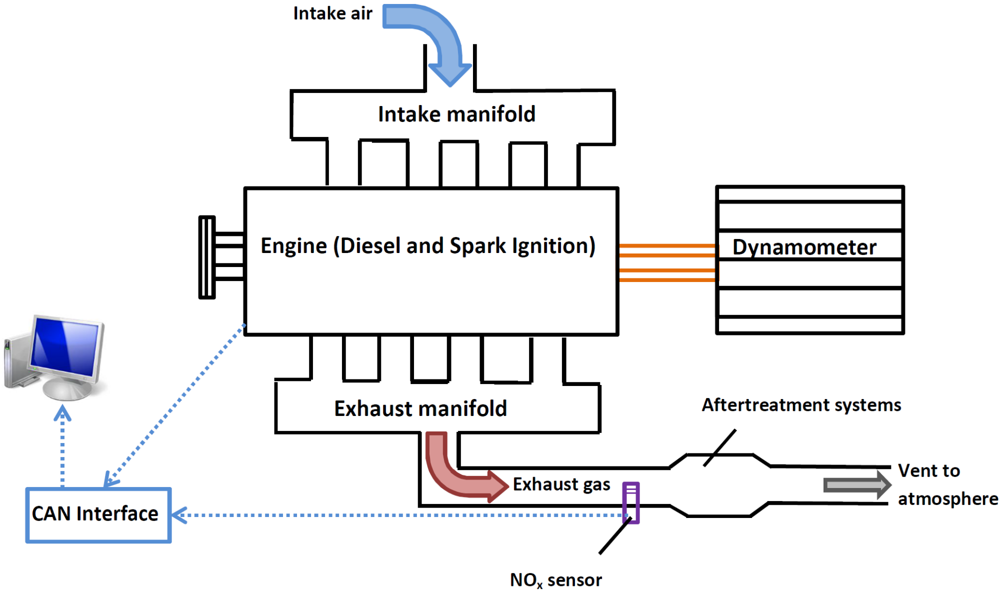

Figure 3.4: Experiment setup - Internal Combustion Engines

3.2.1.3 SOFTWARE

INSITE Pro - Cummins software is used for reading and logging the engine ECU data. A limited number of engine parameters can also be modified and then downloaded to the ECU using this software. A National Instruments data acquisition interface (NI9213) is part of the Dyne Systems 1014W eddy current dynamometer. *Labview* is used to log the engine data (thermocouples and the pressure drop sensor output) from Dyno at 1 Hz.

3.2.1.4 SENSORS

Thermocouples: the exhaust gas temperature is measured at several points including right after the engine, upstream and downstream of the catalysts. The thermocouples used are *OMEGA 20G K-Type* connected to the PC via a NI9213 analog input interface and are read using LabView.

Differential pressure sensor: the pressure drop over catalysts is measured by an automotive differential pressure (Dp) sensor (Ford DPFE-22 - Fig. 3.8a). The Dp sensor

Figure 3.5: Diesel engine setup

has a voltage output which is linearly dependant to the pressure drop over the two sensor inputs. This sensor has an analog output and measures the differential pressure between 0 - 30 kPa. The sensor taps are located 0.15 m upstream and downstream of the DOC on the exhaust. The differential pressure sensor was calibrated and the following relationship was found between the output voltage, V_{DPout} [V] and the differential pressure, ΔP [kPa] [133],

$$\Delta P = 2.7185 V_{\text{DPout}} - 6.9283 \; (\pm 0.136) \tag{3.1}$$

The output voltage from the pressure sensor is measured using a NI9205 analog input module and collected by a computer using LabView with a sampling rate of 1 Hz. Since the sensor tests are all carried out at engine steady state condition, a 1 Hz sampling rate is sufficient.

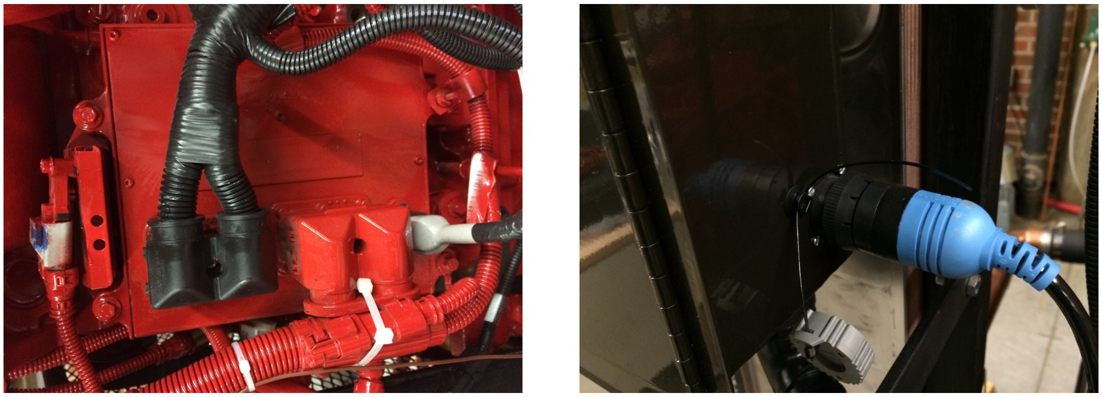

(a) Cummins ECU

(b) J1939 connector

(c) INLINE6 interface

Figure 3.6: Engine control unit

Intake air flow meter: the intake air flow rate is measured using a Hot Film Mass flow sensor (HFM) (Fig. 3.8b). This sensor is a stock Ford sensor with part number of AFLS-166. The sensor has frequency output that increases with the flow rate and is measured using a frequency counter. The relation between the flow rate and the sensor frequency output depends on the intake air pipe diameter and length. To find this dependence, the HFM sensor is mounted on the intake pipe and calibrated using a certified flow meter test bench as shown in Fig. 3.9. The air intake pipe is 0.61 m long and with diameter of 0.10 m and is connected upstream of the engine turbocharger. The HFM is located 0.30 m from the entrance of the inlet tube. After sensor calibration, the following relation is found between the volumetric air flow rate,

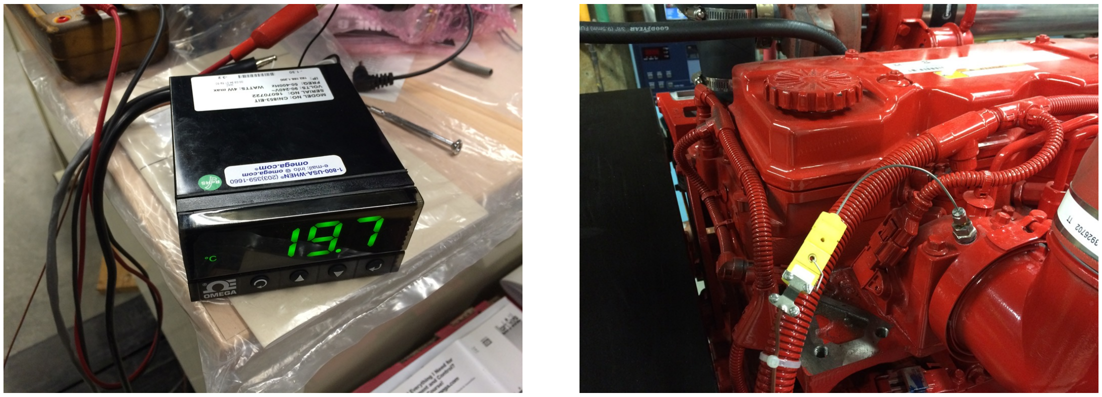

(a) External temperature PID controller module (Omega CNi8 series)

(b) Intake manifold thermocouple for intake air temperature

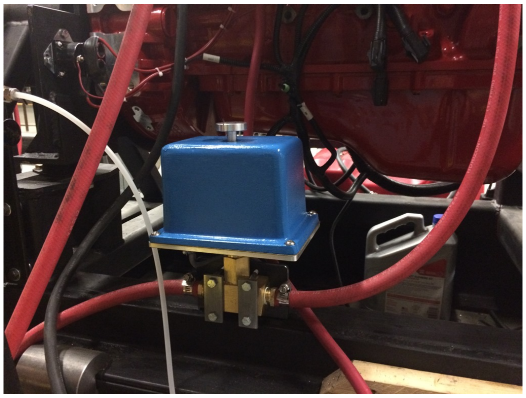

(c) Electronically Controlled Proportioning Valve

Figure 3.7: Intake manifold temperature controller

$\dot{Q}_{air}$ [cfm], and the sensor output frequency, f [Hz], at 20°C [133]:

$$\dot{Q}_{air} = 1.6169 f^{2.7551} \ (\pm 11) \tag{3.2}$$

3.2.1.5 Ammonia injection system

To study the NO_x sensor cross sensitivity to ammonia, an ammonia injection system was developed and mounted on the Diesel engine exhaust system as shown in Fig. 3.10. To inject ammonia into the exhaust system, compressed air is injected to the bottom

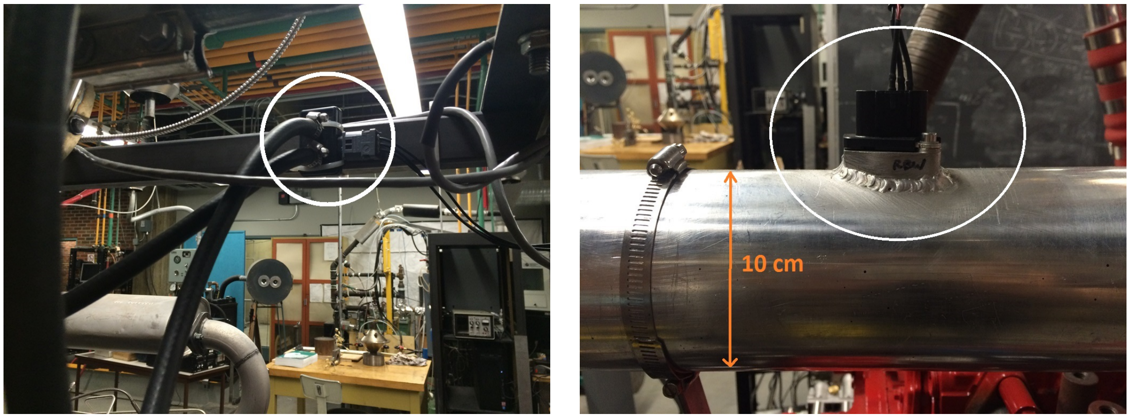

(a) Differential pressure sensor (b) Hot film mass flow sensor (HFM)

Figure 3.8: Flow sensors

of the aqueous ammonia tank. After bubbling the aqueous ammonia solution, the resulting NH_3 gas comes out of the top of the tank and is injected into the exhaust gas. More details about the design of the ammonia injection system is available in [133].

3.2.2 SI engine setup

To examine the sensor performance in a wider range of engine exhaust emissions, the same sensor is mounted on the exhaust pipe of a four cylinder port injection spark ignition engine (GM Vortec 3000, shown in Figure 3.11). The engine is fueled with natural gas. The engine specifications are listed in Table 3.3.

Table 3.3: SI engine characteristics [134]

Engine type	In-Line, 4-Cylinder
Displacement	2966.6 cc
Bore × Stroke	101.60 × 91.44 mm
Fuel type	Gasoline, Propane or Natural Gas
Peak Torque	163 lb-ft @ 1600 rpm (Gasoline), 147 lb-ft @ 1600 rpm (Propane), 139 lb-ft @ 1600 rpm (Natural Gas)
Peak power	83 hp @ 3000 rpm (Gasoline), 75 hp @ 3000 rpm (Propane), 71 hp @ 3000 rpm (Natural Gas)

Figure 3.9: Flow meter test bench - Hot film mass flow sensor (HFM)

3.3 Gas mixture test rig

To experimentally study the exhaust gas sensor behavior in the presence of different gas species at controlled concentrations, a sensor test rig was built based on a design from ECM [128]. The test rig consists of six externally-controlled 2-way valves, three externally-controlled 3-way valves, four humidifying tanks and six CCR MKS-GE50A mass flow controllers, connected to gas cylinders filled to known concentrations. All of the control valves are externally commanded by a PC using digital outputs from an Arduino interface as schematically shown in Figure 3.12. Several gas mixtures at different species concentrations are used to test the sensor.

3.3.1 Sensor test rig components

PFA Tubing: 1/4" *FABCO PLASTICS* PFA tubing was used to connect the gas cylinders to the valves and to connect the sensor test rig components to each other.

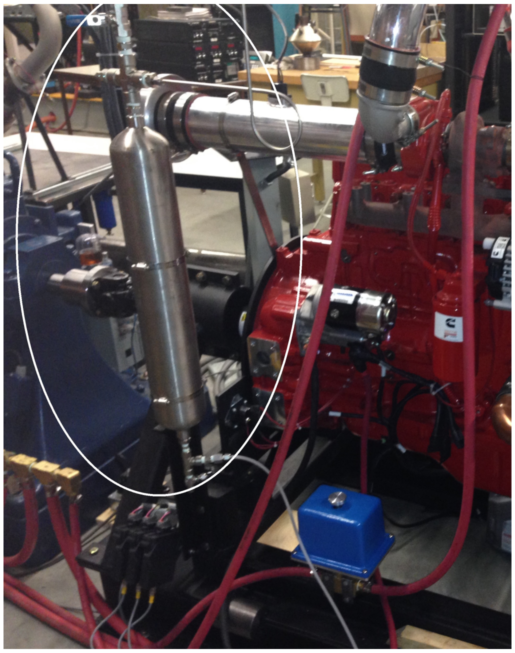

Figure 3.10: Ammonia injection system

Two-way Valves: Six externally controlled solenoid two-way valves (SWAGELOK SS-42S4-41DC) are used in the setup to connect the gas tanks to the mass flow controllers.

Three-way Valves: four externally controlled solenoid three-way valves (SWAGELOK SS-42GXS4-41DCX) are used to control the gasses before they are mixed. OMEGA solid state relays are used to actuate the three-way valves and the two-way valves with an ARDUINO interface.

Mass flow controllers: one 10 slm mass flow controller (MKS GE50A0xxx04SBV020) is used to control the flow of nitrogen through the sensor test rig and five 2000 sccm mass flow controllers (MKS GE50A0xxx03SBV020) are used to control the flow of other gas species through the sensor test rig. The mass flow controllers are connected to a PC through LAN connection through a LAN HUB. The mass flow controllers

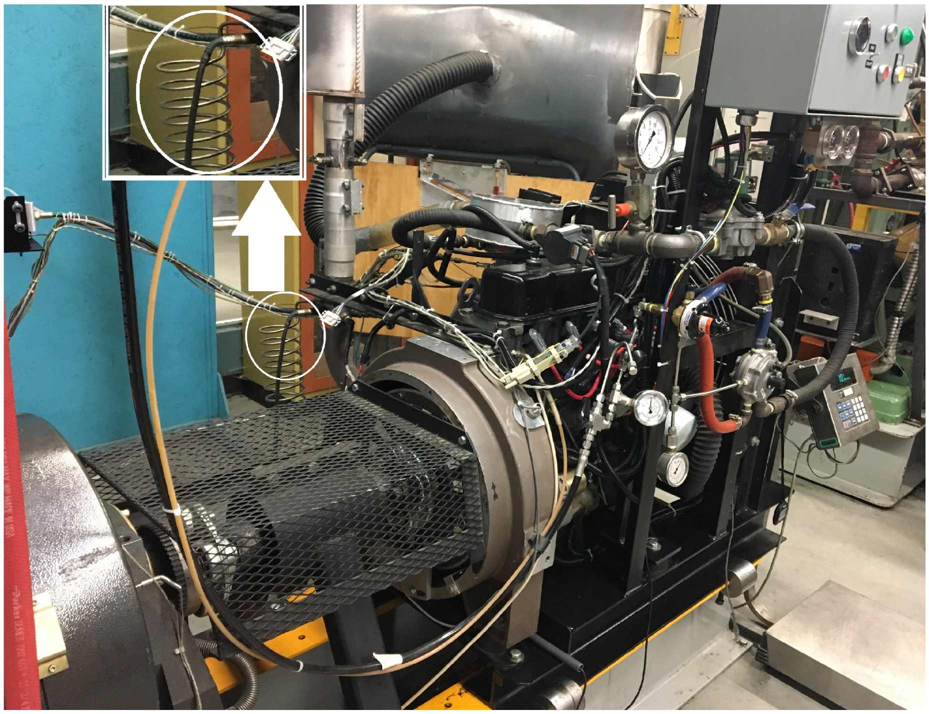

Figure 3.11: Spark ignition engine setup including closeup of NO_x sensor on exhaust.

are fully controlled through a MATLAB GUI program developed for this purpose.

Bubbler tanks: four commercial automotive tanks (Canton Racing Products - 80-211) are modified and then used to humidify the gases if necessary to simulate the combustion products inside the engine exhaust gas. The desired gases are first injected into the water from the bottom of the bubbling tank and the resulting humidified gases are injected to the line from the top of the tanks.

Tank heaters: four Screw Plug Immersion Heaters (OMEGA RI-250/120V) are used to heat the water inside the tanks to keep the vaporization rate constant.

Line heaters: four silicone rubber tape heaters are used to heat the tubes downstream of the tanks to avoid water vapor condensation in the lines. It is critical to keep the line temperature high enough and avoid water vapor condensation not

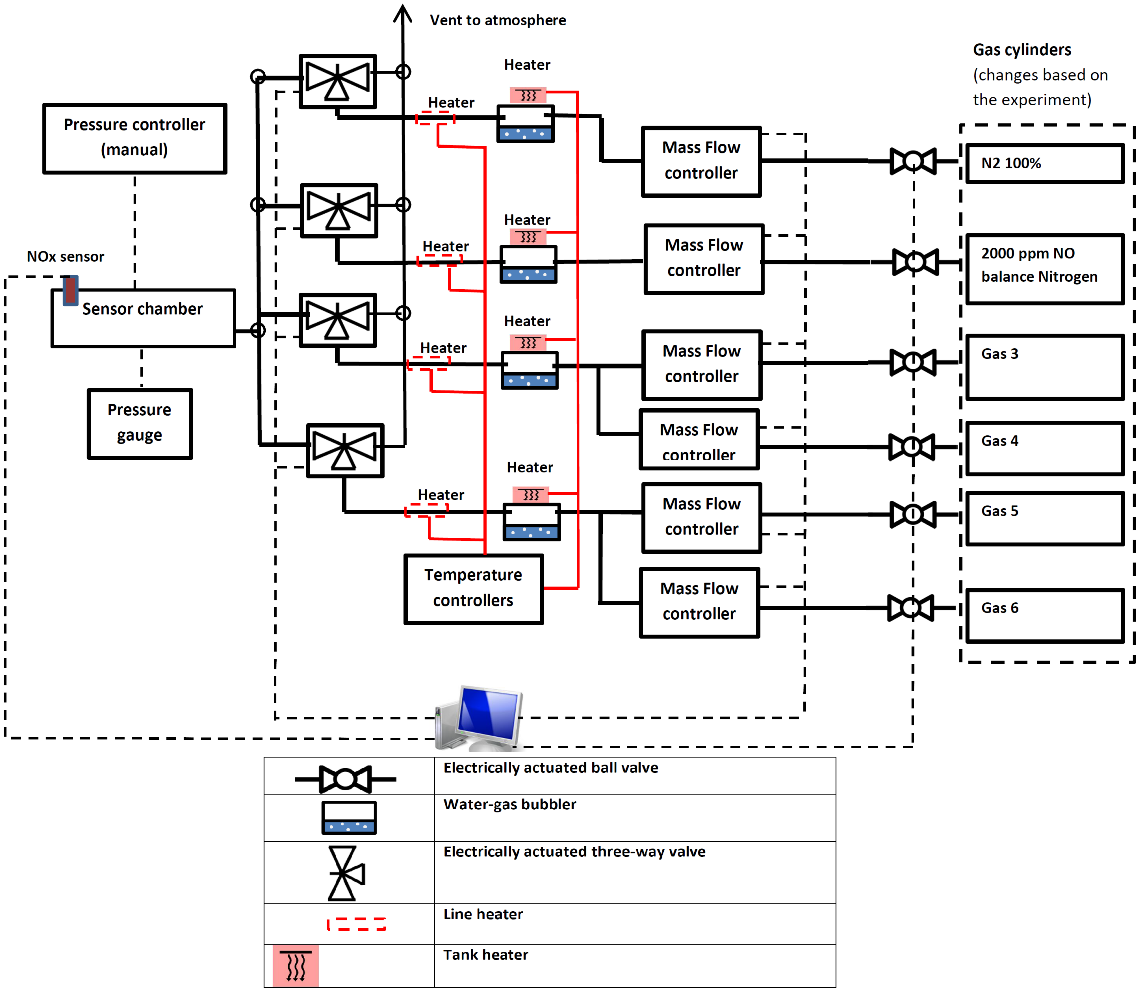

Figure 3.12: Sensor test rig schematic

only for measurement purposes, but for sensor protection. High temperature ceramic sensors are very sensitive to water drops and if the drops are not removed properly from the lines, they may damage the sensor(s) [135].

Thermocouples: to measure the temperature of the heated tanks and the heated lines, eight thermocouples are used and connected to the heater controllers. The thermocouples used are *OMEGA 20G K-Type*.

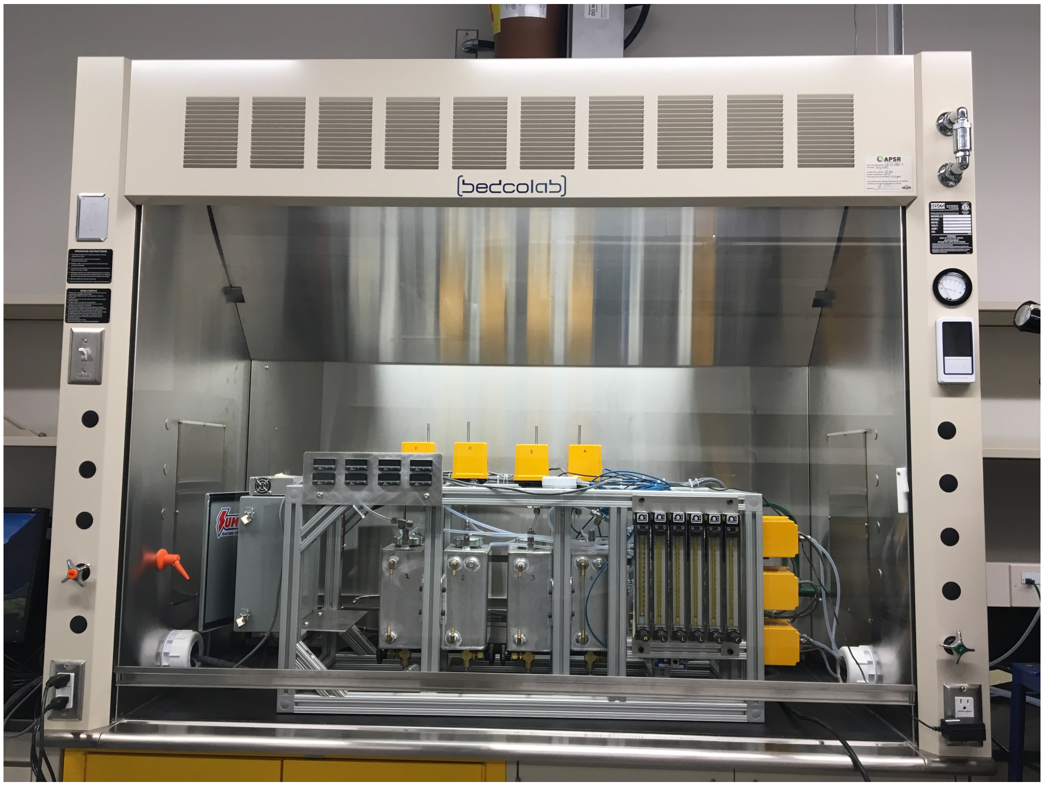

Figure 3.13: Sensor test rig setup in fume hood

Heater controllers: eight heater controllers (OMEGA CN132) used to control the heaters. The controllers measure the tank and line temperatures via the thermocouples and control the tank and line heaters through a PID controller and using analogue outputs. The control output is to OMEGA solid state relays to actuate the heaters.

Rotameter: five 2000 sccm Rotameters (OMEGA FL-3804G) and one 10000 sccm Rotameter (OMEGA FL-3839ST) are used to visually monitor the flow rate of different gasses through the sensor test rig.

Sensor chambers: to study the sensor behavior at different gas concentrations, the sensor needs to be exposed to the gas mixture inside the sensor chamber. Two

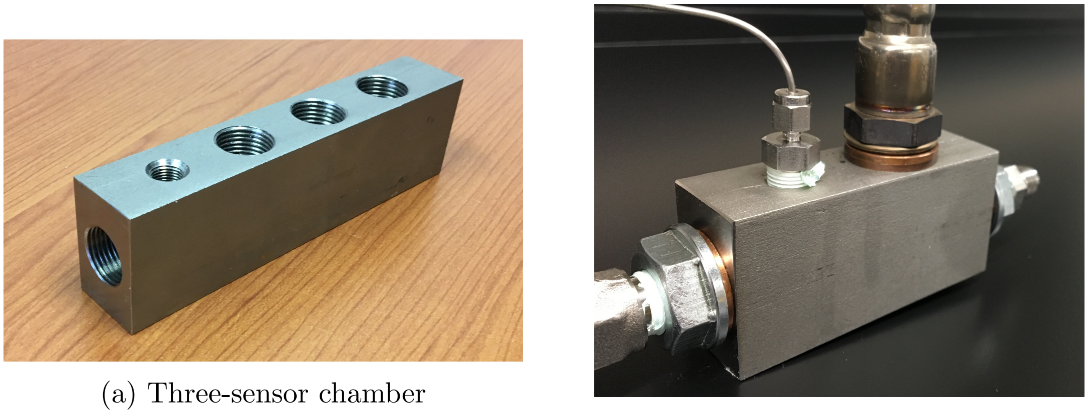

(a) Three-sensor chamber

(b) One-sensor chamber

sensor chambers with different sizes are designed and manufactured to hold one sensor and three sensors. The small volume, one-sensor chamber, and the larger volume, three-sensor chamber are shown in Figure 3.14a and Figure 3.14b respectively. The small and large sensor chamber volume are approximately 9 and 15 cm^3 respectively. To maximize the dynamics of the sensor test rig in transient conditions, the chambers are designed to minimize the chamber volume. A thermocouple hole is also mounted inside the sensor chamber to monitor the temperature of the gas inside the chamber.

Pressure transducer: to visually monitor the pressure inside the sensor chamber, a pressure gauge (OMEGA PX302-100GV) is installed downstream of the sensor chamber, the sensor chamber pressure is manually controlled by a needle valve located downstream of the chamber.

Arduino interface: A MATLAB GUI program (shown in Figure 3.15) was developed to control and monitor the sensor test rig through an Arduino interface. This interface allows control of all the valves and actuators and connects to a LAN hub to control the mass flow controllers. The Arduino interface can not create high output power to operate all the actuators. So solid state relays are used for the power electronics to actuate all the power consuming components of the test rig as shown in Figure 3.16 which are Mass Flow Controllers (MFC)s, two-way valves 1 to 6 and three-way tank valves A to D.

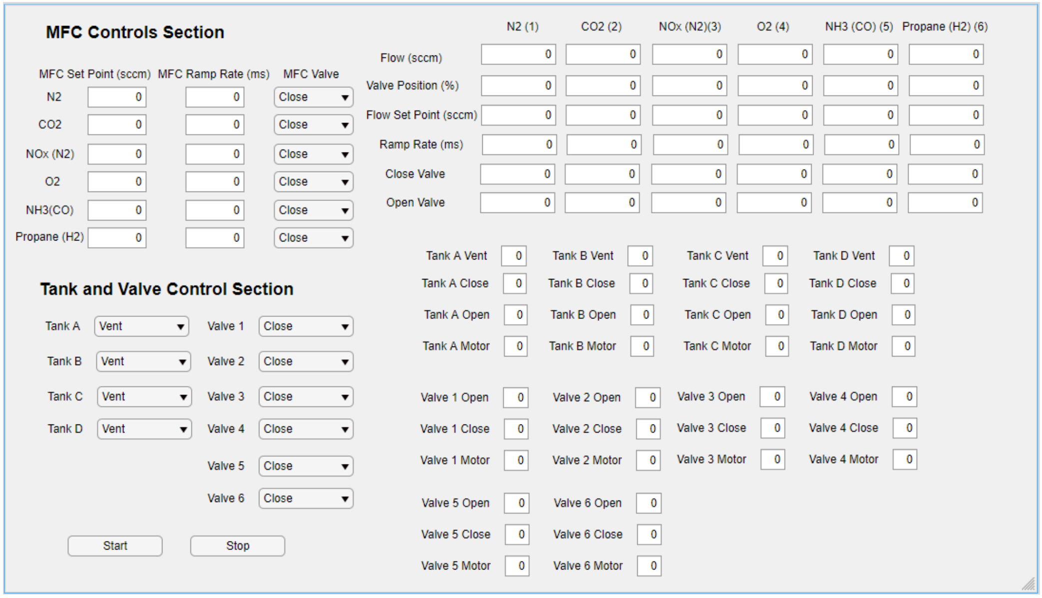

	MFC Set Point (sccm)	MFC Ramp Rate (ms)	MFC Valve
N2	0	0	Close
CO2	0	0	Close
NOx (N2)	0	0	Close
O2	0	0	Close
NH3(CO)	0	0	Close
Propane (H2)	0	0	Close

	N2 (1)	CO2 (2)	NOx (N2)(3)	O2 (4)	NH3 (CO) (5)	Propane (H2) (6)
Flow (sccm)	0	0	0	0	0	0
Valve Position (%)	0	0	0	0	0	0
Flow Set Point (sccm)	0	0	0	0	0	0
Ramp Rate (ms)	0	0	0	0	0	0
Close Valve	0	0	0	0	0	0
Open Valve	0	0	0	0	0	0

Tank A	Vent	Valve 1	Close
Tank B	Vent	Valve 2	Close
Tank C	Vent	Valve 3	Close
Tank D	Vent	Valve 4	Close
		Valve 5	Close
		Valve 6	Close

Tank A Vent	0	Tank B Vent	0	Tank C Vent	0	Tank D Vent	0
Tank A Close	0	Tank B Close	0	Tank C Close	0	Tank D Close	0
Tank A Open	0	Tank B Open	0	Tank C Open	0	Tank D Open	0
Tank A Motor	0	Tank B Motor	0	Tank C Motor	0	Tank D Motor	0
Valve 1 Open	0	Valve 2 Open	0	Valve 3 Open	0	Valve 4 Open	0
Valve 1 Close	0	Valve 2 Close	0	Valve 3 Close	0	Valve 4 Close	0
Valve 1 Motor	0	Valve 2 Motor	0	Valve 3 Motor	0	Valve 4 Motor	0
Valve 5 Open	0	Valve 6 Open	0				
Valve 5 Close	0	Valve 6 Close	0				
Valve 5 Motor	0	Valve 6 Motor	0				

Figure 3.15: MATLAB GUI programed developed to control the sensor test rig through the Arduino interface

Other parts and fittings: the sensor test rig consists of some other parts and fittings including: Check Valves (SWAGELOK SS-CHS4-1/3), Stainless Tee-Type (SWAGELOK SS-4TF-2), Union Tee (SWAGELOK SS-400-3), Male Elbows(SWAGELOK SS-400-2-4), Bulkhead Union (SWAGELOK SS-400-61) and Male Connector (SWAGELOK SS-400-1-4).

Fumehood: since most of the gasses studied in this work are either flammable (such as propane) or toxic (such as NO), the sensor test rig must operate inside a fume hood. A BEDCO VBV72 fume hood is employed to vent the sensor test rig output gases out of the lab as shown in Figure 3.13.

Gas tanks: Praxair gas cylinders with known concentrations are used to feed

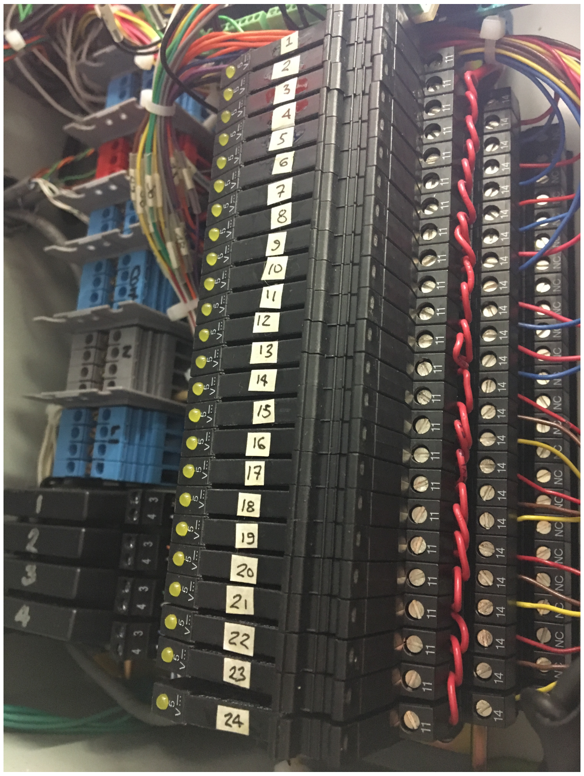

Figure 3.16: Solid state relays for test rig actuators. Pin layout is available in Appendix C.

the sensor test rig to prepare desired species concentrations for the sensor chamber. The cylinders include pure nitrogen (99.99 %), pure oxygen (99.99 %), pure CO_2 (99.99 %), 5000 [ppm] propane balanced with nitrogen, 2000 [ppm] ammonia balanced with nitrogen, 2000 [ppm] NO balanced with nitrogen, and 4000 [ppm] NO balanced with nitrogen.

3.4 Fourier-Transform Infrared Spectroscopy (FTIR)

A FTIR analyser (*MultiGas 2030*) was used to validate the NO_x sensor measurement and to measure the concentration of other species in the exhaust gas. The FTIR analyser was connected to the diesel engine exhaust pipe, upstream of the catalysts to measure the engine raw emissions. The sample exhaust gas passes through two

Heated Filters (*Flexotherm Flex MFF-7.0-S-K-A-6-L5-C-X-S-L5-M*) connected with Heated Sample Lines (*Flexotherm P/N GT-E-6/4-AT-KL-191C-B-6S-60-48*) heated to 191^{o}C to minimize water vapor condensation in the sample gas. More information about the experimental setup of the FTIR system and the heated filters is detailed in [136].

CHAPTER 4

SENSOR MODEL: PART I, DIFFUSION MECHANISM THROUGH THE BARRIERS OF AN AMPEROMETRIC NO_x SENSOR [1]

This chapter investigates the dominant diffusion mechanism of exhaust gas species through the diffusion barrier amperometric NO_x *sensor by studying the effect of sensor temperature on the sensor output. A sensor model is then developed based on this dominant diffusion mechanism to predict the sensor response at different* NO_x *and* O_2 *concentrations.*

4.1 Introduction

Production Nitrogen oxides (NO_x) sensors used in automotive industry are typically manufactured using a planar zirconia multilayer technology [93, 96, 137–139]. The latest versions of these sensors have fast light-off and response times, small size with steady high temperatures all for a low price [140]. These features make Zirconia-based amperometric NO_x sensors ideal for production Internal Combustion (IC) engines. This sensor type measures the O_2 and NO_x concentration simultaneously.

---

[1] This chapter is based on: M. Aliramezani, C.R. Koch, R.E. Hayes, and R. Patrick. *Amperometric solid electrolyte* NO_x *sensors - the effect of temperature and diffusion mechanisms.* Solid State Ionics, 313(Supplement C):7 13, 2017 [50]

Large improvements in solid electrolyte NO_x sensors development occurred in the 1990's [111, 141, 142] and was based on the idea of oxygen measurement with zirconia-based potentiometric oxygen (O_2) sensors [143–145]. Thus, the working principle and modeling methods of solid electrolyte NO_x and oxygen sensors are similar. Oxygen sensor and NO_x sensor models may cover one or all of the following: modeling gas diffusion through the barriers inside the sensor [109, 110, 124]; modeling the reactions that take place inside the sensor chambers [109, 146, 147]; and modeling the heat transfer inside the sensor and from the sensor to the surrounding environment [148, 149].

Typically a limiting-current amperometric sensors are designed with an electrode material and operated in a temperature and voltage range so that the sensor reaction dynamics are much faster than the diffusive flow of species through the sensor internal barriers [110]. Then, the sensor output is a function of the diffusion of species through the barriers into the sensor chambers. To develop reliable sensor models, a better understanding of the diffusion process is essential. The diffusion mechanism through the diffusion barriers of the NO_x sensor is not fully understood and still requires further study. The sensor temperature has an important effect on the diffusive flow inside the sensor since it affects the diffusion coefficient of gas species through the sensor diffusion barriers [110]. Therefore, a reliable and accurate estimation of the actual sensor temperature is needed to study the diffusion process.

In this chapter, different diffusion mechanisms will be evaluated and compared to experimental data. A heat transfer model is developed and used to estimate the sensor temperature. The dominant diffusion mechanism affecting the flow inside the diffusion barriers is then determined by studying the effect of temperature on diffusive flow and on the sensor outputs. Multi component molecular diffusion mechanism is shown to be capable of tracking the effect of temperature on the diffusion rate of species. This diffusion model is then used to develop the sensor model to predict the sensor outputs for O_2 and NO_x. The results are validated with experiments at different species concentrations.

4.2 Sensor structure and sensing principle

The diffusion process inside a porous medium is generally described by two main diffusion mechanisms: normal diffusion or Knudsen diffusion [150]. When the pore diameter (d_p) is smaller than the mean free path of the species, Knudsen diffusion becomes the dominant diffusion mechanism [150]. However, it is shown in [123] that in some conditions such as transition regions in a porous solid, both normal and Knudsen diffusion need to be considered. Regitz and Collings [110] and Collings et al. [124] studied the effect of pressure and temperature on the diffusion mechanism of a wide band lambda sensor considering both normal and Knudsen diffusion as parallel mechanisms. They validated the lambda sensor output current at different air-fuel values (λ values). Collings et al. [124] suggested a multi point calibration of pore diameter d_p to reduce the effect of d_p variation between sensors. Multi component molecular diffusion mechanism is used to model diffusion through diffusion barriers of oxygen sensors in [151]. Knudsen diffusion is assumed to be the dominant diffusion mechanism inside the sensor in [152]. However, it is not clear if this assumption is true for all other types of amperometric sensors and it is not clear if this assumption is valid as the sensor temperature changes. Examining the diffusion mechanism through the diffusion barrier of an automotive NO_x sensor is the focus of this work.

The sensor operates based on measuring the diffusive flow into the internal sensor chambers [140, 153]. A production ECM NO_x sensor (P/N: 06-05) has been X-ray imaged with spatial resolution of $5176 \times 1450 \times 1051$ pixels ($0.007, 0.007$ and 0.005 mm/pixel)[2]. The exact dimensions of the internal parts of the NO_x sensor are used

---

[2] We would like to express our gratitude to Dr. André Phillion for taking the X-ray tomography images.

to parameterize the sensor model.

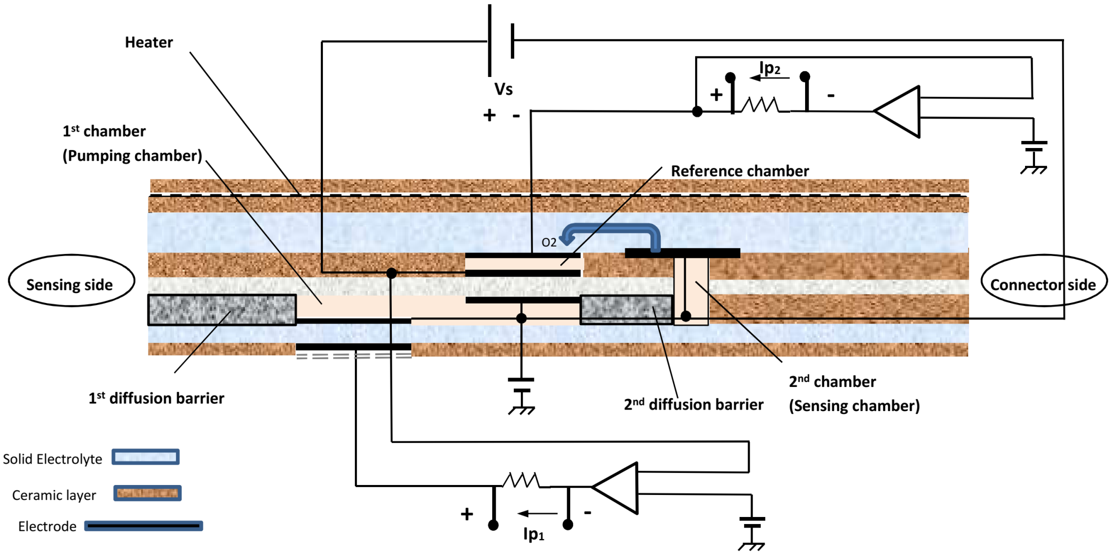

Figure 4.1: Longitudinal cross sectional schematic view of the NO_x sensor

The first chamber, second chamber and reference chamber are the three main chambers in an amperometric NO_x sensor and are schematically shown in Figure 4.1. A zirconia based oxygen pump, pumps O_2 out from the first chamber. The pumping current is proportional to oxygen concentration in the surrounding gas. At the same time, all NO_2 molecules are reduced and converted into NO in the first chamber. The species then diffuse into the second chamber through the second diffusion barrier. In the second chamber, NO is reduced and oxygen ions are pumped out using a Nernst cell into the reference chamber. The pumping current of the second chamber is proportional to NO and thus NO_x concentration.

The sensor consists of three Nernst cells. The O_2 sensing cell, the NO_x sensing cell and the reference cell. A closed loop controller keeps the potential of the reference cell constant by pumping out O_2 from the O_2 sensing chamber. The pumping current is proportional to the diffusion rate of oxygen since each oxygen molecule transfers 4 electrons into the cavity. Thus:

$$I_{p1} = 4F \times N_{O_2,fc} \tag{4.1}$$

where, $N_{O_2,fc}[\frac{mol}{s}]$ is the molar flow of oxygen through the first diffusion barrier and I_{p1} is the pumping current of O_2 from the O_2 sensing cell as shown in Figure 4.1.

4.3 Diffusion model description

To predict the sensor output signals, the diffusive flow through the porous diffusion barriers must be modeled. To define the dominant diffusion mechanism, the diffusion coefficients are first calculated using a normal multi-component mechanism. A mixture-averaged method is then used to calculate the diffusion coefficient of each species from the multi-component mechanism. The diffusion coefficients are also defined using Knudsen diffusion mechanism. The diffusion model is also developed considering both diffusion mechanisms at the same time as in [110] and [124]. All of the physical dimensions used to parameterize the model are measured using X-ray tomography of the sensor.

4.3.1 Molecular diffusion mechanism

A mixture-averaged diffusion model is used to define the species mass flux through the diffusion barriers. This model, which can be used for multi component diffusion simulations, is not very computationally expensive and is accurate for diffusion dominated flow modeling [154, 155]. The sensor temperature is varied using the sensor heater and sensor control module. The absolute pressure of the sensor barriers and cavities is assumed to be a function of engine speed and engine output torque[3].

Mixture-Averaged diffusion model

---

[3] A differential pressure sensor measures the pressure difference through the Diesel Oxidation Catalyst (DOC). The absolute pressure around the sensor is calculated by adding this differential pressure to the barometric pressure.

The relative mass flux vector using mixture-averaged diffusion model is calculated using [150]:

$$j_i = -\Big(\rho D_i^{(m)} \nabla \omega_i + \rho \omega_i D^{(m)} \frac{\nabla M}{M}\Big) \tag{4.2}$$

Where, j_i is mass flux vector of species i and ρ, M and ω_i are mean density, mean molar mass and mass fraction of species i respectively . Index (m) is for **m**ixture average. The mixture-averaged diffusion coefficient ($D_i^{(m)}$) is:

$$D_i^{(m)} = \frac{1-\omega_i}{\sum_{q \neq i}^{N} \frac{x_q}{D_{iq}}} \tag{4.3}$$

$$D_{iq} = \frac{10^{-3} T^{1.75} (\frac{1}{M_i} + \frac{1}{M_q})^{1/2}}{P[(\Sigma\nu)_i^{1/3} + (\Sigma\nu)_q^{1/3}]^2} \tag{4.4}$$

in which, D_{iq} is defined from the Fuller correlation [150]. In Eqns (4.3) and (4.4), x_q is mole fraction of species q and N is the number of species. To model the $\mathrm{NO_x}$ sensor, the boundary conditions and some assumptions are needed which are discussed next. In Eqn (4.4), P is absolute pressure in atm, T is in K and $(\Sigma\nu)_i$ is the diffusion volume of species i, defined in [150]. The Millington and Quirk model [156] is used to calculate the effective diffusion coefficient of the porous solid from the normal diffusion coefficient:

$$D_{i,por} = \epsilon^{4/3} D_i \tag{4.5}$$

where ϵ is porosity and defined as: $\epsilon = \frac{V_v}{V_{total}}$, V_v and V_{total} are the void volume and the total volume of the porous media respectively.

4.3.2 Knudsen diffusion mechanism

The other diffusion mechanism that is examined in this work is Knudsen diffusion. Generally, Knudsen diffusion becomes the dominant diffusion mechanism when the pore diameter ($\mathrm{d_p}$) is smaller than the mean free path of the species [150]. In some conditions such as transition regions in a porous solid, the Knudsen mechanism also needs to be considered [123]. This mechanism considers species collisions with the pore walls. The Knudsen diffusion coefficient (D_i^k) is calculated based on kinetic gas theory [150] as:

$$D_i^k = \frac{L_m}{3}\sqrt{\frac{8\bar{R}T}{\pi M_i}} \tag{4.6}$$

where, L_m is the mean path length which is typically close to the pore diameter for gas transport in porous media since a certain species is more likely to collide with pore wall than another molecule [150]. The term M_i is the specie molar mass. Replacing L_m with the pore diameter ($2 \times r_p$) in Eqn. (4.6) and substituting for the constants results in [157]:

$$D_i^k = 97 r_p \sqrt{\frac{T}{M_i}} \tag{4.7}$$

where, D_i^k, r_p, T and M are in m^2/s, m, K and $kg/kmol$ respectively.

4.3.3 Normal and Knudsen diffusion mechanism

To combine the effect of both diffusion mechanisms, an effective diffusion factor is calculated. The Knudsen diffusion coefficient corrects the mixture-averaged diffusion coefficient (D_i^m) as [150]:

$$D_i^{mk} = (\frac{1}{D_i^m} + \frac{1}{D_i^k})^{-1} \tag{4.8}$$

which substituted into Eqn (4.2) results in:

$$j_i = -(\rho D_i^{mk} \nabla \omega_i + \rho \omega_i D^{mk} \frac{\nabla M}{M}) \tag{4.9}$$

4.3.4 First diffusion barrier and first chamber

Now, the diffusion from the sample gas - here engine exhaust, through into the first and the second chamber will be examined. The diffusion barriers are shown in the sensor schematic (Figure 4.1) and for additional clearity are also shown in a simplified model schematic in Figure 4.2. The fuel is taken to be an idealized typical Diesel fuel with chemical formula of $C_{12}H_{23}$ and complete combustion is assumed. These assumptions are used to calculate the stoichiometric air-fuel ratio (λ) from O_2 concentration in the exhaust gas.

The exhaust gas is assumed to be a mixture of only O_2, N_2, CO_2, H_2O and NO_x which diffuses through the first diffusion barrier. The diffusion model consists of multi component gas diffusion through the diffusion barriers. It also assumes that oxygen is pumped out of the first chamber at a much faster rate than the diffusion rate of oxygen into the chamber. This means that the oxygen concentration can be assumed to be zero at the end of first diffusion barrier (first chamber). It is important to note that all the chamber models are assumed to not vary in spatial dimensions - a lumped parameter model. One of the most important reactions that take place inside the first chamber is conversion of all NO_2 molecules to NO [158].

4.3.5 Second diffusion barrier and the second chamber

Gas then diffuses from the first to the second chamber. The gas entering the second diffusion barrier is assumed to be NO, N_2, CO_2 and H_2O. The O_2 has been removed by the first chamber and all NO_x converted to NO. The same multi component diffusion model is used to simulate diffusion through the second diffusion barrier. The sensing principle of the second chamber is similar to the first chamber. However, in the second chamber, compared to the first chamber, NO affects the sensor output. In the second chamber NO is reduced causing a concentration gradient so NO diffuses from the first chamber. The NO reduction in the second chamber converts NO to nitrogen and oxygen and again this reaction is assumed to be much faster than the diffusion rate. In other words, NO concentration is assumed to be zero at the end of the second diffusion barrier. Each NO molecule transfers one atom of oxygen (two electrons). Therefore, Eqn (4.1) which is used for the first chamber is now:

$$I_{p2} = 2F \times N_{NO,sc} \tag{4.10}$$

where, $N_{NO,sc}[\frac{mol}{s}]$ is the diffusive molar flow of NO through the second diffusion barrier into the second chamber.

A schematic of the whole diffusion model is shown in Figure 4.2.

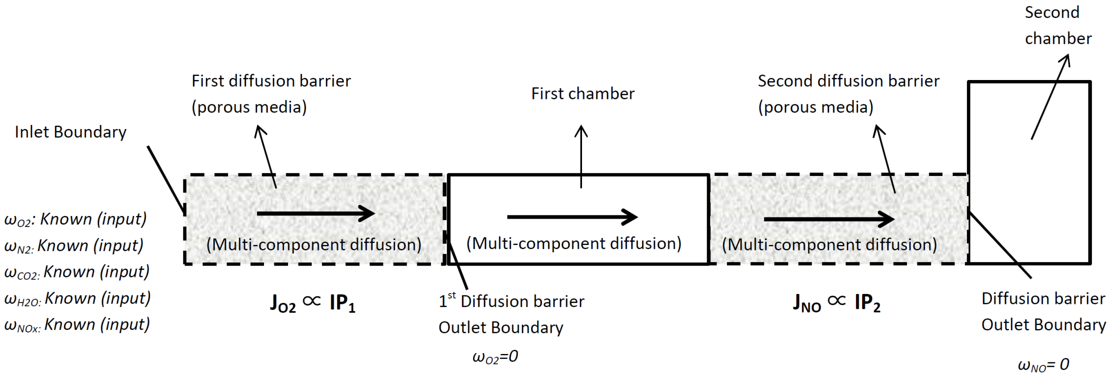

Figure 4.2: NO_x sensor diffusion model schematic for the two chambers

4.4 Heat transfer model

The sensor response is highly dependant on temperature since the diffusion through the diffusion barriers, Eqn. (4.4) and (4.7), and the chamber reactions [108] are strongly dependant on temperature. The sensor temperature was controlled by a heater embedded inside the sensor. It is assumed that the temperature of the sensor chambers and the heater temperature are the same. The impedance, R_{pvs}, of Vs cell (shown in Figure 4.1) varies with temperature and was used to measure the sensor temperature. R_{pvs} was experimentally measured by the sensor control module at all operating conditions. To define the sensor temperature at different R_{pvs} values, a heat transfer model is needed. This model should include the heat transfer from the sensor heater located inside the sensor ceramic to the sensor hoursing and from there to the exhaust pipes (see Figure 4.3). A schematic of the heat transfer model is shown in Figure 4.4 considering convection and radiation heat transfer:

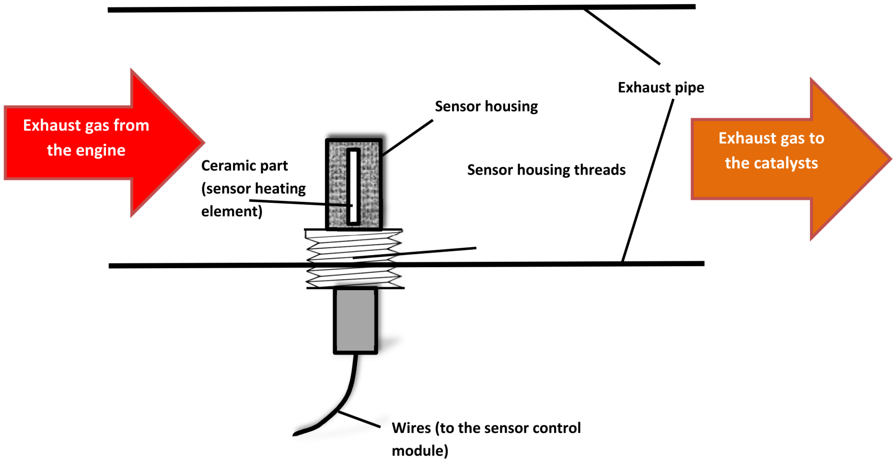

Figure 4.3: Heat transfer model elements

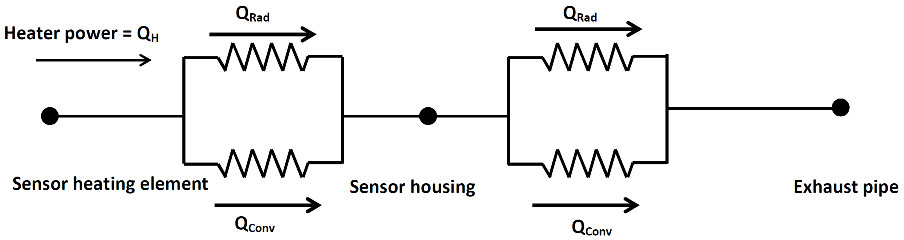

Figure 4.4: NO_x sensor heat transfer schematic

Heat is first transferred from the sensor heating element to the sensor housing and then from the sensor housing to the exhaust pipe both via convection and radiation. The *engine off* condition was used to define sensor temperature at different R_{pvs} values since the exhaust gas and exhaust pipe temperature are known to be approximately room temperature. Then, the results were used for the other engine operating conditions. At *engine off* there is no forced convection heat transfer around the sensor as there is no exhaust gas flow. In addition, the sensor temperature (around 1000 K) is much higher than the environment temperature. So, at *engine off*, the convection heat transfer was assumed to be negligible compared to the radiated heat transfer. The heat transfer from the sensor element to the sensor housing is: $Q_H = \sigma(\epsilon_e T_e^4 - \epsilon_h T_h^4)$ and heat transfer from the sensor housing to the exhaust pipe is: $Q_H = \sigma(\epsilon_h T_h^4 - \epsilon_p T_p^4)$. Where, ϵ_e, ϵ_h and ϵ_p are emissivity coefficients of the sensor element, the sensor housing and the exhaust pipe respectively, σ is the Stefan-Boltzmann Constant, T_e, T_h and T_p are element temperature, sensor housing temperature and exhaust pipe temperature respectively. Combining the two heat transfer equations and solving for T_h results in:

$$T_h = \sqrt[4]{\frac{T_e^4 \epsilon_e + T_p^4 \epsilon_p}{2\epsilon_h}} \tag{4.11}$$

and now assuming that $T_p^4 << T_e^4$, from Eqn (4.11), results in:

$$Q_H \propto T_e^4 \tag{4.12}$$

where Q_H is the heater power.

4.5 Experimental testing

4.5.1 Heat transfer model validation

The engine was a 4 cylinder medium duty diesel engine (Cummins QSB4.5 160 - described in section 3.2.1). The sensor temperature was controlled by the NO_x sensor control module. This module controls the element temperature by controlling heater power. The impedance, R_{pvs}, of Vs cell (shown in Figure 4.1) varies with temperature and was used as the feedback of sensor temperature closed loop control. Therefore, to control the element temperature, the controller measured R_{pvs} and maintained it constant by changing heater power.

The relation between sensor temperature and R_{pvs} were defined at *engine off* condition for which the assumptions leading to Eqn (4.12) are as close as possible. The tests were performed at different R_{pvs} set points and different heater power values. To define the sensor temperature based on the heater power, the sensor temperature was first changed by changing the R_{pvs} set point. A closed loop controller inside the sensor control module changed the heater power to track the R_{pvs} set points. After measuring the sensor heater power at each R_{pvs} set point and at the *engine off* operating condition, the factory default temperature value of T_s=1023 K at R_{pvs} = 252 Ohms and Eqn (4.12) were used. For the other engine operating conditions, the calibrated R_{pvs} *vs* T_s table was used to estimate the sensor temperature without using the heat transfer model. A flow chart of the modeling process is shown in Figure 4.5. The complete experimental heat transfer results are listed in Appendix B, Table B.1 to B.4.

The tests were carried out at three engine operating conditions and the *engine off* condition. To evaluate the accuracy of the heat transfer model and the estimated temperatures, the linearity of heater resistance vs temperature was evaluated. The heater power and heater voltage were measured at different sensor temperatures and the heater resistance was calculated by Ohm's law ($R_H = P_H/V_H^2$). As expected for a metallic material, the relation between the heater resistance and temperature is almost linear, with a correlation coefficient R^2 of 0.9837. This confirms that the heat transfer model is valid and accurate when the engine has no forced convection from the exhaust flow.

The relation between heater power and sensor temperature at different operating conditions is shown in Figure 4.6 with average exhaust temperature noted in the figure. The required value of heater power for a certain temperature at *engine off* condition and at 2500 rpm and 30 lb-ft are almost the same. At 2500 rpm and 30 lb-ft, although the engine is running, the cooling effect of the forced convection to the exhaust gas is offset to a higher exhaust gas temperature compared to the *engine off* condition. Only slightly more heater power than at *engine off* operating condition is needed at high sensor temperatures. However, as the engine load increases, lower heater power is required to maintain the sensor at a certain temperature since the exhaust gas temperature increases with engine load offsetting the convective loss.

4.5.2 Diffusion model validation

To define the dominant diffusion mechanism inside the sensor, diffusion coefficients were defined from multi component molecular diffusion mechanism, Knudsen diffusion and both diffusion mechanisms at the same time. The results are shown in Figure 4.7 for *engine off* operating conditions. Multi component molecular diffusion mechanism closely matches the experiments, and so is the dominant diffusion mechanism that effects the diffusive flow inside the diffusion barrier of the sensor. The deviation between the diffusion models is due to different dependencies on temperature. Knudsen diffusion coefficients are proportional to the square root of temperature, Eqn (4.7), while the diffusion coefficients of normal diffusion are proportional to $T^{1.75}$, Eqn (4.4). In addition, the density of all species decreases as temperature increases according to ideal gas law and this affects the mass flux of species, see Eqn (4.2). For the Knudsen diffusion coefficient, the decreasing effect of temperature on density overcomes its increasing effect on the molar flux of O_2 into the first chamber and consequently reduces I_{p1}. This behavior is not compatible with the experiments. However, multi component molecular diffusion mechanism matches the experiments and is capable of tracking the effect of temperature on diffusive flux of O_2 into the first chamber, indicating Knudsen diffusion is not important for these sensors.

To look at a combination of normal and Knudsen diffusion, the production sensor temperature of 1023 K and *engine off* conditions were chosen to calibrate the model. Porosity was calibrated for normal diffusion model and the value of mean path length was calibrated at this operating condition for Knudsen diffusion. Considering both normal and Knudsen diffusion, the combined model has a diffusive flux between normal and Knudsen diffusive fluxes. This combined model does not match experiments as the temperature is varied as shown in Figure 4.7. Although all diffusion mechanisms were calibrated to the same diffusion coefficient at 1023 K, a 63 K increase in sensor temperature at *engine off* operating condition resulted in an error of Knudsen diffusion of 6.1 % and the combined mechanism of 3.3 %. For Knudsen mechanism, this error was 7.5%, 5.2% and 7.6 % for three loads of 2500rpm - 30lb.ft, 2000rpm - 100lb.ft and 1500 rpm - 200 lb.ft respectively. The error increases as the sensor temperature differs from the calibration temperature (1023 K). Normal diffusion which most closely matches with the experiment, is the only diffusion mechanism that is considered in the remainder of this thesis.

4.5.3 Sensor model validation

Now, using normal diffusion as the dominant diffusion mechanism, the model was evaluated at different engine operating conditions with different concentrations of species in the exhaust gas as shown in Figure 4.8. The normal diffusion model accurately predicts pumping current for a range of temperaturs and for all the operating conditions tested.

The actual NO_x concentration was obtained from the calibrated lookup table provided with the sensor. This calibration table is obtained from calibrating the sensor using known gases and a calibration rig. The calibrated lookup table for NO_x concentration is only valid at standard factory sensor temperature (1023 K) which was also used in the model having normal diffusion. The NO_x sensor model validation based on Eqn (4.10) is shown in Figure 4.9. The maximum error of I_{p2} model was 4.85% at NO_x = 650 [ppm] indicating that the simple model developed does an acceptable job in predicting NO_x.

4.6 Conclusions

Normal diffusion was found to be the dominant diffusion mechanism of a production amperometric NO_x sensor. The sensor temperature was changed using a sensor control module to evaluate the effect of temperature on the sensor outputs which was proportional to the diffusive flux of species through the barriers. The sensor dimensions were obtained from x-ray images of the internal parts (chambers and barriers) and were used in the model.

Knudsen diffusion, multi component molecular diffusion mechanism and mixture averaged method (Normal and Knudsen diffusion) were evaluated by varying the sensor temperatures and comparing the model output to the experiments. A sensor model is developed based on the molecular diffusion mechanism to calculate the sensor outputs for O_2 and NO_x concentrations corresponding to engine off and three engine operating conditions. The sensor model output closely matches the experiments at different engine operating conditions and different concentration of species in the exhaust gas with maximum error of 0.79% for oxygen measurement output (IP_1) and maximum error of 4.85% for NO_x measurement output (IP_2). The developed sensor model can be used to reduce the effect of manufacturing deviations on the sensor output signals and the measurement error without re-calibrating the sensor. The diffusion model is an essential element the sensor model and will be used in subsequent chapters of this thesis to develop more complex sensor models incorporating electrode reactions and electrochemical models.

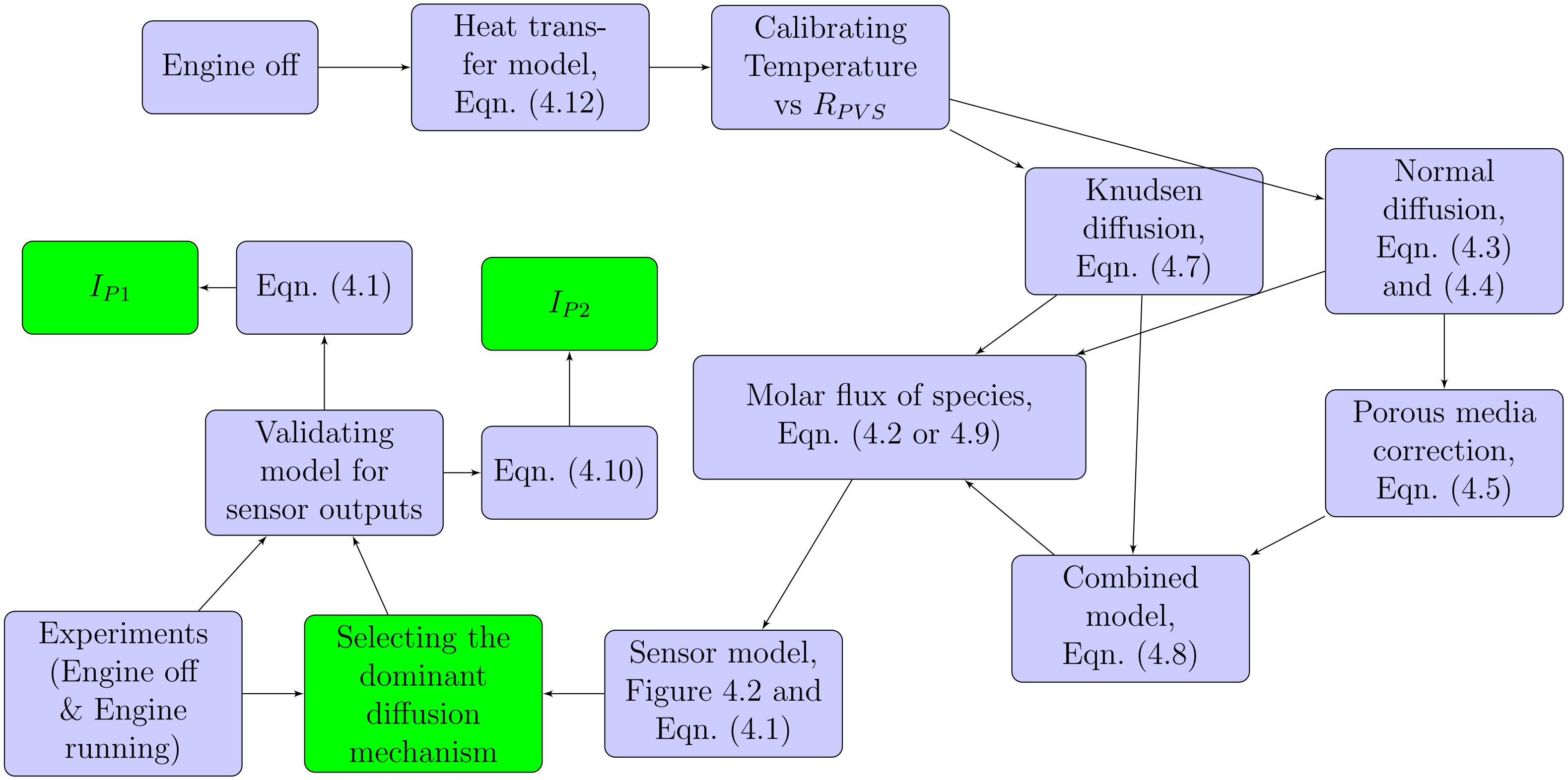

Figure 4.5: NO_x sensor diffusion and heat transfer models overview

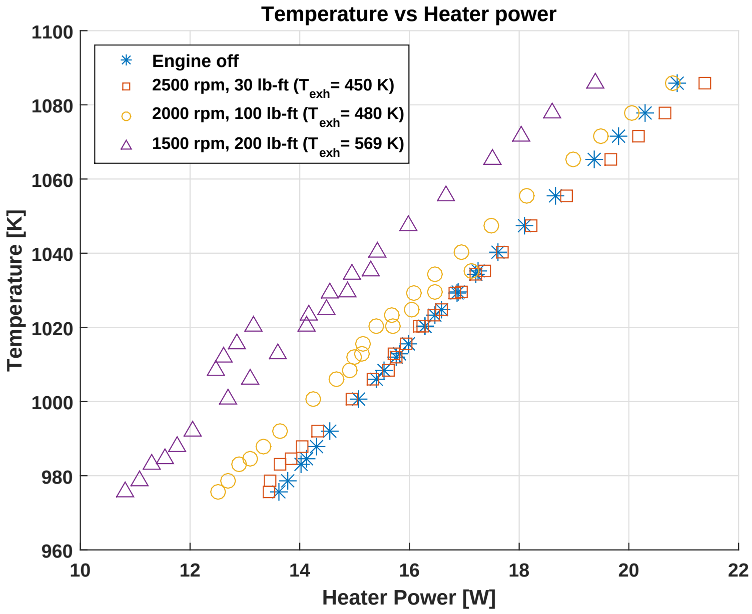

Figure 4.6: Temperature vs heater power

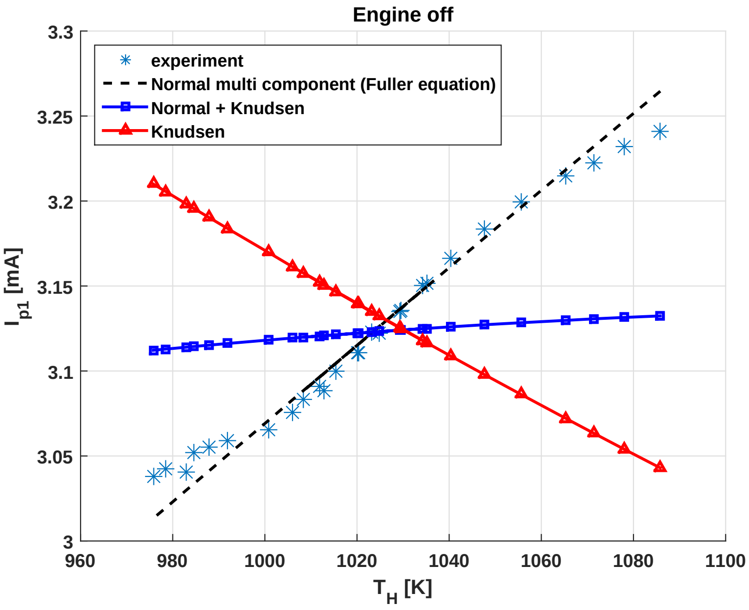

Figure 4.7: Oxygen pumping current (IP1) vs sensor temperature at *Engine off* for different diffusion mechanisms

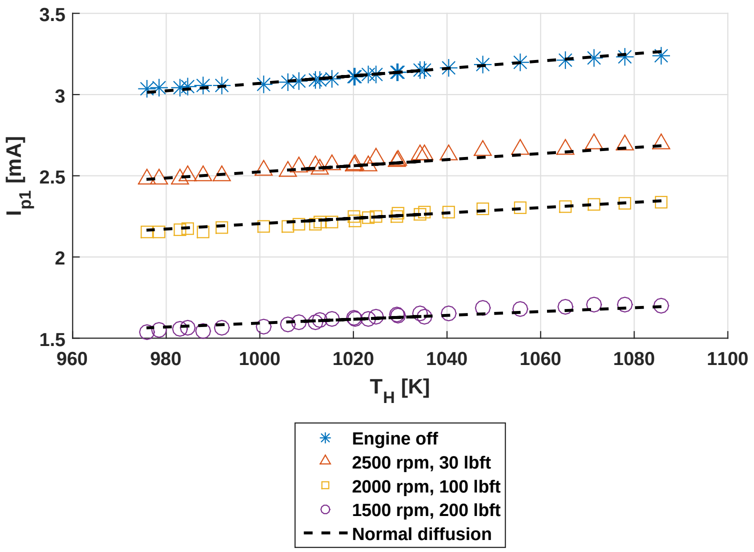

Figure 4.8: Oxygen pumping current (IP1) vs sensor temperature for normal multi-component diffusion mechanism

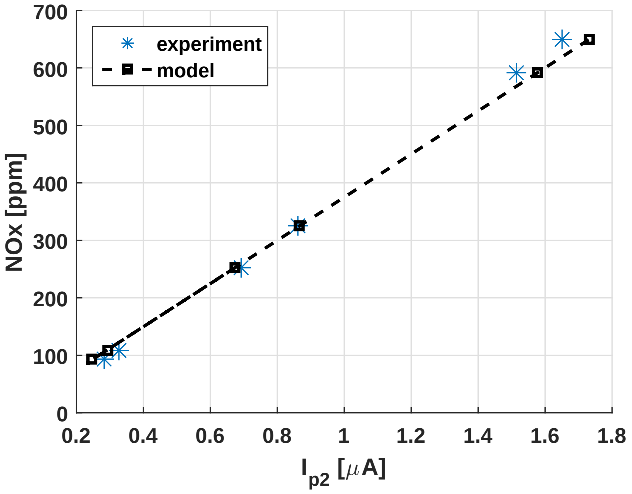

Figure 4.9: NO_x sensor model vs experimental values

Chapter 5

Sensor model: Part II, comprehensive sensor model that includes electrochemical and diffusion submodels [1]

This chapter provides details of a comprehensive sensor model developed in this research that includes electrochemical and diffusion submodels.

5.1 Introduction

Although an amperometric sensor is typically operated at a temperature and cell voltage range so that the diffusion of species into the measurement cell is the dominant process that affects the sensor output [54], a more comprehensive understanding of the electrochemical cell is beneficial for optimizing the sensor performance, durability and sensitivity [159, 160]. The effect of electrochemical properties of electrodes on the sensing behavior of solid state electrochemical gas sensors has been studied in detail [111–114]. The sensitivity of amperometric sensors to gas species and the reliability of these sensors are directly affected by electrochemical properties [115]. These properties include electrode material [116–118], electrode potential [119], electrolyte

---

[1] This chapter is based on: M. Aliramezani, C.R. Koch, M. Secanell, and R. Patrick. *An electrochemical model of an amperometric NOx sensor*. Sensors and Actuators B, 290, pp. 302-311, 2019 [51].

properties [120–122] and properties of diffusion barrier [50, 54, 123, 124].

These previous studies are mostly experimental and do not include quantitative physics-based models of the main relevant processes that simultaneously take place inside the sensor and affect the sensor output. An understanding of solid-state amperometric sensors that includes both the electrochemical properties and species diffusion is essential to provide further insight into the performance of these sensors and is the subject of this chapter. To do this, a physics-based model of an amperometric NO_x sensor is developed that includes diffusion of multiple sample gas species into the sensor chambers through the sensor diffusion barriers. The model also includes an electrochemical submodel that calculates the sensor pumping current as a function of sensing cell voltage. To experimentally validate the model at different NO_x concentrations and NO_x sensing cell voltages, the sensor is first mounted in the exhaust system of a medium duty Diesel engine, then in a port injection spark ignition (SI) engine exhaust system and finally in a controlled gas mixture test bench. The diffusion model is used to calculate the mole fraction of O_2 and NO_x in the sensor chambers. The mole fractions are then used in the NO_x sensing cell electrochemical model to define the sensor pumping current from the cell voltage. The diffusion and the electrochemical model are coupled and solved simultaneously. The ohmic loss, the activation loss and the concentration loss have been included in the model. The NO_x sensor output is then calculated as a function of the sensing cell potential and NO_x concentration.

5.2 Amperometric NO_x sensor

The working principle of an amperometric NO_x sensor has been detailed in chapter 4. The same production amperometric NO_x sensor (ECM, P/N: 06-05 [128]) is studied in this chapter. The sensor consists of two sensing chambers as shown schematically in Figure 5.1. The first chamber is the O_2 sensing chamber while the second chamber is the NO_x sensing chamber. The first chamber has a Platinum (Pt)-based electrode (typically, Platinum-Gold (Pt-Au) alloy) while the second chamber has a Pt electrode [108]. In the first chamber, O_2 is reduced and the resulting O^{2-} ions are pumped out with a pumping current proportional to oxygen concentration in the sampling gas. The Pt-Au electrode has a higher activation energy for NO reduction than the Pt electrode and this enables selective O_2 and NO_2 reduction inside the first chamber at the typical sensor operating condition [108]. Therefore, NO_2 is reduced to NO inside the first chamber. The remaining species diffuse into the second chamber through the second diffusion barrier. In the second chamber, NO is completely reduced and the resulting O^{2-} ions are pumped out through an electrochemical cell into the reference chamber as shown in Figure 5.2. Therefore, the pumping current of the second chamber cell is proportional to the total NO_x (NO_2 and NO) concentration.

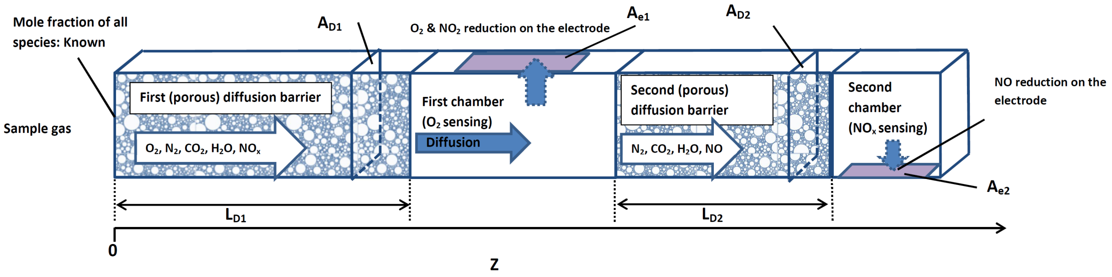

Figure 5.1: NO_x sensor working principle and diffusion model structure

The working principle of the NO_x sensing cell is schematically shown in Figure 5.2.

5.2.1 Sensor dimensions using X-ray tomography

The exact dimensions of the internal components of the NO_x sensor are measured to parameterize the sensor model, using X-ray tomography. The sensor top view using the x-ray tomography image is shown in Figure 5.3 detailing the sensor components.

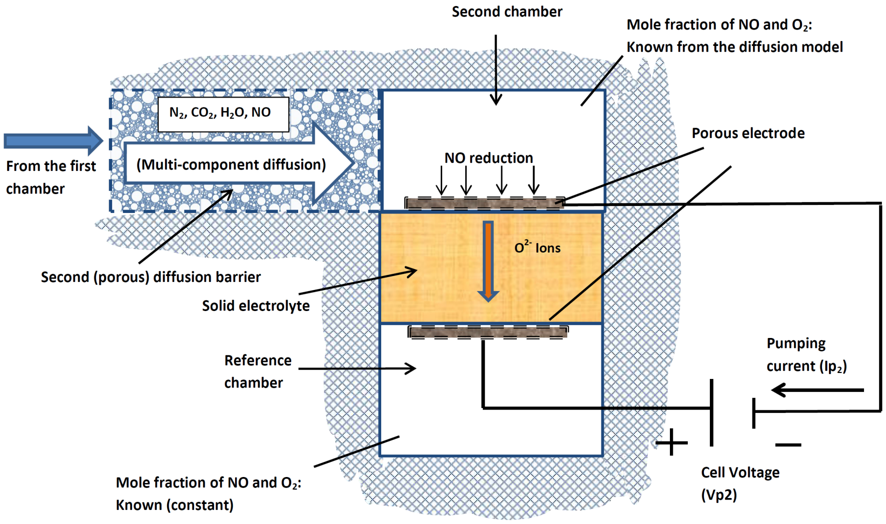

Figure 5.2: Boundary conditions of the NO_x sensing cell (second chamber)

5.3 Sensor model

Typical current-voltage response of an amperometric sensor as the cell voltage (V_P) is varied is shown in Figure 5.4 [50, 125, 126]. The response is divided into six regions that depend on the sensing cell voltage. In region I, the cell voltage is lower than the open-circuit potential and not high enough to cause reduction of species on the cathode. Therefore, the reverse reaction (oxidation) takes place causing a negative cell current. When the cell voltage is just above the open-circuit potential, activation polarization becomes the rate-determining step. This phase is labeled as region II. In region III, the cell current varies almost linearly with voltage, based on Ohm's law. In this region, the Ohmic loss dominates the cell voltage-current relation. As the cell voltage increases further, the current-voltage relation becomes non-linear in region IV and then the cell current finally reaches a saturation level determined by the diffusion rate of oxygen into the chamber (region V). In region V the pumping rate of (O^{2-}) ions from the cell has reached its maximum level since all available reducible molecules are being reduced on the cathode as soon as they reach the electrode surface. The

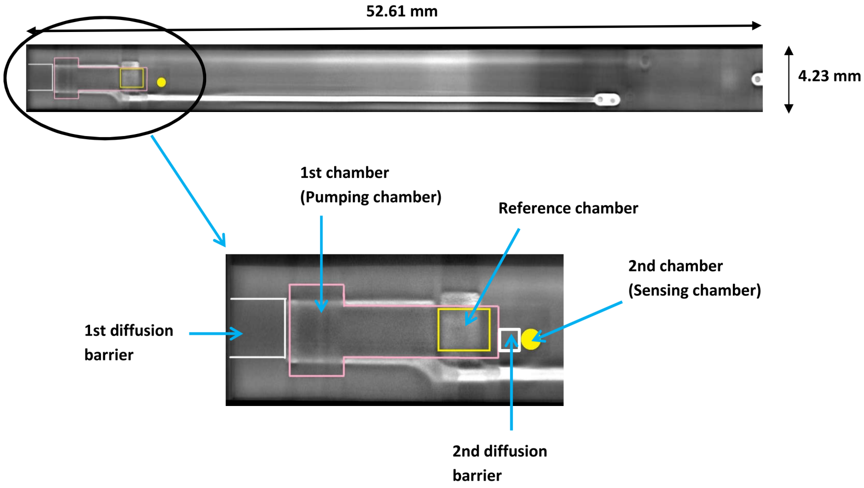

Figure 5.3: X-ray tomography of the NO_x sensor ceramic (top view)

transition phase from ohmic behavior to the limiting current region is marked as region IV.

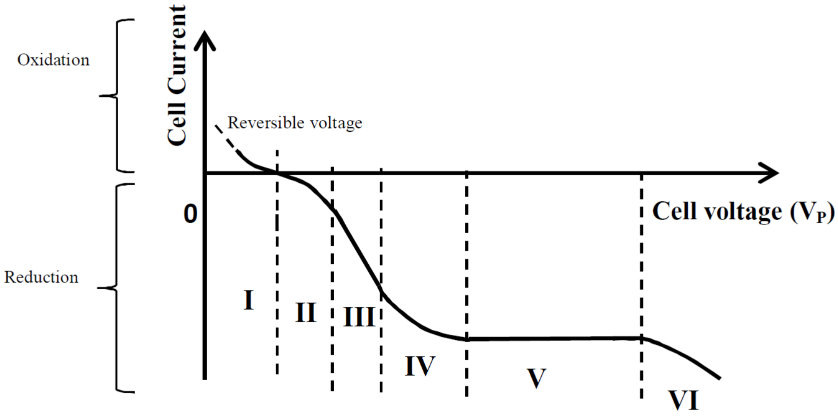

Figure 5.4: Typical electrode current vs potential relation

Further increases in the cell voltage, results in the partial pressure of the reduced species (in this case, NO) becoming lower according to the Nernst equation [95]. If the partial pressure of the reduced species (NO) decreases to less than a certain value ($\approx 10^{-33}$ atm), electrolyte decomposition takes place [127]. This causes a further increase in the O^{2-} pumping rate and therefore the cell current increases (region VI) which can potentially damage the sensor. The sensor behavior in this region is not studied in this work as it is not useful when measuring NO_x.

5.3.1 NO_x sensing cell electrochemical model

The components of an overall NO_x sensor model will be described.

5.3.1.1 NO_x sensing cell electrochemical model

A simple model of the reactions that take place in the NO_x sensing cell is:

$$Cathode : NO + 2e^- \rightarrow \frac{1}{2}N_2 + O^{2-} \tag{5.1a}$$

$$Anode : O^{2-} \rightarrow \frac{1}{2}O_2 + 2e^- \tag{5.1b}$$

$$Overall : NO \rightarrow \frac{1}{2}O_2 + \frac{1}{2}N_2 \tag{5.1c}$$

The Nernst voltage is then [95]:

$$E_N = E^o_{sc} + \frac{\Delta S_{ox-red,sc}}{2F}(T - T_o) - \frac{\bar{R}T}{2F} ln\left(\frac{p^{0.5}_{O_2,rc} p^{0.5}_{N_2,rc}}{p_{NO,sc}}\right) \tag{5.2}$$

where, $p_{NO,sc}$, $p_{O_2,rc}$ and $p_{N_2,rc}$ are the partial pressure of NO in the second chamber, and the partial pressures of oxygen and nitrogen in the reference chamber, respectively. $\bar{R}$ is the universal gas constant, F is the Faraday constant, T is the sensor temperature (all temperatures are in Kelvin), T_o is the reference temperature, E^o_{sc} is the open-circuit potential at the standard condition (1 atm; 298.15 K) and ΔS_{ox-red} is the change in entropy of $products - reactants$ at the operating temperature (the index sc stands for the second chamber, while rc stands for the reference chamber). In this case, it is approximated as [95]:

$$\Delta S_{ox-red} \approx \Delta S^o_{ox-red} = \sum_{Prod} \nu_i \Delta S^o_i - \sum_{Reac} \nu_j \Delta S^o_j \tag{5.3}$$

where, ν_i and ν_j are the stoichiometric coefficient of species i and j respectively.

When kinetic, ohmic and transport losses are included, the second chamber cell voltage (V_{P2}) becomes [95, 161]:

$$V_{P2} = \underbrace{E^o_{sc} + \frac{\Delta S_{ox-red,sc}}{2F}(T - T_o) - \frac{\bar{R}T}{2F} ln(\frac{p^{0.5}_{O_2,rc} p^{0.5}_{N_2,rc}}{p_{NO,sc}})}_{E_N} - \eta_\Omega - \eta_{ac} \tag{5.4}$$

where, η_Ω and η_{ac}, are Ohmic and kinetic-transport polarization losses respectively [95, 161]. According to Dalton's law of partial pressures [162], the total mixture pressure is equal to the sum of partial pressures of all species in the mixture. Therefore, dividing by the total pressure of the mixture, Eqn. (5.4) becomes:

$$V_{P2} = \underbrace{E^o_{sc} + \frac{\Delta S_{ox-red,sc}}{2F}(T - T_o) - \frac{\bar{R}T}{2F} ln(\frac{x^{0.5}_{O_2,rc} x^{0.5}_{N_2,rc}}{x_{NO,sc}})}_{E_N} - \eta_\Omega - \eta_{ac} \tag{5.5}$$

where, $x_{O_2,rc}$, $x_{N_2,rc}$ and $x_{NO,sc}$ are the mole fraction of O_2 in the reference chamber, the mole fraction of N_2 in the reference chamber, and the mole fraction of NO in the second chamber respectively.

5.3.1.2 Ohmic losses (η_Ω)

The ohmic loss is calculated as follows:

$$\eta_\Omega = R_{cell} \; i_{P2} \; A_{e2} \tag{5.6}$$

where R_{cell} is the cell ohmic resistance, i_{P2} is the NO_x sensing cell current density and A_{e2} is the cross sectional area of the NO_x sensing electrode. The ohmic resistance of Yttria Stabilized Zirconia (YSZ) electrolyte significantly decreases with temperature regardless of its thickness [163]. The ohmic loss, η_{Ω}, is neglected in this model due to the high sensor operating temperature (1023 K) and the very low value of cell current.

5.3.1.3 Activation-transportation polarization (η_{ac})

The activation-transportation polarization, is calculated using the Butler-Volmer equation [164]. According to the Butler-Volmer equation, the relation between the second chamber pumping current density (i_{P2}) and the activation-concentration polarization is:

$$i_{P2} = i^{o}_{P2}\left(\frac{x_{NO,sc}}{x^{o}_{NO,sc}}\right)^{\gamma}\left[exp\left(\frac{\alpha_{a2}F}{\bar{R}T}\eta_{ac}\right) - exp\left(\frac{-\alpha_{c2}F}{\bar{R}T}\eta_{ac}\right)\right] \tag{5.7}$$

In Eqn. (5.7), α_{a2} and α_{c2} are the charge transfer coefficient of anode and cathode respectively, while i_{P2}, i^{o}_{P2} and $x^{o}_{NO,sc}$ are the NO_x sensing cell current density; the reference exchange current density; and the reference mole fraction of NO in the second chamber that corresponds to the reference NO concentration in the sample gas. The overpotential η_{ac} is defined as $\eta_{ac} = V_{P2} - E_{OC2}$, where V_{P2} and E_{OC2} are the potential and the open circuit (zero-current) potential of the NO_x sensing cell. The concentration ratio is raised to the power of γ which reflects the effect of concentration losses. The reference NO concentration in this model, is constant and corresponds to the highest (2820 ppm) of NO in the sample gas.

5.3.1.4 Diffusion

Diffusion plays a pivotal role in the operation of amperometric sensors and must be included as one of the main components of the model. It is assumed that O_2 has been completely removed by the first chamber and all NO_2 molecules are converted to NO. The only species that is reduced in the second chamber is NO which diffuses through the second diffusion barrier. Each NO molecule transfers two electrons according to Eqn. (5.1a). Therefore, according to Faraday's law, the pumping current of the NO_x sensing cell is:

$$I_{p_2} = i_{P2}\ A_{e2} = 2FN_{NO,sc} \tag{5.8}$$

in Amperes where $N_{NO,sc}[\frac{mol}{s}]$ is the molar flow of NO through the second diffusion barrier to the second chamber.

The relative molar flux of NO can be estimated using Fick's law [150]:

$$N_{NO,sc} = -C_t D_{NO} A_{D2} \frac{x_{NO,fc} - x_{NO,sc}}{L_{D2}} \tag{5.9}$$

where $N_{NO,sc}$, $x_{NO,fc}$ and $x_{NO,sc}$ are the molar flow vector and the mole fraction of NO in the first and the second chamber respectively, L_{D2} is the length of the second diffusion barrier, A_{D2} is the cross sectional area of the second diffusion barrier, D_{NO} is the diffusion coefficient of NO calculated in [50], and C_t is the total molar concentration in $\frac{mole}{m^3}$ which according to the ideal gas law is:

$$C_t = \frac{P}{\bar{R}T} \tag{5.10}$$

where P is the absolute pressure in Pa.

The limiting current value, is the maximum possible cell current determined from diffusion which according to Eqn. (5.9) corresponds to the lowest molar fraction of NO in the second chamber ($x_{NO,sc} = 0$). Combining Eqn. (5.8) and (5.9), the pumping current of the NO_x sensing cell becomes:

$$I_{P2} = i_{P2}\ A_{e2} = -2FC_tD_{NO}A_{D2}\frac{x_{NO,fc} - x_{NO,sc}}{L_{D2}} \tag{5.11}$$

5.3.2 Modeling NO reduction in the first chamber

Due to the observed NO reduction current in the first chamber at low I_{P2} currents, a model of the first chamber that can be coupled to the second chamber, is needed.

5.3.2.1 O_2 sensing cell electrochemical model

Although NO is usually assumed not reduced in the first chamber, our experiments show that NO is indeed partly reduced in this chamber. This can affect the sensor behavior, at very low NO_x sensing cell pumping current ($I_{P2} \approx 0$). As the NO_x sensing cell current reduces to zero, the molar flux of NO through this cell also reduces to zero, according to Eqn. (5.8). This means that at zero NO_x sensing cell current, there is no gradient in NO through the second diffusion barrier, according to Eqn. (5.9) (also see Figure 5.5).

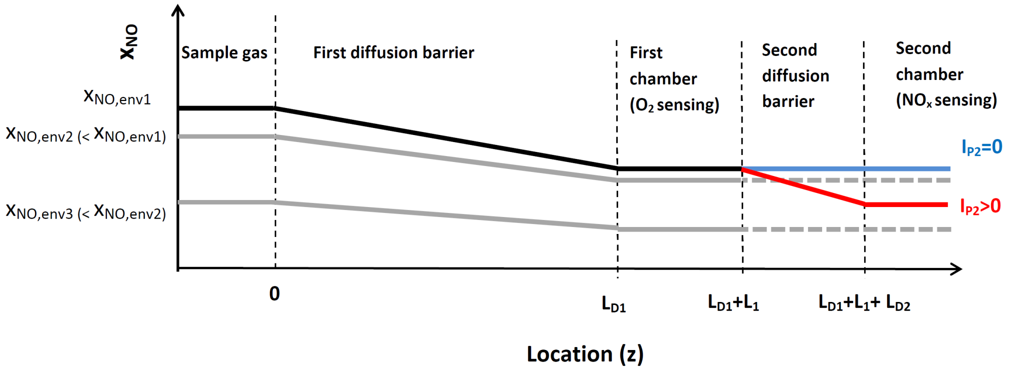

Figure 5.5: NO mole fraction gradient inside the NO_x sensor at different NO concentrations in the sample gas

A model is developed to estimate the NO concentration that would reach the second chamber to consider the effect of partial reduction of NO in the first chamber on the NO_x sensing cell behavior (the second chamber).

In the first chamber, NO is reduced through the following reactions:

$$Cathode : NO_{fc} + 2e^- \rightarrow \frac{1}{2}N_2 + O^{2-} \tag{5.12a}$$

$$Anode : O^{2-} + \frac{1}{2}N_2 \rightarrow NO_{env} + 2e^- \tag{5.12b}$$

$$Overall : NO_{fc} \rightarrow NO_{env} \tag{5.12c}$$

where NO_{fc} is the NO molecule inside the first chamber and NO_{env} is the NO molecule in the sample gas.

Using a similar approach to that in section 5.3.1.1, the effect of NO reduction on the first chamber cell voltage (V_{P1}) can be expressed by:

$$V_{P1} = \underbrace{E^o_{fc} + \frac{\Delta S_{ox-red,fc}}{2F}(T - T_o) - \frac{\bar{R}T}{2F} ln\left(\frac{p_{NO_{env}}}{p_{NO_{fc}}}\right)}_{E_N} - \eta_a \tag{5.13}$$

where, $p_{NO_{env}}$ and $p_{NO_{fc}}$ are the partial pressure of NO in the sample gas and in the first chamber respectively. In this case, E^o_{fc} and $\Delta S_{ox-red,sc}$ are both equal to zero [95]. Again, using Dalton's law of partial pressures [162], Eqn.(5.13) becomes:

$$V_{P1} = \underbrace{E^o_{fc} + \frac{\Delta S_{ox-red,fc}}{2F}(T - T_o) - \frac{\bar{R}T}{2F} ln\left(\frac{x_{NO,env}}{x_{NO,fc}}\right)}_{E_N} - \eta_a \tag{5.14}$$

where, $x_{NO,env}$ and $x_{NO,fc}$ are the molar fraction of NO in the sample gas and in the first chamber respectively.

5.3.2.2 Activation overpotential

The first chamber cell potential is kept at a high value (>0.42 V). Therefore, the activation is calculated using a Tafel approximation which is valid at high cell voltages [95]:

$$\eta_a = \frac{\bar{R}T}{\alpha_1 F} ln\left(\frac{i_{P1,NO}}{i^o_{P1}}\right) \tag{5.15}$$

where, $i_{P1,NO}$ and i^o_{P1} are the current density and the exchange current density of the first cell respectively and α_1 is the charge transfer coefficient of the first cell.

5.3.2.3 Diffusion

All the NO that comes through the first diffusion barrier is reduced either in the first or the second chamber. Therefore, according to the Faraday's law, the molar flux of NO through the first diffusion barrier, $N_{NO,fc}$ has the following relation between the first and the second cell pumping currents:

$$\underbrace{i_{p_1,NO} A_{e1}}_{I_{p_1,NO}} + \underbrace{i_{p_2} A_{e2}}_{I_{p_2}} = 2F N_{NO,fc} \tag{5.16}$$

where, A_{e1} and A_{e2} are cross sectional area of the first and the second chamber electrodes respectively. The current $I_{p_1,NO}$ only considers the effect of NO on the first cell pumping current. In the presence of O_2, the value $I_{p_1,NO}$ is at least three orders of magnitude lower than the overall I_{p1} value [50] and does not significantly effect the sensor sensitivity to O_2. Thus, the model parameter estimation tests are carried out in the absence of O_2 in the sample gas.

The relative molar flux of NO can be estimated using Fick's law [150]:

$$N_{NO,fc} = -C_t D_{NO} A_{D1} \frac{x_{NO,env} - x_{NO,fc}}{L_{D1}} \tag{5.17}$$

where, $N_{NO,fc}$ is the molar flux vector through the first diffusion barrier, $x_{NO,env}$ is the mole fraction NO in the sample gas, A_{D1} is the cross sectional area of the first diffusion barrier, and L_{D1} is the length of the first diffusion barrier. Combining Eqn. (5.16) and (5.17):

$$i_{p_1,NO}A_{e1} + i_{p_2}A_{e2} = -2FC_tD_{NO}A_{D1}\frac{x_{NO,env} - x_{NO,fc}}{L_{D1}} \tag{5.18}$$

5.3.3 $\mathrm{NO_x}$ sensor model by coupling the diffusion and the electrochemical models

To develop a comprehensive $\mathrm{NO_x}$ sensor model, diffusion and electrochemical equations for both chambers must be solved simultaneously. A set of coupled nonlinear equations are used to present the model in a standard form of f($\mathbf{x}$,$\mathbf{u}$, ζ, β)=0. The model inputs, variables and parameters are vectors which are listed next. The vector **u** contains three model inputs:

$$\mathbf{u} = \begin{bmatrix} V_{p1} & V_{p2} & x_{NO,env} \end{bmatrix}$$

The vector **x** contains four model variables (or states):

$$\mathbf{x} = \begin{bmatrix} x_{NO,fc} & x_{NO,sc} & i_{p1,NO} & i_{p2} \end{bmatrix}$$

The vector $\boldsymbol{\zeta}$ contains 23 model parameters (see Table 5.3):

$$\boldsymbol{\zeta} = \Big[T \; P \; E^o_{fc} \; E^o_{sc} \; \Delta S_{ox-red,fc} \; \Delta S_{ox-red,sc} \; x_{N_2,rc} \; x_{O_2,rc} \; A_{e1} \; A_{e2} \; A_{D1} \\ A_{D2} \; R_{cell} \; x^o_{NO,sc} \; i^o_{P1} \; i^o_{P2} \; \gamma \; \alpha_1 \; \alpha_{a2} \; \alpha_{c2} \; L_{D1} \; L_{D2} \; D_{NO} \Big]$$

The vector $\boldsymbol{\beta}$ contains three constants used in the model:

$$\boldsymbol{\beta} = \begin{bmatrix} F & \bar{R} & T_o \end{bmatrix}$$

All the model parameters and constants are listed in Table 5.3. The objective of this model is to find the variable vector $\mathbf{x}$ for the given model input vector $\mathbf{u}$. Since the variable vector $\mathbf{x}$ has four components, four equations are needed to find the variables. The four equations are obtained as follows:

$$\begin{cases} Eqn.\ (5.5)\ \&\ (5.7)\ combined \rightarrow f_1(\mathbf{x}, \mathbf{u}, \boldsymbol{\zeta}, \boldsymbol{\beta}) = 0 \\ Eqn.\ (5.11) \rightarrow f_2(\mathbf{x}, \mathbf{u}, \boldsymbol{\zeta}, \boldsymbol{\beta}) = 0 \\ Eqn.\ (5.14)\ \&\ (5.15)\ combined \rightarrow f_3(\mathbf{x}, \mathbf{u}, \boldsymbol{\zeta}, \boldsymbol{\beta}) = 0 \\ Eqn.\ (5.18) \rightarrow f_4(\mathbf{x}, \mathbf{u}, \boldsymbol{\zeta}, \boldsymbol{\beta}) = 0 \end{cases}$$

with,

$$\begin{aligned} f_1(\mathbf{x}, \mathbf{u}, \boldsymbol{\zeta}, \boldsymbol{\beta}) = -u_2 + \zeta_4 + \frac{\zeta_6}{2\beta_1}\left(\zeta_1 - \beta_3\right) - \frac{\beta_2\zeta_1}{2\beta_1} ln\left(\frac{\zeta_7^{0.5}\zeta_8^{0.5}}{x_2}\right) \\ -\zeta_{13}x_4\zeta_{10} - \frac{\beta_2\zeta_1}{\frac{\zeta_{19}+\zeta_{20}}{2}\beta_1} sinh^{-1}\left(\frac{x_4}{2\zeta_{16}(\frac{x_2}{\zeta_14})^{\zeta_{17}}}\right) = 0 \end{aligned} \qquad (5.19)$$

$$f_2(\mathbf{x}, \mathbf{u}, \boldsymbol{\zeta}, \boldsymbol{\beta}) = x_4\zeta_{10} + 2\beta_1\left(\frac{\zeta_2}{\beta_2\zeta_1}\right)\zeta_{23}\zeta_{12}\frac{x_1 - x_2}{\zeta_{22}} = 0 \qquad (5.20)$$

$$f_3(\mathbf{x}, \mathbf{u}, \boldsymbol{\zeta}, \boldsymbol{\beta}) = -u_1 + \zeta_3 + \frac{\zeta_5}{2\beta_1}\left(\zeta_1 - \beta_3\right) - \frac{\beta_2\zeta_1}{2\beta_1} ln\left(\frac{u_3}{x_1}\right) - \frac{\beta_2\zeta_1}{\zeta_{18}\beta_1} ln\left(\frac{x_3}{\zeta_{15}}\right) = 0 \qquad (5.21)$$

$$f_4(\mathbf{x}, \mathbf{u}, \boldsymbol{\zeta}, \boldsymbol{\beta}) = x_3\zeta_9 + x_4\zeta_{10} + 2\beta_1 \frac{\zeta_2}{\beta_2\zeta_1}\zeta_{23}\zeta_{11}\frac{u_3 - x_1}{\zeta_{21}} = 0 \tag{5.22}$$

5.4 Experimental setup

5.4.1 Internal Combustion Engines

To study the sensor behavior over a wide range of $\mathrm{NO_x}$ and other exhaust emission concentrations, the sensor was first mounted in the exhaust pipe of a four cylinder medium duty Tier III diesel engine (Cummins QSB 4.5 160) and then in the exhaust pipe of a four cylinder port injection spark ignition (SI) engine fueled with natural gas (GM Vortec 3000) as shown in Figure 3.4. The tests were carried out at different engine operating conditions with different $\mathrm{NO_x}$ concentrations in the exhaust system as listed in Table 5.1. The sensor was installed upstream of the engine aftertreatment systems to measure the engine raw emissions. The $\mathrm{NO_x}$ sensor used in the experiments was a production ECM $\mathrm{NO_x}$ sensor (P/N: 06-05). The sensor parameters and operating condition were changed using the corresponding control module (*ECM-NOxCANt* P/N: 02-07) connected to a computer via *Kvaser Light HS* CAN interface. More details of the experimental setup are in chapter 3.

All measurements were carried out once the engine and the sensor reached steady state operating conditions.

Table 5.1: Engine operating conditions and $\mathrm{NO_x}$ concentration in the exhaust gas. * The stoichimetric air/fuel ratio is changed to change the level of $\mathrm{NO_x}$ emission in the SI engine

Engine	Engine speed [rpm]	Engine output torque [ft-lb]	$\mathrm{NO_x}$ mole fraction [$\times 10^{-6}$]
Diesel	2500	30	165
Diesel	2000	100	280
Diesel	1500	200	590
SI	2000	118	750, 1310, 1800, 2200, 2820*

5.4.2 Gas mixture test rig

To make sure that the sensor behavior is not affected by the other exhaust gas species, specially O_2 and NO_2, a sensor test rig was built based on a design from ECM [128]. The test rig consists of six externally-controlled 2-way valves, three externally-controlled 3-way valves, four humidifying tanks and six CCR MKS-GE50A mass flow controllers, connected to gas cylinders filled to known concentrations. All of the setup actuators are externally controlled by a PC as schematically shown in Figure 3.13. To have a better control of NO_x concentration, the water tanks are bypassed for all the tests carried out on the sensor test rig. The sensor tests are carried out with the sensor test rig using NO/N_2 mixture at different NO concentrations.

5.5 Results and discussion

The sensor was tested over a wide range of operating conditions to study the behavior of the NO_x sensing cell and to observe the effect of all important factors on the sensor output. To do this, the sensor temperature was kept at the stock sensor temperature in normal operation (T= 1023 K). Then, the NO_x sensing cell voltage, V_{P2} was changed to cover regions (I to V) in Figure 5.4 (not region VI). These tests were performed at different engine operating points with different NO_x concentrations up to approximately 2800 ppm ($x_{NO,env} = 2800 \times 10^{-6}$).

5.5.1 Activation polarization parameters for the first cell (O_2 sensing cell)

To investigate partial reduction of NO in the first chamber (O_2 sensing chamber), several tests were carried out with the sensor test rig in the absence of O_2. First, the open-circuit (zero-current) potential of the second cell (NO_x sensing cell) was found through the experiments at different NO_x concentrations in the sample gas. Theoretically, it is equal to the Nernst potential, E_N, defined in Eqn. (5.5). Since the second cell pumping current (i_{P2}) is equal to zero, the mole fraction of NO in the first and the second chamber are equal. Then, using the experimental open-circuit potential of the second cell at different NO_x concentrations, the mole fraction of NO in the second chamber, $x_{NO,sc}$, can be estimated using Eqn. (5.5) with η_{ac} and η_Ω set to zero. Then, the kinetic parameters for the first chamber, α_1 and i^o_{P1}, are obtained by fitting i_{P1} using Eqn.(5.15) where Eqn. (5.14) is used to estimate the overpotential, η_a as illustrated in Figure 5.6.

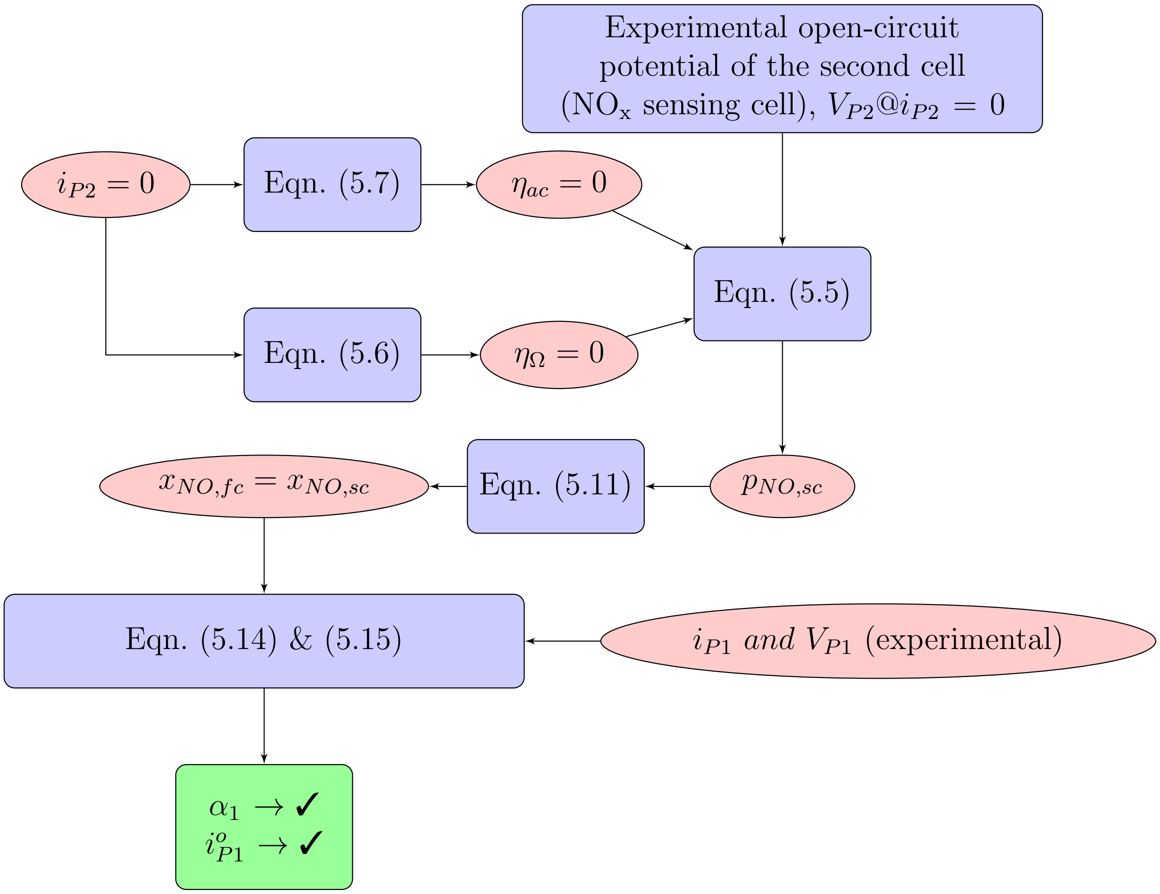

Figure 5.6: Defining the activation polarization parameters for the first cell

The effect of NO concentration on the first sensing cell current, $I_{P1,NO}$, was studied to evaluate the role of the first sensing cell in NO reduction at zero NO_x sensing cell current (I_{P2}=0) and the results are shown in Table 5.2. All the tests were carried out on the sensor test-rig in the absence of O_2 at different NO concentrations balanced with N_2 .

Table 5.2: The effect of NO concentration on the pumping current of the first chamber in the absence of O_2 and @I_{P2}=0

$x_{NO,env}$	$I_{P1,NO}$ [μA]	V_{P1} [V]
0	0	0.375
100×10^{-6}	1	0.38
1140×10^{-6}	2	0.423
2800×10^{-6}	5	0.465

The I_{P1} measurement system is designed by the sensor manufacturer for measuring O_2 concentration and therefore does not have an appropriate resolution for measuring low currents. Therefore, the tests are carried out only at points that have a recognizable effect on I_{P1}.

I_{P1} increases with the sample gas NO concentration as shown in Table 5.2. The test results confirm that NO is partly being reduced in the first chamber affecting NO concentration gradient inside the sensor compartments including the NO_x sensing cell, when I_{P2} is equal to zero. Using the data in Table 5.2 and the process above, the resulting activation polarization parameters for the first chamber were determined and are listed in Table 5.3.

The use of Eqn. (5.14) is needed because the first sensing cell voltage is not fixed and changes slightly to keep the reference cell voltage constant through a closed loop controller. Activation polarization parameters for NO reduction in the first chamber are found based on the experimental open-circuit potential of species in the second chamber for three NO concentrations along with the corresponding first cell voltage, V_{P1}, as listed in Table 5.2. The value of V_{P1} is linearly interpolated for the concentrations between the measured points listed in Table 5.2.

5.5.2 Activation polarization parameters for the second chamber

Generally, the activation polarization becomes the rate-determining step of the species reduction/oxidation when the current density is very low and the concentration of reduced/oxidized species is high. Therefore, the NO_x sensing cell behavior should be studied at very low current densities to find the activation polarization parameters for the model.

As discussed in section 5.5.1, the first sensing cell plays a pivotal role in determining the open-circuit potential of the second sensing cell by changing the mole fraction of NO through the sensor compartments as schematically shown in Figure 5.5. The first cell potential, V_{P1} increases with the NO_x concentration in the sample gas as shown in Table 5.2. This reduces mole fraction of NO inside the first and the second chamber according to Eqn. (5.14) which makes the open-circuit potentials to converge at high concentrations as shown in Figure 5.7 and schematically illustrated in Figure 5.5. The error bars in Figure 5.7 represent the uncertainty of the effect of NO_x concentration on the second cell open-circuit potential. This uncertainty decreases as the NO_x concentration in the environment increases.

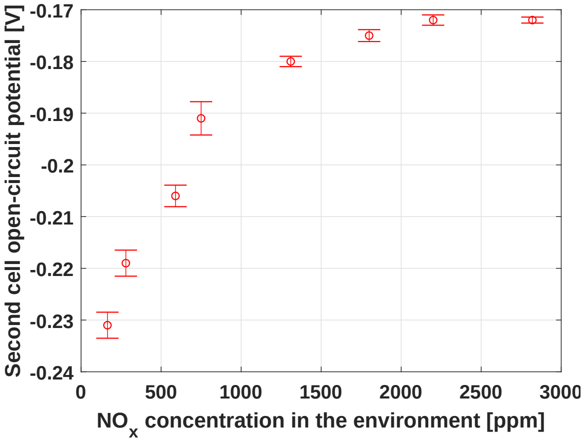

Figure 5.7: Experimental open-circuit potential of the NO_x sensing cell

The cell behavior at high concentration (2820 ppm) and very low current densities

(<0.2 [A/m^2]) was used to find the parameters of activation loss, i.e. i^o_{P2}, α_{a2} and α_{c2} as shown in Figure 5.8, considering the corresponding mole fraction of NO at this operating condition as the reference mole fraction ($x^o_{NO,sc}$). The cell overpotential is defined as $\eta = E_{cell} - E_{N,exp}$, where $E_{N,exp}$ is the experimental open-circuit cell potential. A Butler-Volmer fit has been carried out using a trust-region algorithm [165] with squared correlation coefficient (R^2) of 0.9736 and Root Mean Square Error (RMSE) of 0.01512. The cell current density, i_{P2}, is obtained from the experimental measurements. All the Butler-Volmer fit parameters are listed in Table 5.3.

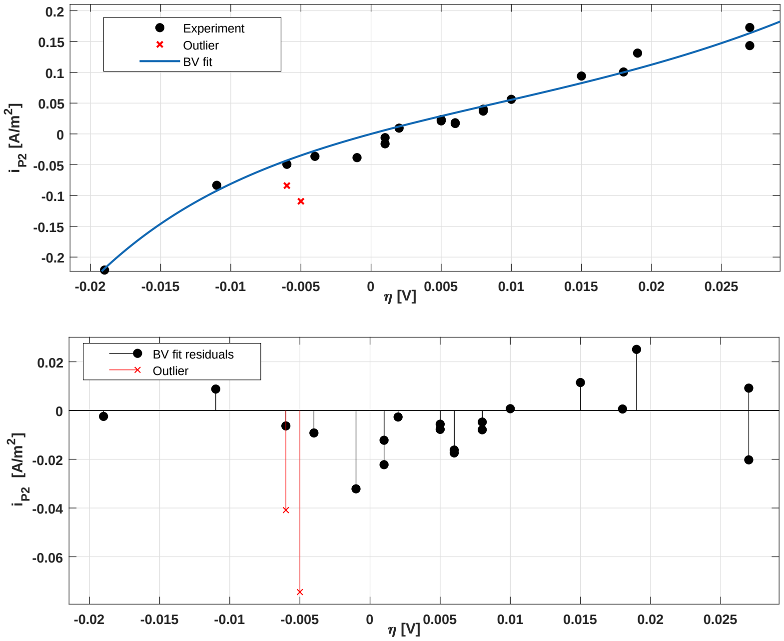

Figure 5.8: Butler-Volmer fit for 2820 ppm NO concentration in the environment ($x_{NO,env} = 2820 \times 10^{-6}$)

5.5.3 Model Validation

To validate the model capability to predict sensor behavior at different cell voltages and different NO$_x$ concentrations, the sensor is mounted on the exhaust system of a Diesel and SI engine as explained in chapter 3. Different engine operating conditions with different NO_x concentrations listed in Table 5.1 are tested. All the engine tests are carried out at steady state engine operating condition, where the engine is fully warmed up. To maintain steady state, the engine output torque was controlled by a dynamometer at the set points listed in Table 5.1, while the engine speed was controlled by the engine controller. After the engine reached steady state operating condition, the second cell potential was changed using the NO_x sensor control module via the *Kvaser Light HS* CAN interface. The NO_x sensing cell potential was changed to cover the full operating range at each NO_x concentration set point. To do this, the potential was varied from the open circuit potential to the diffusion rate-determining operating condition. The operating conditions and sample gas conditions of each test were applied to the sensor model as the inputs (V_{P1}, V_{P2}, $x_{NO,env}$) where, V_{P1} and V_{P2} are the sensor operating condition inputs and $x_{NO,env}$ is the boundary condition applied to the model. The boundary condition values are listed in Table 5.1. The actual sensor temperature and cell voltage were measured and used as the inputs for the diffusion model and the electrochemical model. The model was then used to predict the sensor current at different diesel and SI engine operating conditions with different NO_x concentrations listed in Table 5.1 and at different NO_x sensing cell potentials to evaluate the accuracy of the model in predicting the effect of model inputs (V_{P1}, V_{P2}, $x_{NO,env}$) on the measureable output (i_{P2}).

The experimental and the model output results for the NO_x sensing cell are shown in Figure 5.9 with symbols representing the data and the lines representing the model.

The effect of water vapor and the other exhaust gas species (such as CO_2, unburned hydrocarbons, particulate matters, etc) on the model boundary condition is considered since all these species contribute to NO_x dilution inside the exhaust gas. However, the cross sensitivity of the NO_x sensor to water vapor is neglected in the model which could be one of the factors affecting the model accuracy at some operating conditions shown in Figure 5.9. The model results match the experimental data

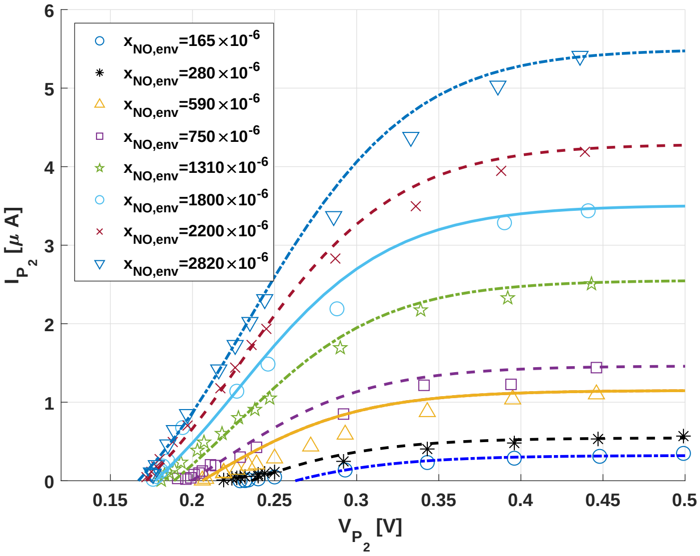

Figure 5.9: Experiments and simulation results of the sensor pumping current, I_{p2} vs cell voltage at different NO_x concentrations in the environment

with maximum error of 12 % at $V_{P_2} = 0.29$ V and [NO_x]= 1800 ppm as shown in Figure 5.9. As the cell voltage increases, more NO is reduced on the cathode electrode inside the sensing chamber which reduces the mole fraction of NO inside the chamber based on Eqn. (5.5). Reduction of NO directly changes the NO gradient inside the sensor and makes it easier to estimate the mole fraction of NO inside the NO_x sensing chamber. Finally, the sensor pumping current reaches its maximum value limited by the diffusion of species through the sensor porous diffusion barriers, which is accurately captured by the model as shown in Figure 5.9. The experimental results of the second sensing cell test are listed in Appendix B.

5.6 Chapter summary

The full range of the sensing cell current-voltage curve of an amperometric NO_x sensor was experimentally studied and then simulated. First, diffusion of the sample gas species through the sensor porous diffusion barriers and sensor chambers were modeled. Then, the diffusion model was coupled to an electrochemical model to predict the current-voltage curve of the NO_x sensing cell. The ohmic loss, activation loss and concentration loss have been included in the electrochemical submodel. To validate the sensor model at different operating conditions, the sensor was installed on the exhaust pipe of a medium duty 4.5 L Diesel engine, a 3 L port injection spark ignition engine and a sensor test-rig that provides fully controlled gas mixtures. Experiments were carried out at different engine operating conditions to provide a wide range of NO_x concentrations for NO_x sensor model validation. The sensor model consists of 4 non-linear equations with 3 inputs, 23 physics-based parameters and 3 constants. The NO_x sensing cell voltage was changed from the open-circuit cell voltage, which corresponds to zero current density, to 0.45 V that corresponds to the limiting current of the NO_x sensing cell.

It is shown that NO partially reduces in the first chamber which affects the NO_x sensing cell open-circuit potentials. The experimental open-circuit potential at different concentrations were defined and then implemented in the model to simulate NO reduction in the first chamber at $I_{P2} = 0$. The model results for the limiting current and the pumping current of the NO_x sensing cell, closely match the experiments for a wide range of cell voltages and different engine operating points with different NO_x concentrations up to more than 2800 ppm.

Table 5.3: Model parameters and constants. Estimated parameters are from physics-based models explained in the chapter.

Parameter	**Description**	**value**	**Source**
T	Sensor temperature	1023 [K]	Measured
P	Sample gas pressure	1 [atm]	Measured
E^o_{fc}	open-circuit potential at the standard state for the first chamber	0 [V]	Calculated [95]
E^o_{sc}	open-circuit potential at the standard state for the second chamber	0.4487 [V]	Calculated [95]
$\Delta S_{ox-red,fc}$	The change in entropy of products reactants for the first chamber	0 $[\frac{J}{mole.K}]$	Calculated [95]
$\Delta S_{ox-red,sc}$	The change in entropy of products -reactants for the second chamber	-12.5325$[\frac{J}{mole.K}]$	Calculated [95]
$x_{O_2,rc}$	O_2 mole fraction in the reference chamber	0.10 [-]	Assumption
$x_{N_2,rc}$	N_2 mole fraction in the reference chamber	0.90 [-]	Assumption
A_{e1}	First electrode cross sectional area	10.15×10^{-6}[m^2]	Measured
A_{e2}	Second electrode cross sectional area	2.59×10^{-6}[m^2]	Measured
A_{D1}	1st Diffusion barrier cross sectional area	1.81×10^{-7}[m^2]	Measured
A_{D2}	2nd Diffusion barrier cross sectional area	3.2×10^{-8}[m^2]	Measured
R_{cell}	Cell resistance	0 [Ω]	Estimated
$x^o_{NO,sc}$	Reference mole fraction of NO in the second chamber	6.62×10^{-7} [-]	Estimated
i^o_{P1}	First cell exchange current density	0.0109[A/m^2]	Estimated
i^o_{P2}	Second cell exchange current density	0.0471[A/m^2]	Estimated
γ	Second cell power of concentration ratio	0.1 [-]	Estimated
α_1	First cell charge transfer coefficient	4.817 [-]	Estimated
α_{a2}	Second cell charge transfer coefficient for anode	4.15 [-]	Estimated
α_{c2}	Second cell charge transfer coefficient for cathode	7.5 [-]	Estimated
L_{D1}	Length of the first diffusion barrier	1.66 [mm]	Measured
L_{D2}	Length of the second diffusion barrier	0.71 [mm]	Measured
D_{NO}	Diffusion coefficient of NO through the sensor barriers	$7.1 \times 10^{-6}[\frac{m^2}{s}]$	Estimated
Constant	**Description**	**value**	**Source**
F	Faraday constant	96485.33 [C/mol]	[166]
$\bar{R}$	Universal gas constant	8.314 $[\frac{J}{mole.K}]$	[166]
T_o	Reference temperature	298.15 [K]	[166]

CHAPTER 6

NO_x SENSOR CROSS SENSITIVITY TO AMMONIA AND PROPANE

This chapter investigates the cross sensitivity of an amperometric NO_x *sensor to ammonia and proposes a physics-based model to remove this cross sensitivity. The chapter also includes developing an amperometric HC sensor by changing the operating parameters of a production* NO_x *sensor.*

6.1 Cross sensitivity to ammonia

As discussed in chapter 2, Urea-based selective catalytic reduction (SCR) is an effective technique to reduce the NO_x emissions and to satisfy future emission standard regulations for Diesel engines[7]. Measuring the NO_x concentration in the exhaust gas is essential for closed-loop control of SCR systems [69, 74, 75]. However, the commercial NO_x sensors are cross-sensitive to ammonia (NH_3) [68] and therefore the NO_x sensor reading can differ from the actual value when NH_3 is present [76]. Determining actual NO_x is an important challenge for controlling urea injection of SCR systems.

Cross sensitivity of commercial NO_x sensors to NH_3, makes it difficult to achieve maximum NO_x conversion in SCR control. The time delay in the urea or ammonia injection and SCR catalyst dynamics are other important factors that limit the performance of closed-loop SCR control [77]. Therefore, removing the sensor cross sensitivity to the contaminations in the exhaust gas, is crucial to improve the system performance and to reduce the emissions.

The comprehensive understanding of the sensor performance and working principles gained in this work, provides a foundation to reduce, to remove, or at least to predict the sensor cross sensitivity to the exhaust gas contaminations. Another way of removing the sensor cross sensitivity to the exhaust gas contaminations is estimating the concentration of the species that affect the sensor response by modeling the engine aftertreatment systems. In this section, a physics-based SCR model is employed to estimate NH_3 concentration downstream of a SCR system mounted on a diesel engine in order to reduce the cross sensitivity of a NO_x sensor to NH_3. Then, the cross sensitivity of an amperometric NO_x sensor to ammonia is experimentally studied under different sensor operating conditions and different ammonia concentrations.

6.1.1 Removing cross sensitivity of NO_x sensor to ammonia leakage downstream of a SCR system[1]

Depending on the sensor type (potentiometric, amperometric etc), the sensor design and the sensor operating parameters, the cross sensitivity factor can vary at different sensor or engine operating conditions. The cross-sensitivity factor of a NO_x sensor to NH_3 is taken as a constant by [167, 168] and a function of time by [76] and the normalized stoichiometric ratio by [73].

The focus of this section is removing the cross sensitivity by estimating the concentration of the ammonia in the exhaust gas around the NO_x sensor. To do so, a NO_x sensor is selected that has a wide range of cross sensitivity variation at different

---

[1] This subsection is partly based on: M. Aliramezani, C.R. Koch, and R.E. Hayes. Estimating tailpipe NO_x concentration using a dynamic NO_x/ammonia cross sensitivity model coupled to a three state control oriented SCR model. IFAC-PapersOnLine, 49(11):813,2016. [33]

operating conditions [158], so that different cross sensitivity cases are examined and the most appropriate one is selected and improved.

The available cross sensitivity removal cases are first evaluated. Then, a temperature-based function is derived for the cross sensitivity factor based on experimental data. The model is then improved for transients by adding a correction factor. A new parameter (normalized ammonia slip rate) is defined which is found to be an effective factor for cross sensitivity in transients. A three state control oriented SCR model is calibrated and used to predict NH_3 slip and the results are validated using experimental data.

Finally, the SCR model and the sensor model are coupled and NO_x concentration is estimated using the NO_x sensor signal decomposition. The validation results show that the model is capable of accurately estimating the actual NO_x concentration based on the NH_3 and NO_x concentration upstream of the SCR and the NO_x sensor signal located downstream of the SCR for the data tested.

6.1.1.1 Experimental setup

The experimental data in [158] is used to evaluate different cross sensitivity models. A schematic of experimental setup used in [158] is shown in Fig. 6.1. The NH_3 and NO_x sensors used in the experiment are Delphi and *Siemens VDO* respectively [70, 158].

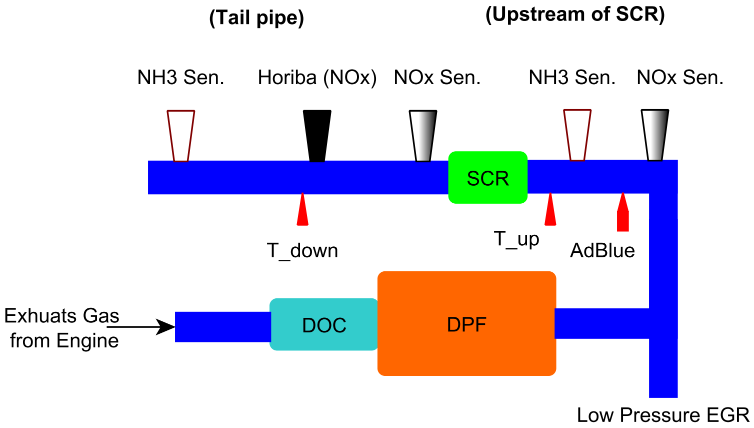

Figure 6.1: Exhaust after treatment system - Experimental setup

6.1.1.2 Cross sensitivity model

A linear form of a NO_x sensor cross sensitivity model is [169]:

$$\overline{C_{NO_x}} = C_{NO_x} + C_{CS}C_{NH_3} \tag{6.1}$$

Where, $\overline{C_{NO_x}}$ is the sensor output signal, C_{CS} is the cross sensitivity factor. C_{NO_x} and C_{NH_3} are NO_x and NH_3 concentrations respectively. Rearranging Eqn. (6.1), the actual NO_x concentration is:

$$C_{NO_x} = \overline{C_{NO_x}} - C_{CS}C_{NH_3} \tag{6.2}$$

The cross-sensitivity factor is taken to be: a constant [167, 168]; a function of time [76] and the normalized stoichiometric ratio [73]. However, commercial sensors are complex and as shown, these models can be improved for transient conditions or when there is large amounts of NH_3 slip. In this section, experimental data from the literature [158] is used to evaluate different cross sensitivity models. Two tests are chosen from the experimental data and are described in Table 6.1, with details in

[158].

Table 6.1: Engine tests description [158]

Test number	Test 1	Test 2
Engine speed range [rpm]	1700	1000
Engine torque range [Nm]	265-285	235-250
Gas Temperature before SCR [°C]	270-333	245-250
AdBlue Inj. Rate [mg/sec]	145	107

The measured values from Horiba MEXA 7500 gas analyzer after the SCR and NO_x concentration estimates for different constant cross sensitivity factors are shown in Fig. 6.2 and 6.3, where C_{NOx}, C_{NH_3} are measured from downstream of the SCR and the temperature is the exhaust gas upstream of the SCR. Both tests have transient Adblue (Ammonia) injection [158].

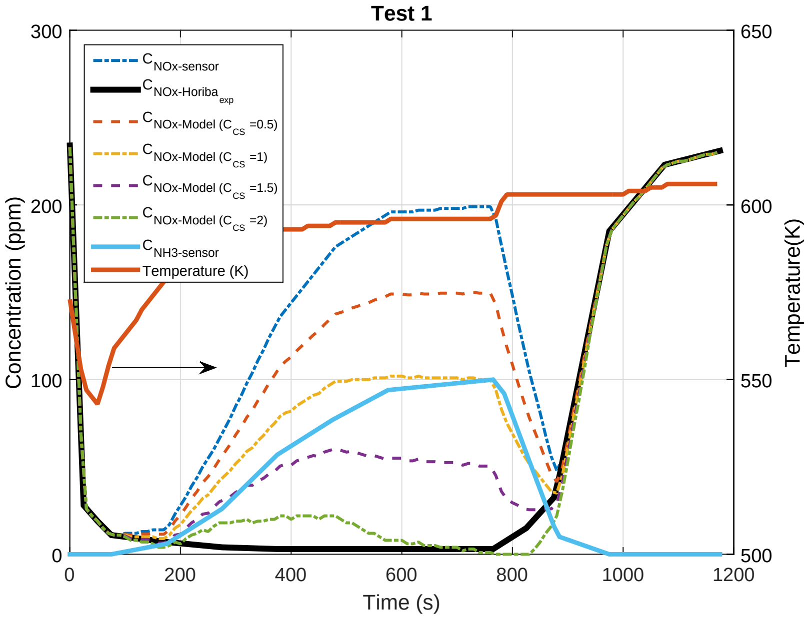

Figure 6.2: Modeled NO_x concentration (downstream of the SCR) for constant cross sensitivity factors vs. actual concentration - test 1

The actual NO_x concentration is taken as the measured value from Horiba gas analyser (the solid black line). The output signal from the production NO_x sensor (the dot-dashed blue line) shows a significant deviation from the actual NO_x concentration.

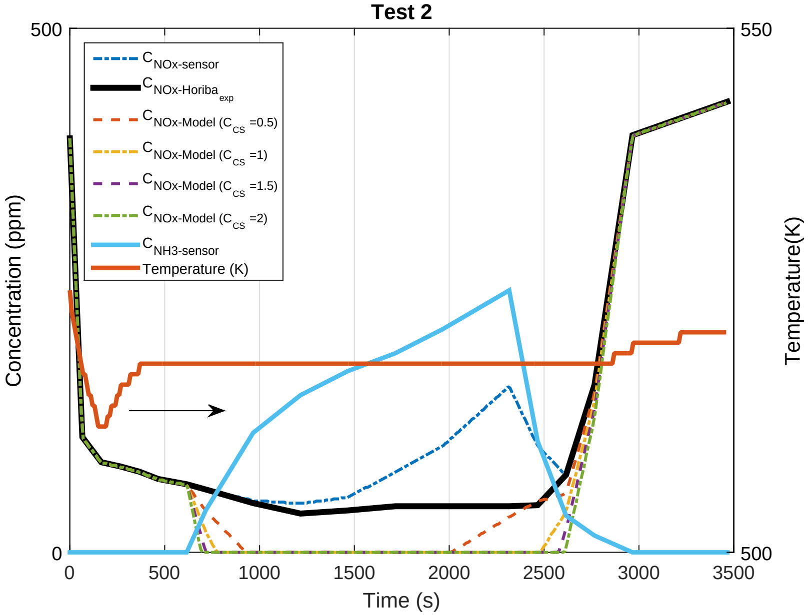

Figure 6.3: Modeled NO_x concentration (downstream of the SCR) for constant cross sensitivity factors vs. actual concentration - test 2

Since NH_3 is also measured by an ammonia sensor, different cross-sensitivity factors are checked using the ammonia slip and the NO_x sensor reading as shown in Fig. 6.2 and 6.3 for tests 1 and 2 respectively. The use of a constant cross sensitivity of 0.5, 1, 1.5 and 2 in Eqn. (6.2) are also shown as the four dashed lines. Even with constant cross sensitivity, the NO_x sensor model error is significant. This error is attributed to exhaust gas temperature deviation between the tests.

The cross sensitivity factor is found varying with exhaust gas temperature over a bounded range [76, 158]. The function *arctan(T)* is used as a simple function to describe the dependence on temperature (T). To achieve this

$$\overline{c_{CS}(T)} = a * arctan((T - b) * c) + d \tag{6.3}$$

is used for cross sensitivity as a function of temperature with T[K] and *a, b, c* and *d* are parameters which are fit to the experimented data from [158] and listed in Table 6.2.

Table 6.2: Calibrated parameters of the temperature-based cross sensitivity function, Eqn. (6.3)

Parameter	Value
a	0.65
b	550
c	0.1
d	1.087

The estimate of NO_x concentration for the two cases above including the temperature dependent cross sensitivity are shown in Fig. 6.4 and 6.5. Estimated NO_x has a maximum error of 34 ppm and 48 ppm for tests 1 and 2 respectively using a single cross sensitivity function. This is significantly lower error than with constant cross sensitivity.

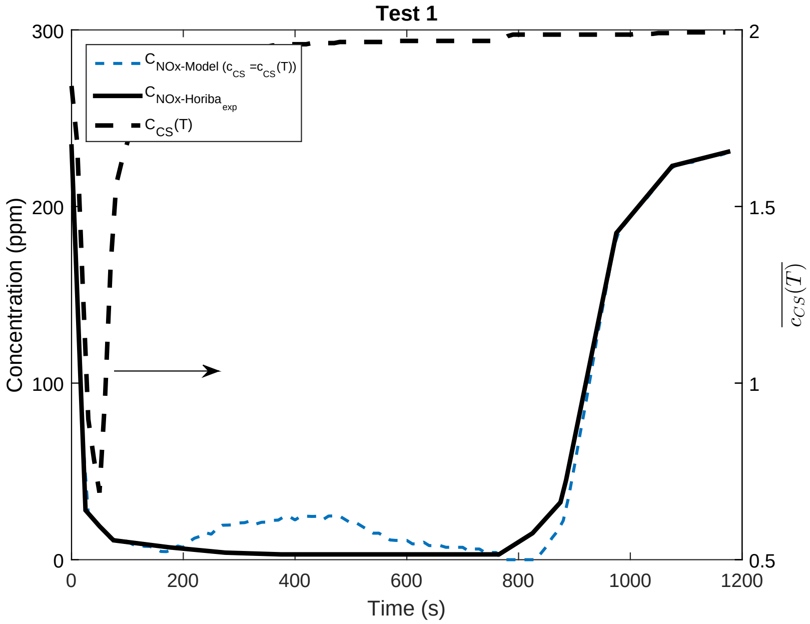

Figure 6.4: Modeled NO_x concentration from the temperature-based cross sensitivity ($\overline{c_{CS}(T)}$ - test1) - maximum error: 34 ppm

To further improve the model transient response, a normalized stoichiometric ratio (NSR) is used [73]. NSR is defined as the fraction of NH_3 concentration over

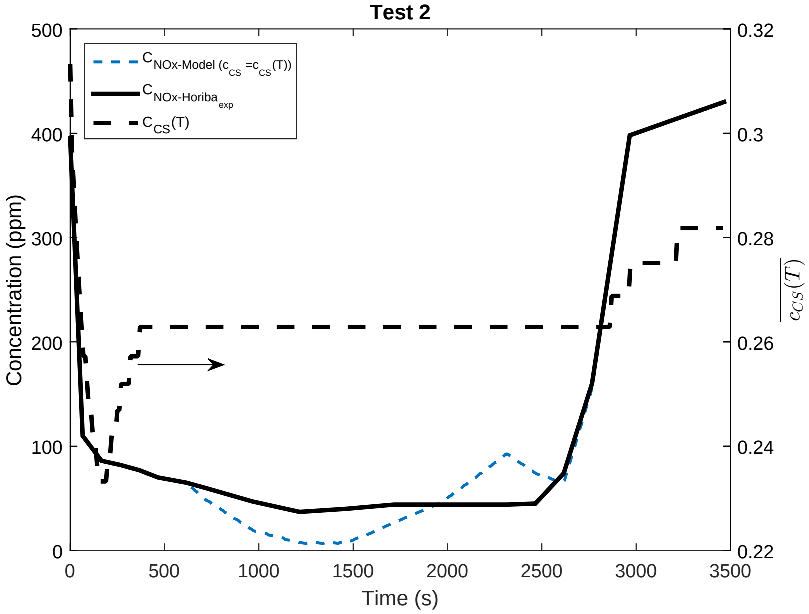

Figure 6.5: Modeled NO_x concentration from the temperature-based cross sensitivity ($\overline{c_{CS}(T)}$ - test2) - maximum error: 48 ppm

NO_x concentration:

$$NSR = \frac{C_{NH_3}}{C_{NO_x}} \tag{6.4}$$

However, as shown in Fig. 6.6 and 6.7, the relation between cross sensitivity and NSR is not static and changes with the time over the two tests.

To include time dependance, a new factor is proposed:

$$\beta = \frac{\frac{dC_{NH3}}{dt}}{C_{NH3}} \tag{6.5}$$

In Eqn. (6.5), C_{NH3} is the measured ammonia concentration from NH_3 sensor [158].

Then, $\overline{c_{CS}(T)}$ in Eqn. (6.3) is augmented to include a transient correction factor, $\overline{k(\beta)}$ as:

$$\overline{c_{CS}(T,\beta)} = \overline{k(\beta)}\ \overline{c_{CS}(T)} \tag{6.6}$$

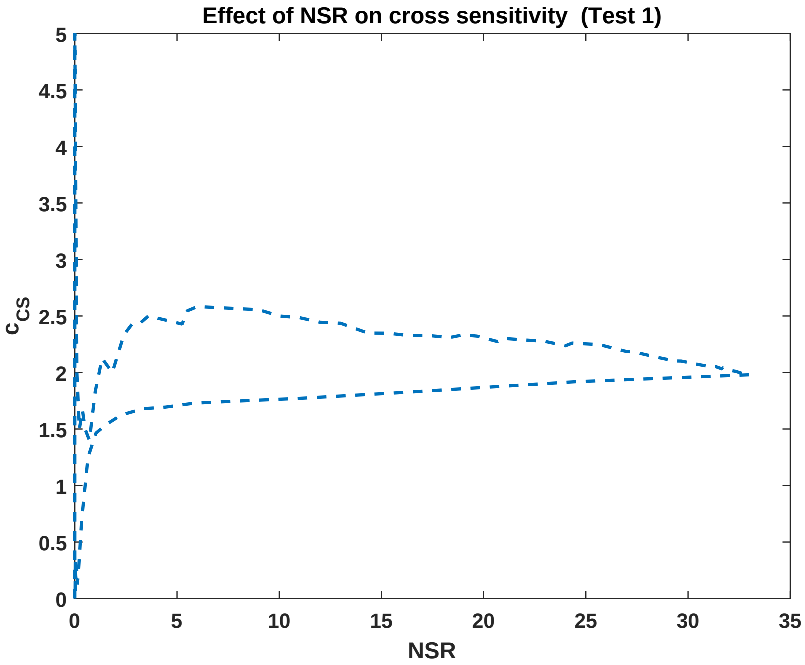

Figure 6.6: Effect of NSR on cross sensitivity (test1)

Where, $\overline{c_{CS}(T)}$ is calculated from Eqn. (6.3).

The calibrated values of $\overline{k(\beta)}$ from the experimented data for different ranges of β is shown in Table 6.3.

Table 6.3: Transient correction factor $\overline{k(\beta)}$ in Eqn (6.6)

β	$\overline{k(\beta)}$
> 0	1.1
$= 0$	1
< 0	0.8

The transient correction factor, $\overline{k(\beta)}$, adds step changes to the model when β changes sign. This is undesirable so a first order low pass filter is used with a time constant that is a function of temperature.

Considering β as a function of time, the first order low pass filter has the following form:

$$K(\beta(s), T) = \frac{1}{\tau(T)s + 1}\overline{K(\beta(s))} \tag{6.7}$$

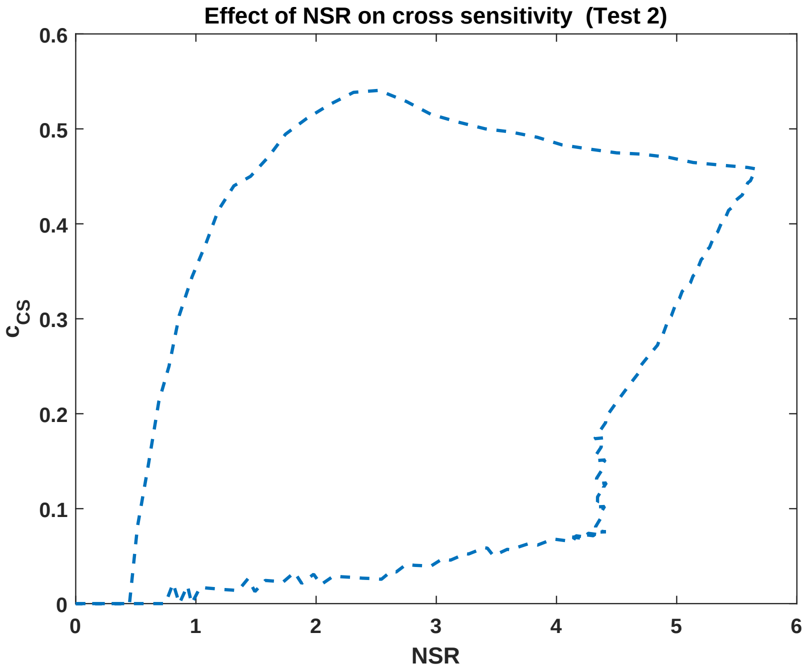

Figure 6.7: Effect of NSR on cross sensitivity (test2)

Then:

$$k(\beta, T, t) = \mathcal{L}^{-1}\{K(\beta(s), T)\} \tag{6.8}$$

The result from Eqn. (6.6) has the form:

$$c_{CS}(\beta, T, t) = k(\beta, T, t)\overline{c_{CS}(T)} \tag{6.9}$$

with T in Kelvin, t in seconds, $k(\beta, T, t)$ from Eqn. (6.7) and $\overline{c_{CS}(T)}$ from Eqn. (6.3).

The NO_x level using Eqn. (6.9) are shown in Fig. 6.8 and 6.9.

The model in Eqn. (6.9), follows the measured NO_x in Fig. 6.8 and 6.9 with a maximum overshoot (undershoot) of 10 (4) ppm and 45 (19) ppm instead of 34 (43) ppm and 48 (33) ppm for tests 1 and 2 respectively.

6.1.1.3 Selective Catalyst Reduction (SCR) Model

Chemistry of the De-NOx SCR process

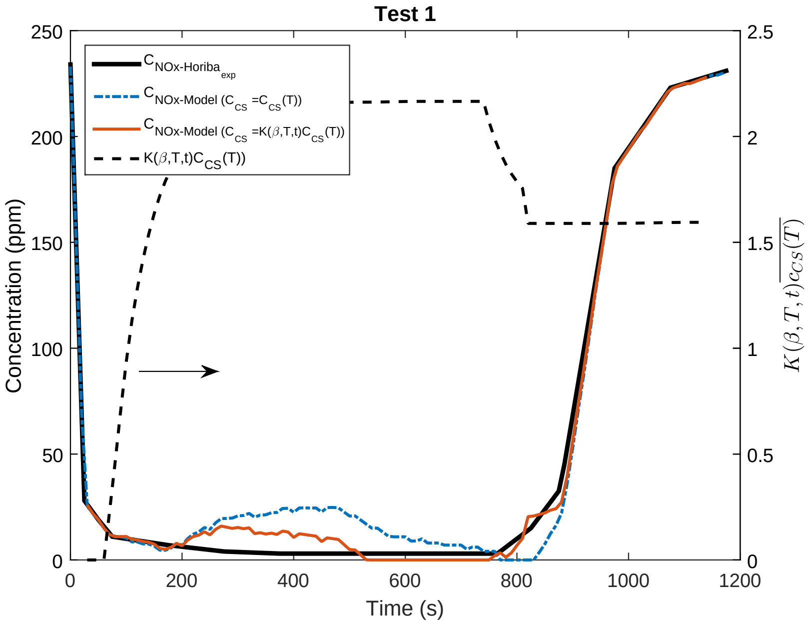

Figure 6.8: Modeled NO_x concentration - Maximum overshoot: 10 ppm, undershoot: 4 ppm (Eqn. (6.9), test1)

The main NO_x reduction reactions of SCR are described in section 2.1.3.

SCR reaction rates

The injected ammonia can be adsorbed on and desorbed from the SCR substrate. The kinetic rates of ammonia desorption and adsorption on the catalyst surface are calculated as [170]:

$$R_{des} = k_{des} exp(\frac{E_{des}}{\bar{R}T})\theta_{NH3} \tag{6.10}$$

$$R_{ads} = k_{ads} exp(\frac{E_{ads}}{\bar{R}T})C_{NH3}(1-\theta_{NH3}) \tag{6.11}$$

The reaction rate, R_{red}, of NO_x reduction is defined by [167]:

$$R_{red} = k_{red} exp(\frac{E_{red}}{\bar{R}T})C_{NOx}\theta_{NH3} \tag{6.12}$$

where, $\bar{R}$ is ideal gas constant, T is the temperature and k_{red} and E_{red} are two constants.

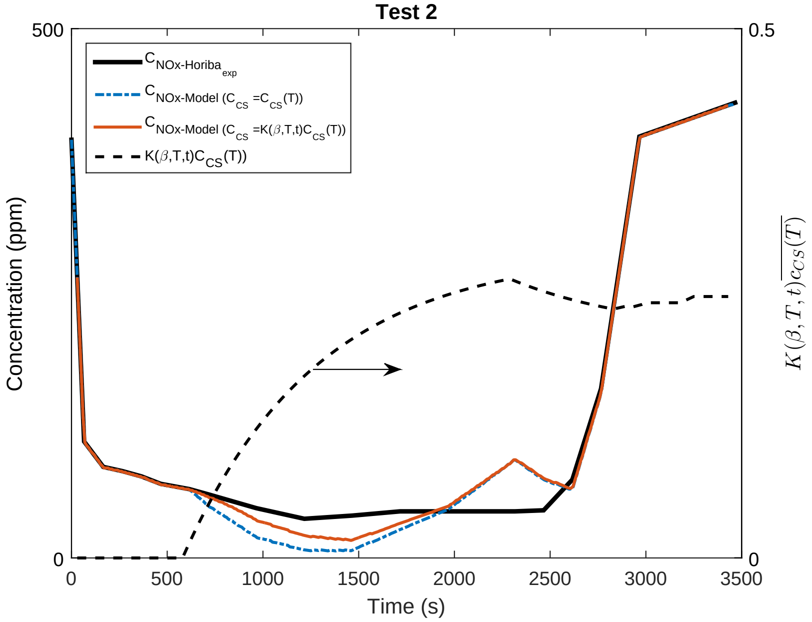

Figure 6.9: Modeled NO_x concentration - Maximum overshoot: 45 ppm, undershoot: 19 ppm (Eqn. (6.9), test2)

Another main reaction that should be considered is the NH_3 oxidation rate, R_{oxi}, which occurs at temperatures higher than 450 °C and is represented as [76]:

$$R_{oxi} = k_{oxi} exp(\frac{E_{oxi}}{\bar{R}T})\theta_{NH_3} \tag{6.13}$$

where k_{oxi} and E_{oxi} are two constants and θ is the ammonia surface coverage ratio defined as:

$$\theta_{NH_3} = \frac{M^*_{NH_3}}{\Theta} \tag{6.14}$$

$M^*_{NH_3}$ is the mole of ammonia stored on the SCR substrate surface and Θ is ammonia storage capacity (mole) described as [171]:

$$\Theta = S_1 exp(-S_2 T) \tag{6.15}$$

where S_1 and S_2 are constants.

SCR model formulation

A three-state nonlinear model was developed in [172] using tailpipe NOx and NH_3 concentration and ammonia surface coverage ratio with the states:

$$\begin{aligned}\begin{bmatrix}\dot{C}_{NOx}\\ \dot{\theta}_{NH_3}\\ \dot{C}_{NH_3}\end{bmatrix} &= \begin{bmatrix}f_1(C_{NOx},\theta_{NH_3},T,F)\\ f_2(C_{NOx},\theta_{NH_3},T,C_{NH_3})\\ f_3(C_{NH_3},\theta_{NH_3},T,F)\end{bmatrix}\\ &+\begin{bmatrix}0\\ 0\\ \frac{F}{V}\end{bmatrix}C_{NH_3,up}+\begin{bmatrix}\frac{F}{V}\\ 0\\ 0\end{bmatrix}C_{NOx,up}\end{aligned} \tag{6.16}$$

where,

$$f_1(C_{NOx},\theta_{NH_3},T,F) = -C_{NOx}(\Theta r_{red}\theta_{NH_3}+\tfrac{F}{V})+r_{oxi}\Theta\theta_{NH_3}$$

$$f_2(C_{NOx},\theta_{NH_3},T,C_{NH_3}) = -\theta_{NH_3}(r_{red}C_{NH_3}+r_{des}+r_{red}C_{NOx}+r_{oxi})+r_{ads}C_{NH_3}$$

$$f_3(C_{NH_3},\theta_{NH_3},T,F) = -C_{NH_3}(\Theta r_{ads}(1-\theta_{NH_3})+\tfrac{F}{V})+\Theta r_{des}\theta_{NH_3}$$

C_{NOx} and C_{NH_3} are tailpipe NO_x and NH_3 concentrations, respectively, $C_{NOx,up}$ and $C_{NH_3,up}$ are NO_x and NH_3 concentrations upstream of the SCR, respectively, $F[m^3/s]$ is the exhaust volume flow rate, $V[m^3]$ is the catalyst volume, $T[K]$ is exhaust gas temperature, Θ is calculated from Eqn. (6.15) and r_{des}, r_{ads}, r_{red} and r_{oxi} are defined as:

$$r_i = \frac{R_i}{\theta}, \qquad i = des, ads, red, oxi \tag{6.17}$$

SCR Model Validation

To calibrate the parameters and validate the SCR model for different operating conditions, results from the literature [158] are used.

Simulated and experimental values of NH_3 slip for test 1 are shown in Fig. 6.10.

According to Fig. 6.10, the simulated NH_3 slip (blue line) matches the measured values (yellow line) with maximum error of 21 ppm while the NH_3 concentration upstream of the SCR is the red line from [158].

NH_3 slip is the output of the SCR model that is used in the next section.

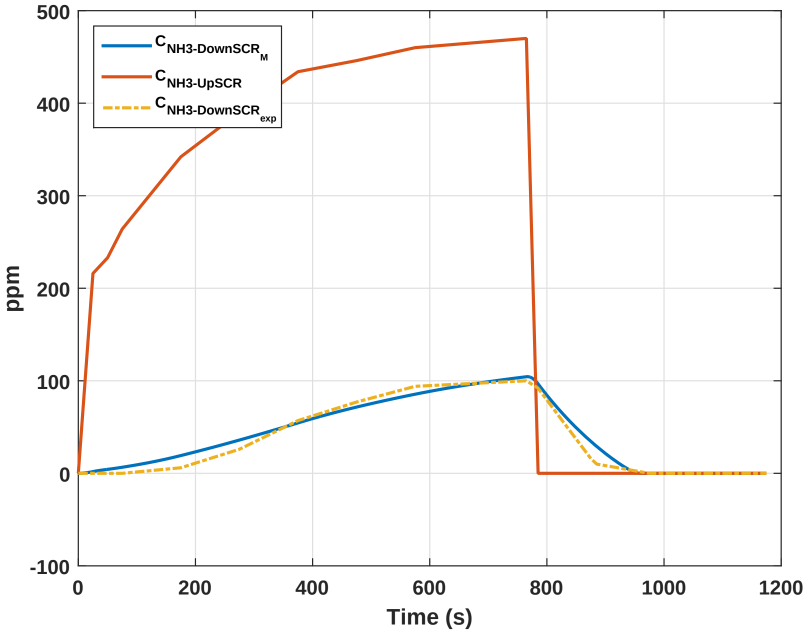

Figure 6.10: Predicted NH_3 concentration downstream of the SCR for test 1

6.1.1.4 Coupling SCR and NOx sensor model

The SCR and NO_x sensor models are now coupled to estimate the actual NO_x concentration based on NO_x sensor signal and exhaust gas temperature upstream and downstream of SCR. A Schematic of the coupled model is shown in Fig. 6.11, where, $T_{up,SCR}[K]$ is the exhaust gas temperature upstream of SCR.

As indicated in Fig. 6.11, NH_3 and NO_x concentration upstream of the SCR are both considered as inputs of the model. Although, in this model, NO_x concentration is measured by an accurate measurement device (Horiba MEXA 7500). For production engine management strategies, NH_3 and NO_x concentration at upstream of the SCR should be measured or estimated. A simple practical method is using a production NO_x sensor upstream of the Adblue injector and modeling NH_3 concentration based on the injected Adblue.

The simulated and experimental values of NH_3 slip from the coupled SCR and NOx sensor model are shown in Fig. 6.12 for test 1.

The final Ccs model (red line), Eqn. (6.9), has the closest value to the actual NOx concentration (black line) in comparison with all sensor models coupled to the SCR model as shown in Fig. 6.12. It should be noted that the error of all models consists of both sensor and SCR model errors.

6.1.1.5 Summary of ammonia cross sensitivity

In this section, ammonia cross sensitivity of a production NO_x sensor is modeled for slow transients. The most effective factors on cross sensitivity were evaluated to get the best accuracy against the experiments. The model is validated for large amounts of ammonia slip. A dynamic production NO_x sensor model is then developed to remove ammonia cross sensitivity and to decompose the NO_x sensor output signal. A basic model is derived for the cross sensitivity factor based on the experimental data as a function of exhaust gas temperature. The model is then improved for transients by considering a correction factor as a function of normalized ammonia slip rate (NASR). A three-state nonlinear control oriented SCR model is used to predict the NH_3 concentration downstream of the SCR. The SCR model and the sensor model are finally coupled and NO_x concentration is estimated using the NO_x sensor signal

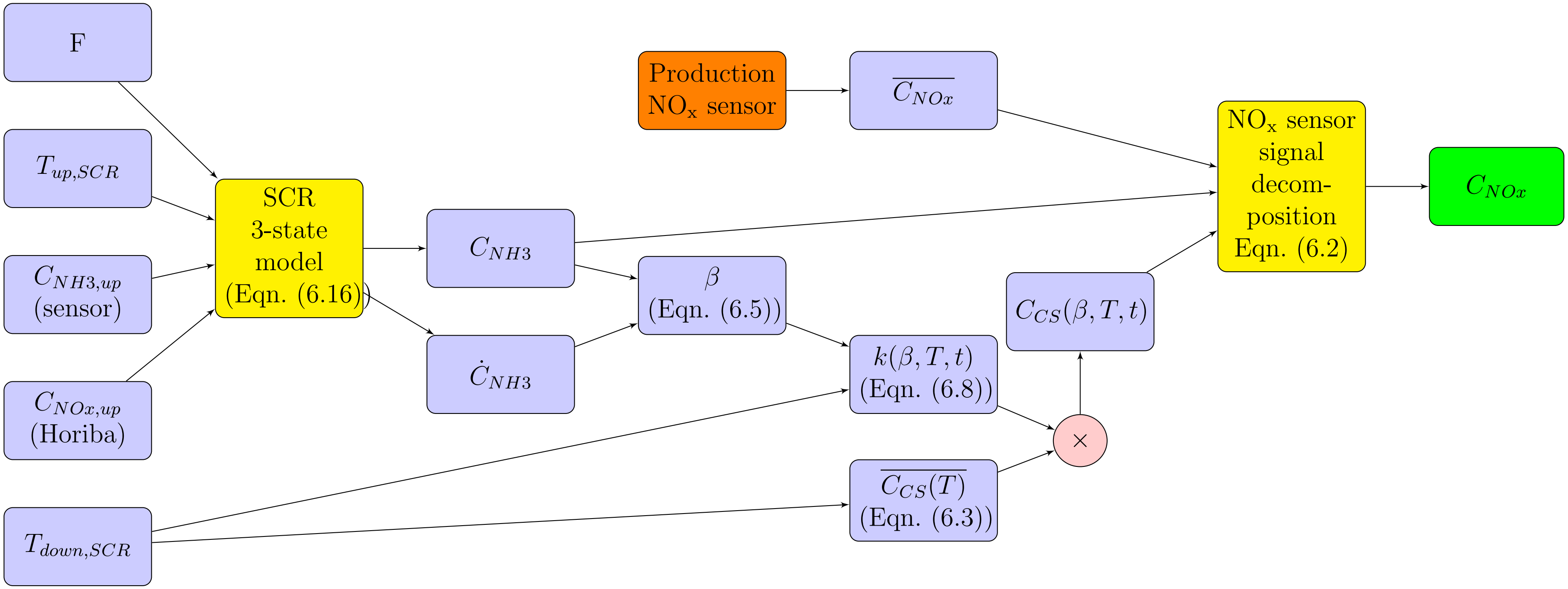

Figure 6.11: Coupled SCR and cross sensitivity model overview

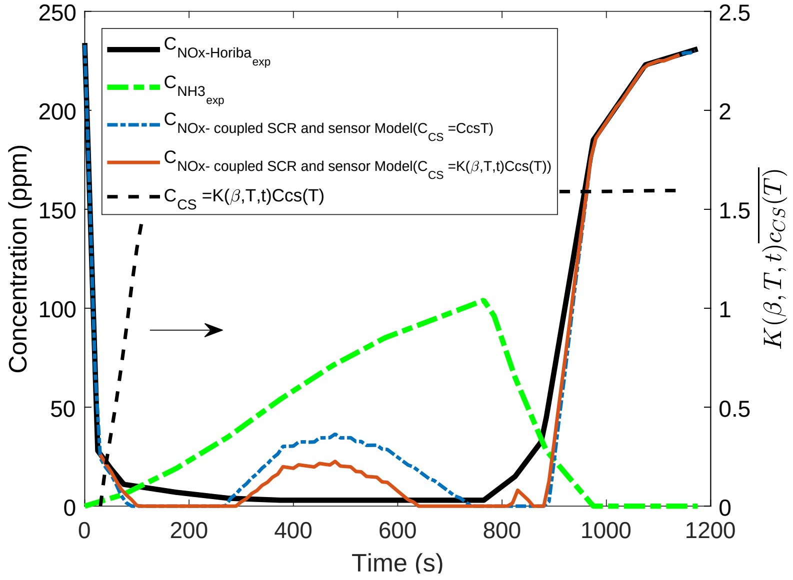

Figure 6.12: NOx concentration from coupled SCR and NOx sensor model for test 1

decomposition. The validation results confirms that the model is capable to accurately estimate the actual NO_x concentration based on the NH_3 concentration upstream of the SCR and the NO_x sensor output signal. This model can be used for future engine emission control strategies such as SCR control.

6.2 Cross sensitivity to hydrocarbons - A variable-potential limiting-current-type amperometric hydrocarbon sensor[2]

A limiting-current-type amperometric hydrocarbon sensor for rich conditions (in the absence of O_2) is developed in this section. To do this, an inexpensive three-chamber amperometric sensor with three separate electrochemical cells is parameterized to measure propane concentration. The sensor is tested using a controlled sensor test rig at different propane concentrations. This test rig was developed as a part of this thesis. The inputs to the sensor electrochemical cells have been modified to optimize

---

[2] This subsection is partly based on: *A variable-potential limiting-current-type amperometric hydrocarbon sensor* [52]

the sensor performance for measuring propane at different concentrations. First, the transient performance and stability of the sensor are optimized by changing the sensor temperature, the reference cell potential, and the stabilizing cell potential at a high propane concentration (5000 ppm - balanced with nitrogen). Over the range tested, the sensor has the longest stable output duration at the temperature of 1009 K, the reference cell potential of 0.67 V and the stabilizing cell potential of 0.45 V. After defining these optimized sensor operating parameters for the sensor temperature, the reference cell potential and the stabilizing cell potential, the sensor steady state behavior is studied to find the diffusion-rate-determined operating region.

Amperometric gas sensors (AGS)s belong to a promising group of electrochemical gas sensors that play a pivotal role in a wide range of industrial applications, including the automotive industry [50], medical [173, 174], and environmental monitoring [175, 176]. In an AGS, the sensor output signal is equal to the current generated by oxidation or reduction of species over the electrode-electrolyte interface. This current is typically measured at a fixed cell potential to obtain stable current value [177, 178]. Variable-potential AGS are also used in some applications such as wide-band O_2 sensors [179] to increase the sensor operating range.

The AGS current signal generally depends on the sensing cell potential, sensor temperature and the concentration of the measuring species [54, 180]. When the sensor temperature and the potential of an AGS sensing cell is set high enough, then the reaction rate becomes much faster than diffusion rate of species through the sensor diffusion barriers. In this case, the sensor current output is limited only by the diffusion of species. These sensors are called limiting-current type amperometric sensors. Limiting-current-type AGSs have much higher resolution than other types of electrochemical sensors and do not depend on chemical equilibrium at the electrode/electrolyte interface [181, 182].

Defining the optimal value of sensing cell voltage is essential to achieve the most stable sensor response. This is a trade-off since the sensing cell potential must be high enough to keep the reaction rates within the diffusion-rate-determining region [183], otherwise the sensor output signal will not be proportional to the concentration of the measuring species reducing the sensor accuracy. However, if the sensing cell voltage is too high, electrolyte decomposition takes place [127] which will not only reduce the sensor accuracy but can also damage the sensor. The value of optimal cell potential is also affected by manufacturing tolerances and sensor aging.

These drawbacks of fixed potential amperometric sensors can be solved by implementing a variable-potential sensing cell. Implementing a variable-potential sensing cell, facilitates controlling the partial pressure of the measuring gas species inside the sensing cell using a reference cell [110]. In this case, the sensing cell potential is changed to keep the reference cell potential at a constant value [140]. This is used in wide band lambda sensors where the oxygen concentration in the engine exhaust system is compared to the stoichiometric condition represented by the reference chamber set-point potential [109].

A limiting-current-type hydrocarbon sensor is developed to measure propane over a wide range propane concentration in a rich (no oxygen) environment. A low cost mass produced amperometric $\mathrm{O_2}$- $\mathrm{NO_x}$ sensor is used as the base sensor and then the operating conditions are modified to measure propane concentration. All of the main electrochemical inputs of the sensor have been modified to improve the sensor performance for measuring propane at different concentrations. The three electrochemical sensor cells in this case are: HC sensing, reference and stabilizing. The effect of sensor temperature (controlled by a closed loop heater), the reference cell potential, and the stabilizing cell potential on sensor performance are first studied to improve the transient performance and stability of the sensor. The sensor inputs and outputs are shown schematically in Fig. 6.13. Next, the sensor steady state behavior is experimentally investigated to find the diffusion-rate-determined operating region. Finally, the sensor transient response is studied for step changes in propane concentration.

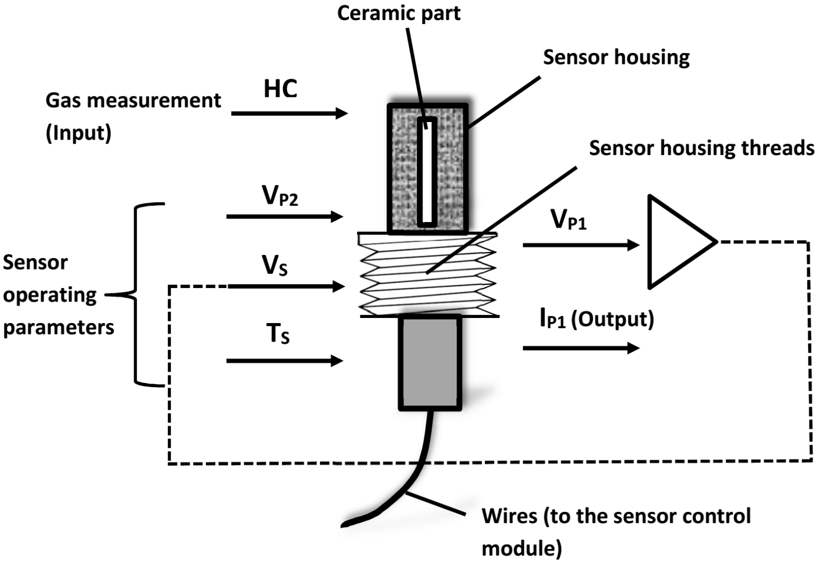

Figure 6.13: Amperometric HC Sensor operating parameters and input-output schematic

6.2.1 Amperometric sensor for HC measurement

A conventional NO_x sensor has been used as the base sensor and modified to measure propane at different concentrations. The sensor, shown schematically in Fig. 6.14, consists of three electrochemical cells: the HC sensing cell, the reference cell and the stabilizing cell. The sensor inputs are set to develop the capability of a limiting-current type amperometric HC sensor. In the limiting-current operating region, HC oxidizes in the first chamber and produces a cell current proportional to HC concentration. Higher resolution and easier calibration of this sensor are the main advantages in comparison with the other amperometric HC sensors [177, 178, 184].

The HC sensing cell is a variable-potential electrochemical cell. An internal controller adjusts the HC sensing cell potential (V_{P1}) to keep the reference cell potential (V_S) at a constant value. V_S corresponds to the potential difference between the

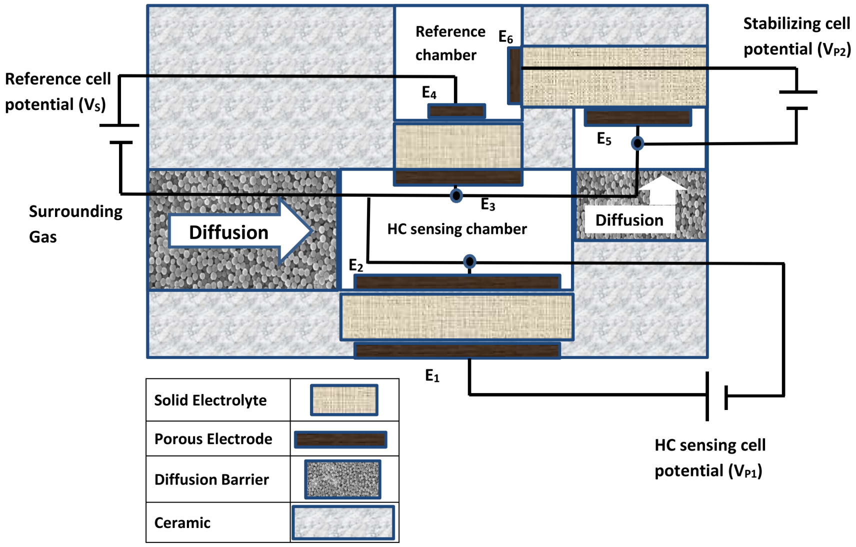

Figure 6.14: HC Sensor Schematic

HC sensing cell electrode (E3) and the reference cell electrode (E4). When the HC concentration in the surrounding gas increases and therefore diffuses into the first chamber, then the HC sensing cell voltage decreases to oxidize all the HC inside the first chamber to keep the reference cell potential at a constant value. It will be experimentally shown here that a positive fixed value of the stabilizing cell potential, increases the sensor stability at high hydrocarbon concentrations. The best value of the reference cell potential and the stabilizing cell potential have been determined experimentally as explained in the next section.

6.2.2 Experimental setup

The sensor test rig explained in section 5.4.2 was used to test the sensor at different propane concentrations.

6.2.3 Determining HC measurement parameters (HMPs)

The sensor temperature, T_S, the reference potential, V_S and the stabilizing cell potential, V_{P2}, are the main inputs that affect the sensor performance by influencing the diffusion of HC (propane) through the sensor as well as the oxidation rate of HC over the sensing electrode. The main objective of this optimization process is to investigate the effect of these factors on sensitivity and stability of the sensor.

To achieve high resolution and accuracy it is desirable that the sensor operate in Diffusion Rate Determining (DRD) conditions. To keep the sensor at the DRD condition, the diffusion rate of the measuring species through the sensor diffusion barrier should be lower than the reaction rate of the species on the sensing electrode. The sensor inputs (shown in Fig. 6.13) are modified to extend the working range of the sensor by expanding the DRD operating region.

The reaction rate of species over the sensing electrode is a function of electrode material, sensor temperature and the cell potential [95, 161]. The diffusion rate directly varies with the sensor temperature, the concentration of species in the surrounding gas and the concentration of species inside the sensor chambers [54, 95] according to the equations explained in section 6.2.4.2.

The diffusion rate increases with increasing the hydrocarbon concentration in the surrounding gas. If the hydrocarbon concentration goes higher than a certain large value, the diffusion rate becomes higher than the reaction rate and the sensor does not operate at DRD. Then, not all the HC can be oxidized inside the sensing cell since the HC oxidation rate is not as high as the diffusion rate of HC into the sensing chamber. The sensor behavior becomes unstable above this value due to the unbalanced diffusion-reaction rate and accumulation of the HC in the sensing cell.

The sensor is exposed to a high value (here, 5000 ppm) propane mixture balanced with nitrogen. This concentration is too high for the sensor to operate at diffusion limiting condition. Instead, the sensor has rate-determining operation. Then, the sensor inputs are changed to maximize the time duration of stable operation of the sensor. These specified sensor inputs are then used to study the sensor behavior at a DRD operating condition.

6.2.3.1 The effect of reference cell potential

The reference cell potential represents a set point for species concentration in the sensing chamber. For instance, in a wide-band oxygen sensor, the reference cell potential represents the oxygen concentration for stoichiometric combustion (zero oxygen concentration and zero unburned hydrocarbon concentration). For the amperometric HC sensor studied here, the reference cell (V_S) potential remains constant during sensor operation using a feedback controller by adjusting the HC sensing cell potential (V_{P1}). Once the reference potential is set, a closed loop controller adjusts the sensing cell potential and current to maintain the partial pressure of the oxidized species at the reference value.

The effect of reference cell potential on the sensor transient behavior is experimentally tested and the results are shown in Fig. 6.15 and Fig. 6.16. The sensor is first exposed to pure nitrogen (initial condition) and then to 5000 ppm propane diluted with nitrogen. The 5000 ppm propane is high enough to put the sensor in reaction rate determining operation. Then first objective is to maximize the duration of stable sensor current output before it starts dropping due to accumulation of non-oxidized HCs inside the first chamber and consequently dropping HC sensing cell voltage. Maximizing the stable-output duration at such a high concentration, ensures stable behavior at lower concentrations and therefore, increases the sensor DRD operating range.

Stable-output duration is experimentally found to increase with the reference cell potential. The corresponding sensing cell potential generally increases with the reference potential as shown in Fig. 6.16 and therefore postpones V_{P1} drop and postpones sensor unstable behavior. However, increasing the reference cell potential to 0.82 V has an opposite effect on the output stability. This is attributed to electrode decomposition that takes place at high cell potentials [127].

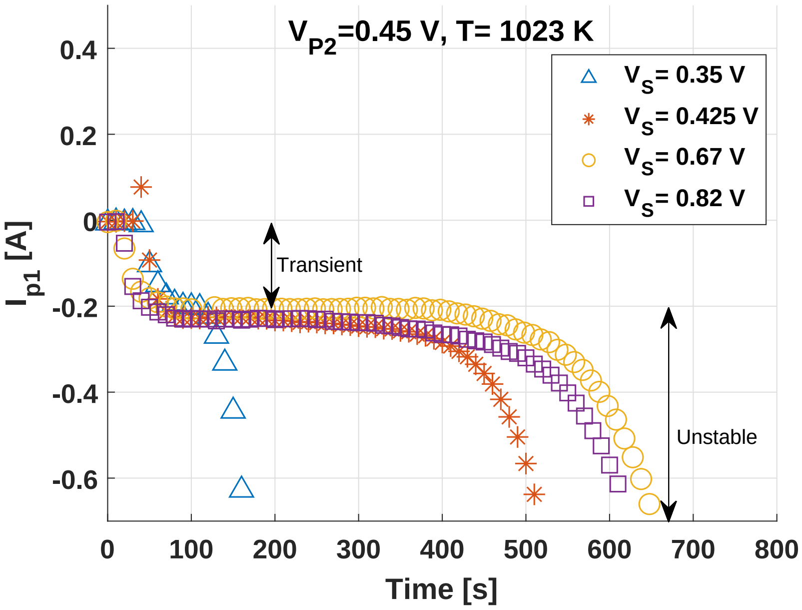

Figure 6.15: The effect of reference cell potential on the transient behavior of the sensor output current at HC (propane) concentration = 5000 ppm

6.2.3.2 The effect of Temperature

The sensor temperature has a more complicated effect on the sensor behavior as it affects both the diffusion of species through the sensor diffusion barriers (explained in section 6.2.4.2) and the reaction rate over the electrode as follows [51]:

$$V_{P1} = \underbrace{E^o + \frac{\Delta S_{ox-red}}{nF}(T_s - T_o) - \frac{\bar{R}T}{nF} ln\left(\frac{\prod_{i=1}^{k_1}(x_{i,anode})^{y_{1i}}}{\prod_{j=1}^{k_2}(x_{j,cathode})^{y_{2j}}}\right)}_{E_N} - \eta_a \tag{6.18}$$

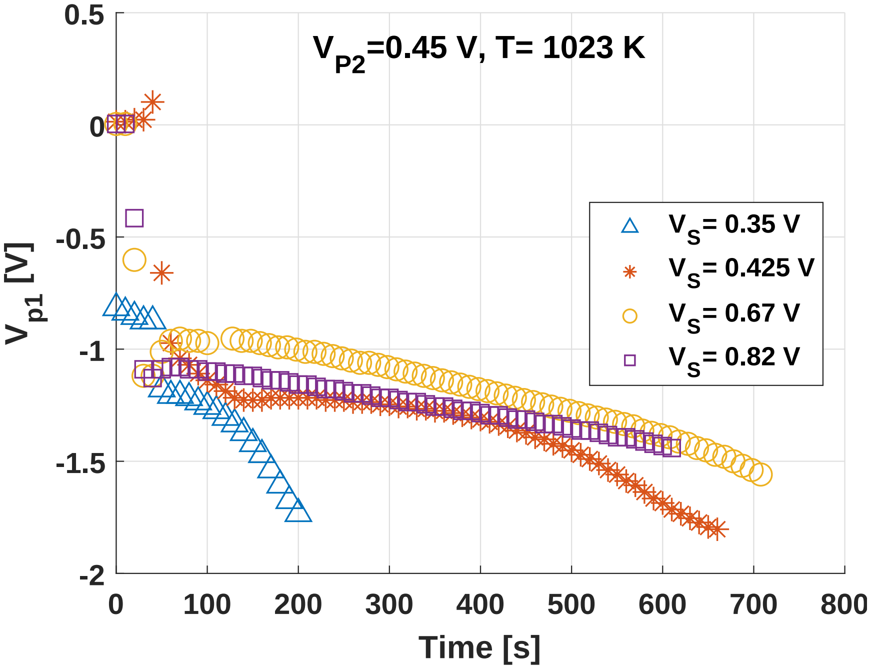

Figure 6.16: The effect of reference cell potential on the transient behavior of the sensing cell potential at HC (propane) concentration = 5000 ppm

where, $\bar{R}$ is the universal gas constant, F is the Faraday constant, T_s is the sensor temperature (in Kelvin), T_o is the reference temperature, ΔS_{ox-red} is the change in entropy of products-reactants at the operating temperature and E^o is the open-circuit potential at the standard state (1 atm; 298.15 K) while $x_{i,anode}$ and $x_{j,cathode}$ are the molar fraction of species around the anode and the cathode respectively. The parameters y_{1i} and y_{2j} and n depend on the species involved in the electrochemical reaction [51].

Therefore, the effect of temperature on the sensor output stability may vary for different operating conditions. The effect of sensor temperature on sensor transient behavior at three different reference potentials is shown in Fig. 6.17 and 6.18. The reaction rate and the diffusion rate both increase with the sensor temperature [50, 127]. This two-sided effect can either reduce or increase the stable-output duration, depending on the operating condition.

According to the experimental results, at $V_S = 0.45$ V, the stable-output duration decreases dramatically when the sensor temperature increases from $T_S = 1023$ K to 1080 K while at $V_S = 0.82$ V, the stable-output duration increases as the temperature increases. For 1009 K $\leq T_S \leq$ 1080 K and 0.35 V $\leq V_S \leq$ 0.82 V, the most stable sensor performance is experimentally found at T_S= 1009 K and $V_S = 0.672$ V. Stabilizing is defined as the time it takes for I_{P2} to drop to 10% lower than its stable response value for a step input of propane.

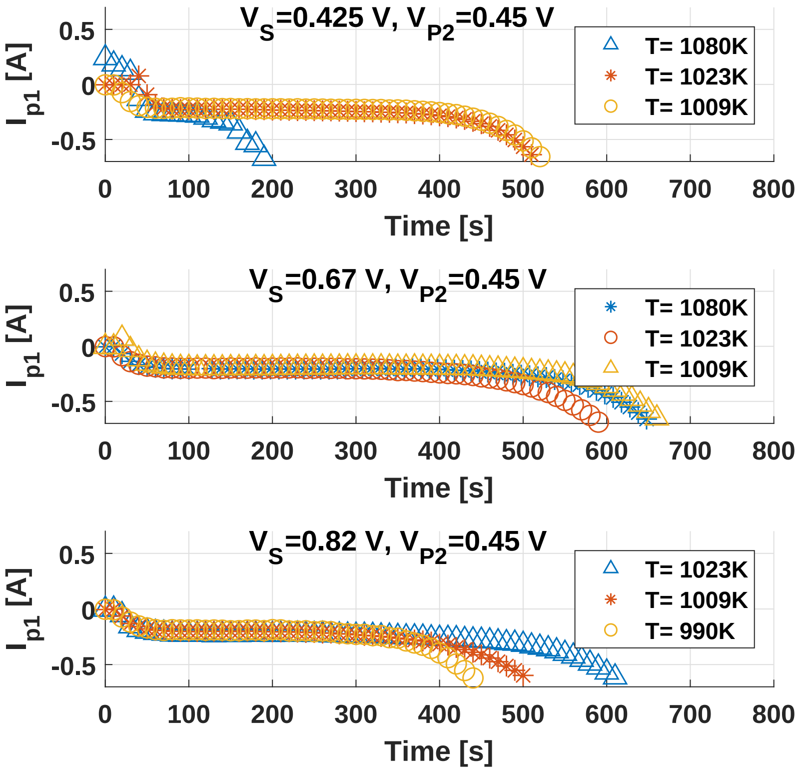

Figure 6.17: The effect of temperature on the transient behavior of the sensor output current at HC (propane) concentration = 5000 ppm

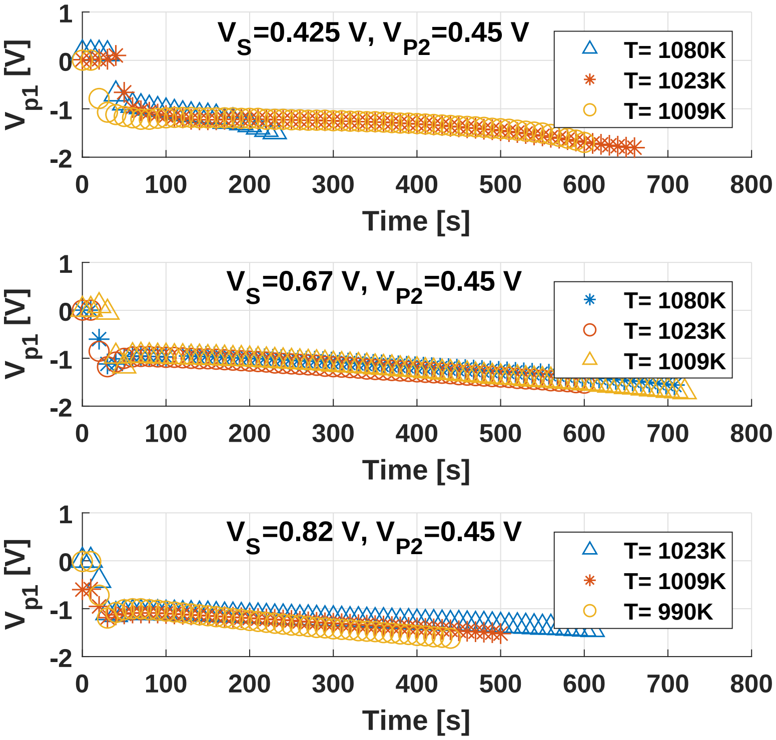

Figure 6.18: The effect of temperature on the transient behavior of the sensing cell potential at HC (propane) concentration = 5000 ppm

6.2.3.3 The effect of stabilizing cell potential

Compared to the HC sensing cell, the stabilizing cell has a Platinum (Pt) electrode which has a lower activation energy for reducing species inside the stabilizing cell chamber. This significantly affects the gradient of species concentration through all of the sensor chambers and barriers [50] and changes the sensor output. To find the best value of the stabilizing cell potential (V_{P2}), the transient behavior is examined at two different cell potentials, V_{P2} = 0.22 V and V_{P2} = 0.45 V. The sensor is tested at two stabilizing cell potentials of 0.22 V and 0.45 V and the results are shown in Fig. 6.19 and 6.20. The potential V_{P2} = 0.45 V is used as it is typically high enough to reduce any combustion engine productions, such as NO_x, that get into the stabilizing chamber [50].

At HC = 5000 ppm in the surrounding gas, the stable-output duration is experimentally found to increase as the stabilizing cell potential increases. The stabilizing cell potential is set to $V_{P2} \leq 0.45$ V to avoid electrolyte decomposition.

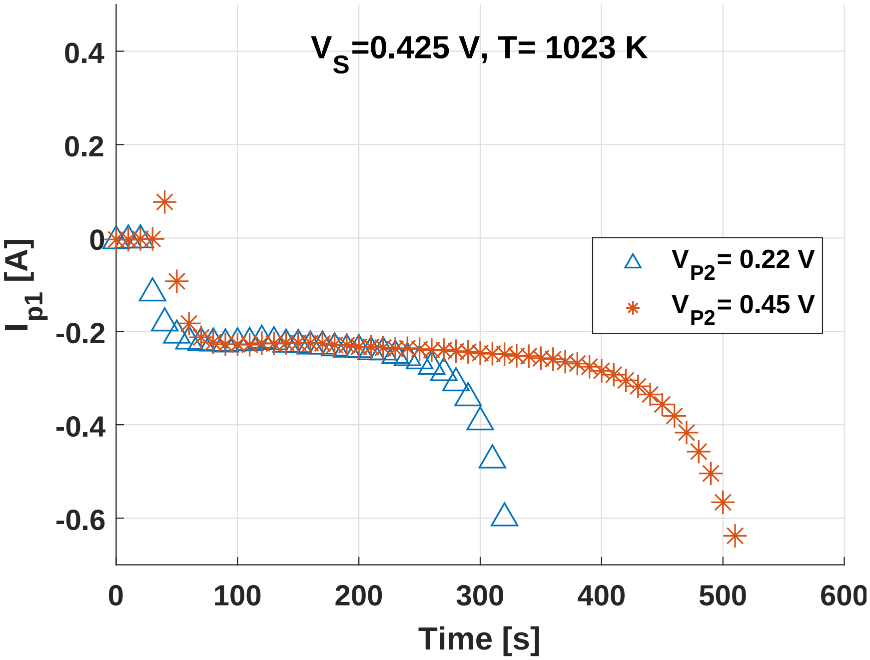

Figure 6.19: The effect of second sensing cell potential on the transient behavior of the sensor output current at HC (propane) concentration = 5000 ppm

6.2.3.4 The effect of CO_2 presence

All the above tests were carried out in the absence of any oxygen containing species as the propane mixture was diluted with pure nitrogen. To study the sensor transient behavior in the presence of an oxygen containing specie, CO_2 is used. The choice of CO_2 is based on that it is a hydrocarbon combustion product. Now, the sensor is exposed to the same propane concentration (4350 ppm) without and with CO_2, while CO_2 concentration = 13 % setting $V_S = 0.35$ V, $V_{P2} = 0.45$ V and the sensor temperature equal to 1080 K. For both of the tests, the sensor is initially exposed to

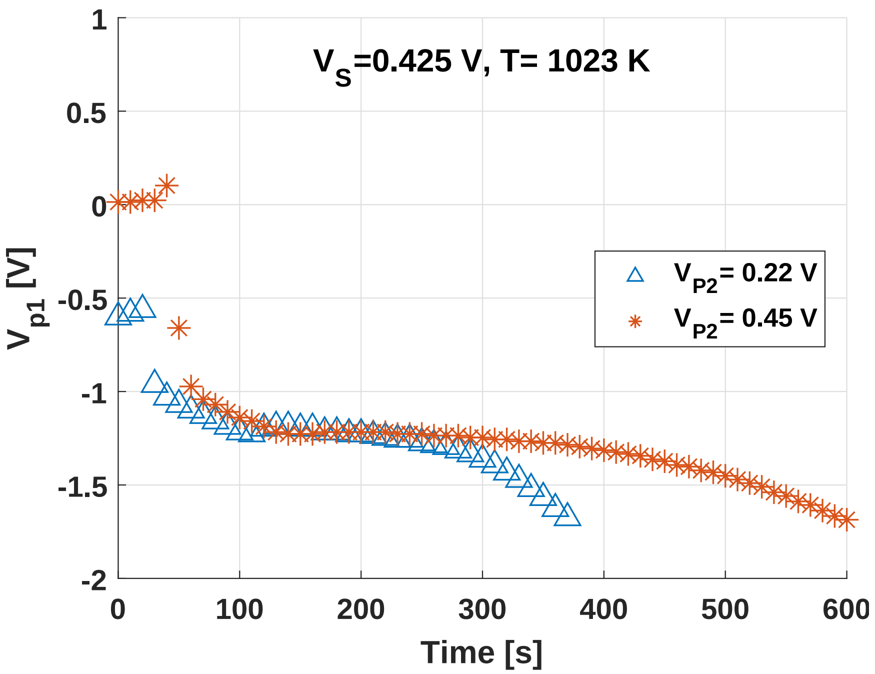

Figure 6.20: The effect of second sensing cell potential on the transient behavior of the sensing cell potential at HC (propane) concentration = 5000 ppm

the N_2-CO_2 mixture with no propane and then to 4350 ppm propane concentration. The transient results are shown in Fig. 6.21. The presence of CO_2 does not have a significant effect on the sensor transient behavior as shown in Fig. 6.21 and does not have an effect on the steady state sensor behavior.

6.2.4 Steady state sensor behavior

6.2.4.1 The effect of propane concentration

After maximizing the stable-output duration, the sensor sensitivity to propane (diluted with N_2) is evaluated at the HMPs ($V_S = 0.67$ V, $V_{p2} = 0.45$ V, T=1009 K). The sensor stable response at different propane concentrations has been studied to find the sensor sensitivity to propane and to find the DRD operating region. The test results at five different propane concentrations are shown in Fig. 6.22. The steady state sensor output magnitude, decreases with the propane concentration. This is due to

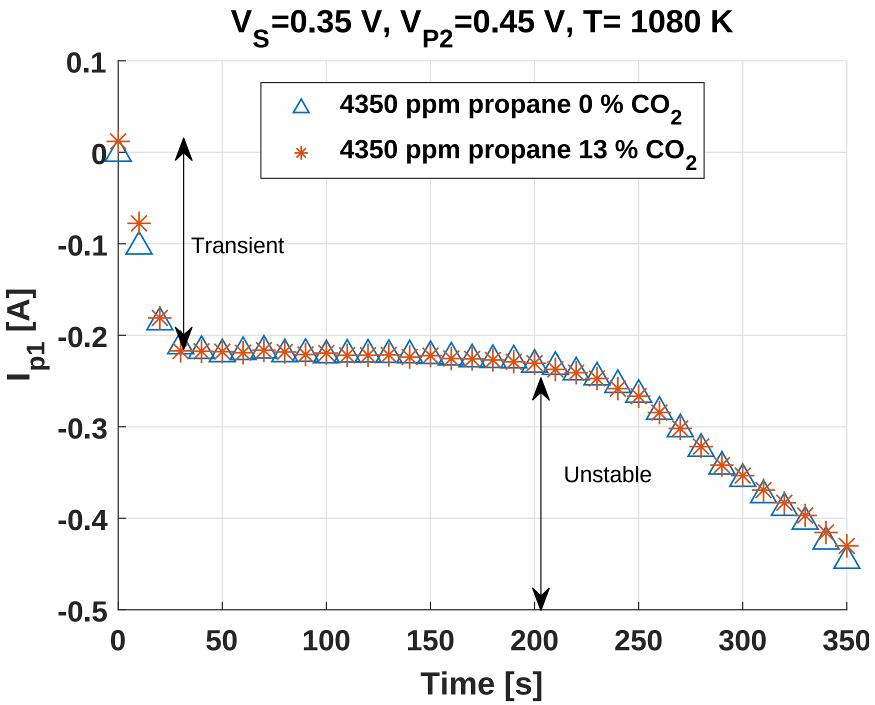

Figure 6.21: The effect of presence of CO_2 on the transient behavior of the sensing cell current

the lower diffusion rate of propane through the sensor diffusion barrier and therefore the lower oxidation rate of propane over the sensing electrode. This sensitivity of the sensor output to propane can be used to measure propane concentration. However, to develop an accurate and reliable sensor, the DRD operating region should first be determined. This procedure is explained next.

6.2.4.2 Diffusion rate-determining (DRD) operating region

The HC sensing cell pumping current is proportional to the molar flux of propane through the sensor diffusion barrier. According to Faraday's law [110]:

$$I_p \propto N_{C_3H_8} \tag{6.19}$$

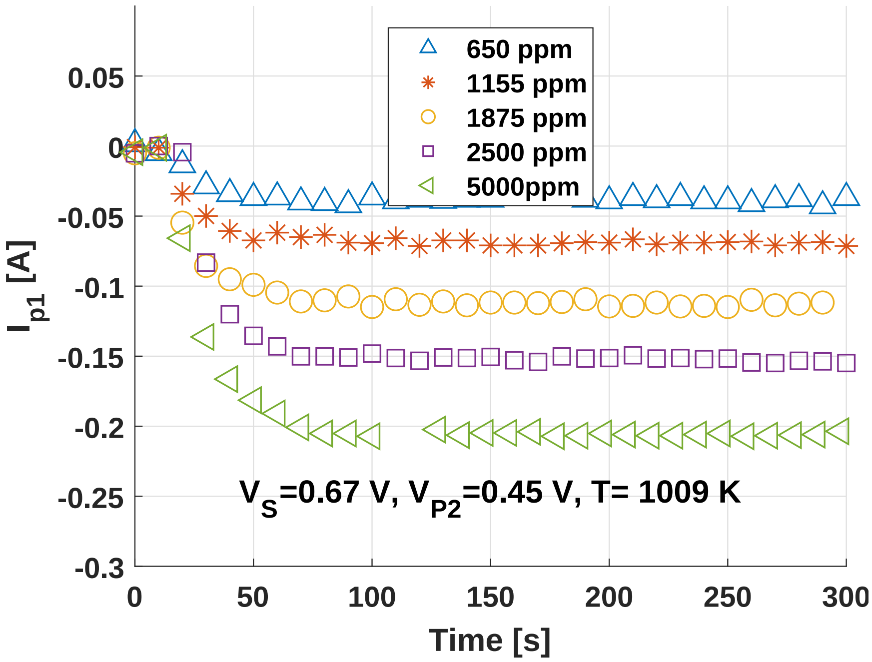

Figure 6.22: The effect of propane concentration on the transient behavior of sensor output current at propane concentration = 5000 ppm

where, $N_{C_3H_8}$ is the molar flux of propane through the first diffusion barrier to the HC sensing chamber.

Assuming negligible convection inside the cell and perfect dilution of propane in N_2, the molar flux of propane ($N_{C_3H_8}$) can be estimated using Fick's law [150]:

$$N_{C_3H_8} = -C_t D_{C_3H_8} A_{D1} \frac{x_{C_3H_8,sur} - x_{C_3H_8,senc}}{L_{D1}} \tag{6.20}$$

Where, $N_{C_3H_8}$, C_t, $x_{C_3H_8,sur}$ and $x_{C_3H_8,sur}$ are the molar flux, total concentration and the mole fraction of propane in the surrounding gas and inside the sensing chamber respectively while A_{D1} is the diffusion barrier cross sectional area, L_{D1} is the diffusion barrier length and $D_{C_3H_8}$ is the diffusion coefficient of propane through the porous diffusion.

For DRD operating condition, propane oxidizes with a higher rate than it diffuses into the sensing chamber. In this case, the molar fraction of propane decreases to a very low value ($x_{C_3H_8,senc} \approx 0$). Therefore, based on Eqn. (6.19) and (6.20), the sensor current output becomes linearly dependant on propane concentration in the surrounding gas.

In order to define the DRD operating region and the corresponding sensor linear operation band, the sensor output current vs propane concentration is shown in Fig. 6.23. The sensor output current magnitude increases linearly with propane concentration up to approximately 3200 ppm propane concentration as shown in Fig. 6.23. The sensor output current then plateaus at propane concentrations higher than 3200 ppm. The sensor is working as DRD for propane concentration below 3200 ppm and for higher propane concentration, the sensor operates at reaction rate determining condition.

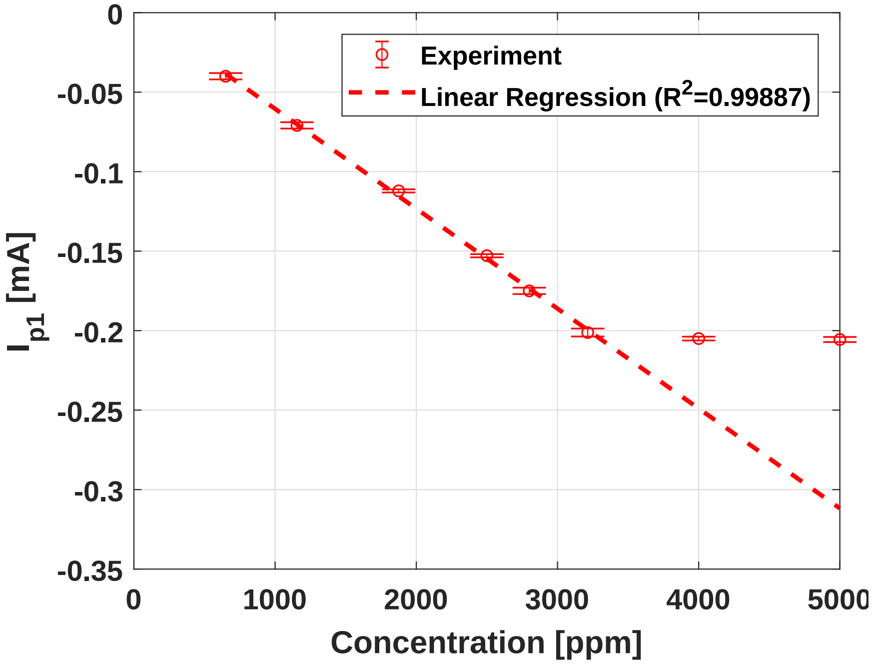

Figure 6.23: The sensor output current vs propane concentration. V_S= 0.67 V, T= 1009 K, V_{P2}= 0.45 V

6.2.5 Sensor response time

Sensor response time is used to capture the transient behavior of a system. A better understanding of the sensor transient behavior is useful to determine appropriate applications for the sensor.

A normalized variable is defined by dividing the transient sensing cell current by the steady state cell current at the same propane concentration ($I_{P1,diff}$). The transient behavior of the normalized sensing cell current is shown in Fig. 6.24. The results show that the size of the propane step concentration does not have a significant effect on the transient behavior with the response time as shown in Fig. 6.24.

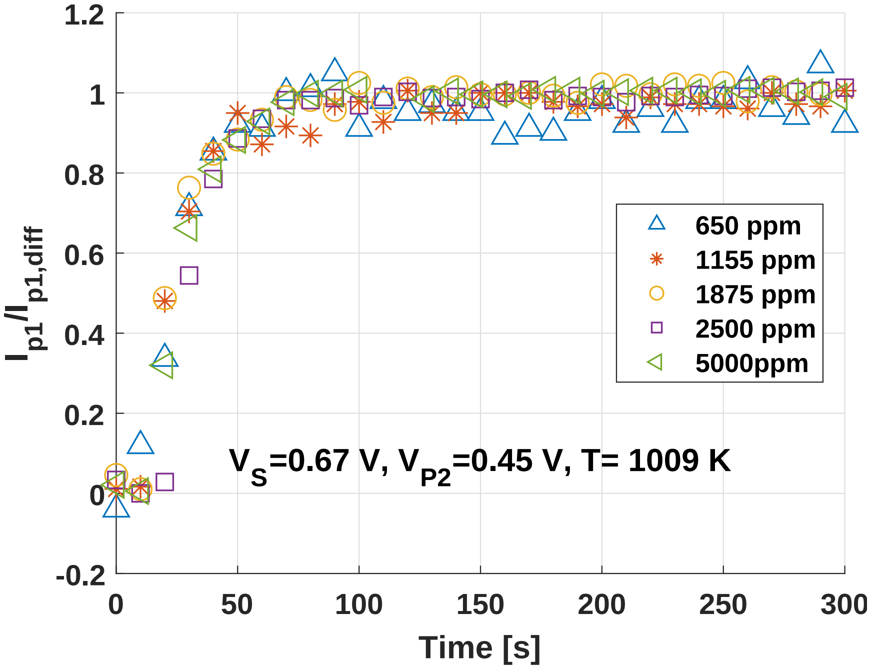

Figure 6.24: Transient behavior of the normalized sensor current at different propane concentrations

The step-response characteristics of the sensor is studied considering all of the normalized sensor outputs and the sensor response time (10% to 90%) was found to be 38 seconds. Although this response time is shorter than many other amperometric HC sensors [177, 178], it could be significantly reduced by modifying the sensing cell potential (V_{P1}) controller since the long sensing cell potential settling time, shown in Figures 6.16, 6.18 and 6.20, increases the sensor response time.

6.2.6 Summary of HC measurement

A production three-chamber limiting-current-type amperometric sensor is modified to measure propane concentration in a rich environment. First, the sensor stability is maximized for purpose of measurement by changing the sensor inputs including the sensor temperature, the reference cell potential, and the stabilizing cell potential. Stability is defined as the time it takes for I_{P2} to drop to 10% lower than its stable response value. Then stability tests are carried out on a controlled sensor test rig at a reaction rate determining operating condition with propane concentration of 5000 ppm (balanced with nitrogen). Based on the experiments, the sensor has a stability of 530 seconds at sensor temperature of 1009 K, a reference cell potential of 0.67 V and a stabilizing cell potential of 0.45 V. This condition is then fixed for subsequent sensor operating condition. Further experimental testing shows that the presence of CO_2 does not have a significant effect on the sensor sensitivity to propane and the sensor transient behavior.

To find the diffusion-rate-determined operating region, the linearity of sensor steady state response vs propane concentration is experimentally studied at the stable operating condition. A linear sensitivity to propane concentration from 0 to 3200 ppm reveals the DRD operating region of the sensor.

To study the sensor transient behavior in DRD operating region, the sensor response time is examined for step changes from zero propane concentration to several propane concentrations. It is shown that the sensor response time is almost the same for different size step changes of propane concentration and is approximately 38 seconds. This response speed could be improved by modifying the sensing cell controller and will be a subject of future work.

6.3 The effect of operating parameters of an amperometric NO_x-O_2 sensor on the sensor response - A potential way to remove cross-sensitivity and emission measurement [3]

Experimental results are combined with a physical understanding of the sensor to study the effect on the sensor behavior of three main operating parameters of an amperometric NO_x-O_2 sensor. The sensor response to NO_x concentration is examined over a range of: sensor operating temperatures, the reference cell potential, and the cell potential in the second chamber. The results show that the sensor sensitivity increases gradually with the sensing cell voltage while the sensor gradually increases for cell voltages higher than 0.25 V. The results of this work provides a better understanding of the sensor behavior at different operating conditions which can be used to design new accurate sensors with different sensitivities to a variety of species in the exhaust gas. This improved understanding of the sensor has the potential to remove cross-sensitivity for emission measurements of gases containing NOx and other species in the exhaust gas such as NH_3 and unburned hydrocarbons.

The effect of main operating conditions of an amperometric NO_x-O_2 sensor on sensor sensitivity to NO_x and the linearity of the sensor response to NO_x concentration is studied. The results of this study, provide insight into which operating range of an amperometric NO_x-O_2 sensor can be used to reduce or remove the sensor cross-sensitivity to other exhaust gas species.

6.3.1 The role of electrochemical cell potential

A typical cell current vs cell voltage response of an amperometric sensor is shown in Figure 5.4. When the cell voltage is lower than the open-circuit (zero-current) potential, the reverse reaction (oxidation) takes place causing a negative cell current.

---

[3] This section is based on the paper titled: *The effect of operating parameters of an amperometric NOx -O2 sensor on the sensor response*[53]

When the cell voltage is above the open-circuit potential and less than the limiting current voltage, the sensor output is a function of reduction rate of species on the sensing electrode. This reduction rate is defined by the activation polarization and the Ohmic effect. As the cell voltage increases further, the cell current finally reaches a saturation level determined by the diffusion rate of reducible species (in this case, O_2 and NO_x) into the chamber (region V of Figure 5.4). In region V the pumping rate of (O^{2-}) ions from the cell has reached its maximum level since all available reducible molecules are being reduced on the sensing electrode as soon as they reach the electrode surface.

A further increase in the cell voltage, decreases the partial pressure of the reduced species (in this case, NO) according to the Nernst equation [95]. If the partial pressure of the reduced species (NO) decreases too much, ($< 10^{-33}$ atm), electrolyte decomposition takes place [127] which causes a further increase in the cell current as illustrated in region VI of Figure 5.4. This can potentially damage the sensor electrolyte. The sensor electrochemical cells and internal wiring are shown in Figure 4.1 and described in details in [50].

6.3.2 The role of sensor temperature

At typical operation of an amperometric sensor, the sensing cell potential is high enough so that the pumping current is equal to the limiting current determined by diffusion of species through the barriers (region II). Therefore, for a typical sensor cell potential, an increase in the sensor temperature will affect the sensor output, by affecting the diffusive flow of species into the sensing chambers [54]. The normal multicomponent diffusion mechanism is found to be the dominant diffusion mechanism of species through the amperometric NO_x sensor diffusion barriers [50]. According to the molecular diffusion mechanism, the diffusion coefficient, D_n, increases with the sensor temperature as [54]:

$$D_n \propto T^{1.75} \tag{6.21}$$

Assuming that the sensor output current is limited by the diffusion rate, the sensor output, I_P, changes with temperature as [54]:

$$I_P \propto T^{0.75} \tag{6.22}$$

However, when diffusion is not the only rate determining factor for reduction of species over the sensor electrodes, the sensor temperature will affect the sensor output current in a more complex way as [51]:

$$I_P = A_e i_P^o \left(\frac{x}{x^o}\right)^{\gamma} \left[exp\left(\frac{\alpha_a F}{\bar{R}T}\eta_{ac}\right) - exp\left(\frac{-\alpha_c F}{\bar{R}T}\eta_{ac}\right)\right] \tag{6.23}$$

where, A_e, i_P^o, x and x^o are the sensing electrode area, the reference exchange current density, the mole fraction of reduced species inside the chamber and the reference mole fraction of the reduced species in the sensing chamber respectively, while α_a and α_c are the charge transfer coefficient of anode and cathode respectively. The overpotential η_{ac} is defined as $\eta_{ac} = V_P - E_{OC}$, where V_P and E_{OC} are the potential and the open circuit (zero-current) potential of the sensing cell.

The O_2 sensing cell potential, V_{P1}, affects the mole fraction of NO inside the first chamber, $x_{NO,fc}$, as [51]:

$$V_{P1} = \underbrace{E_{fc}^o + \frac{\Delta S_{ox-red,fc}}{2F}(T - T_o) - \frac{\bar{R}T}{2F} ln\left(\frac{x_{NO,env}}{x_{NO,fc}}\right)}_{E_N} - \eta_a \tag{6.24}$$

where, ΔS_{ox-red} is the change in entropy of $products - reactants$ at the operating temperature (the index sc stands for the second chamber) and E_{fc}^o is the open-circuit potential at the standard state (1 atm; 298.15 K) while $x_{NO,env}$ and $x_{NO,fc}$ are the molar fraction of NO in the sample gas and in the first chamber respectively.

On the other hand, the NO_x sensing cell potential, V_{P2}, affects the mole fraction of NO inside the second chamber, $x_{NO,sc}$, as follows [51]:

$$V_{P2} = \underbrace{E^o_{sc} + \frac{\Delta S_{ox-red,sc}}{2F}(T - T_o) - \frac{\bar{R}T}{2F} ln(\frac{x^{0.5}_{O_2,rc} x^{0.5}_{N_2,rc}}{x_{NO,sc}})}_{E_N} - \eta_\Omega - \eta_{ac} \tag{6.25}$$

where, $x_{O_2,rc}$, $x_{N_2,rc}$ and $x_{NO,sc}$ are the mole fraction of O_2 in the reference chamber, the mole fraction of N_2 in the reference chamber, and the mole fraction of NO in the second chamber respectively.

6.3.3 Experimental setup

The gas mixture test rig, Spark Ignition (SI), Diesel engine, amperometric NO_x-O_2sensor and the FTIR system described in chapter 3 were used to carry out the experiments.

6.3.4 Results and discussion

To investigate the effect of sensor temperature on sensor sensitivity and the sensor linearity to NO_x, the sensor response is measured at three sensor temperatures and four diesel engine operating conditions. The NO_x concentrations are listed in Table 6.4 as well as the concentration of other species in the exhaust gas measured by the FTIR emission measurement system. The results for H_2O, CO_2 and CO from the FTIR are also listed in Table 6.4. The sensor temperatures selected for this study are close to the typical design sensor operating temperature (1023 K) and are controlled by a built in heater located between the sensor ceramic layers. Decreasing the sensor temperature to lower than the sensor design temperature, reduces the diffusion coefficient of NO through the sensor diffusion barriers according to Eqn. (6.21). The typical sensing cell potential ($VP_1 \approx 0.4$ V) is high enough so that NO is partly reduced in the first chamber [51]. Thus reducing the sensor temperature reduces the reduction rate of NO inside the first chamber according to Eqn. (6.24) which increases the molar fraction of NO inside the first chamber causing an increase in the molar flow rate of NO, according to Fick's law [150], to the second chamber.

Table 6.4: Engine operating conditions and NO_x concentration in the exhaust gas. * Water condensation inside the sample lines may have affected the concentration of water measured by the FTIR.** The stoichimetric air/fuel ratio is changed to change the level of NO_x emission in the SI engine

Engine	Eng. speed [rpm]	BMEP [bar]	NO_x[ppm]	CO_2 [%]	H_2O^* [%]	CO [ppm]
SI**	2000	6.7	470 - 1750	-	-	-
Diesel	2500	1.1	103	2.82	3.12	2.82
Diesel	2000	3.8	175	4.00	3.21	154
Diesel	1500	7.6	368	6.50	3.24	177

Increasing the sensor temperature increases the diffusion rate of NO through the sensor barriers and reduction rate of NO in the first chamber. At a sensor temperature of 1080 K, the effect of temperature increase on NO reduction in the first chamber outweighs its effect on the diffusion rate. As a result, less NO is delivered to the NO_x sensing chamber which consequently reduces the pumping current of NO in the NO_x sensing chamber as shown in Figure 6.25 and Table 6.5. The linearity of sensor response is also reduced at the high sensor temperature (1080 K) as depicted in Table 6.5. When sensor linearity is assumed, this adversely affects the sensor accuracy particularly at high NO_x concentrations.

Table 6.5: Linearity of I_{P2} vs NO_x as a function of sensor temperature - from Figure 6.25

Case	Sensor temperature [K]	R^2	Slope [$\mu A/ppm$]
1	1010	0.9998	0.002531
2	1023	0.9999	0.002493
3	1080	0.98751	0.001918

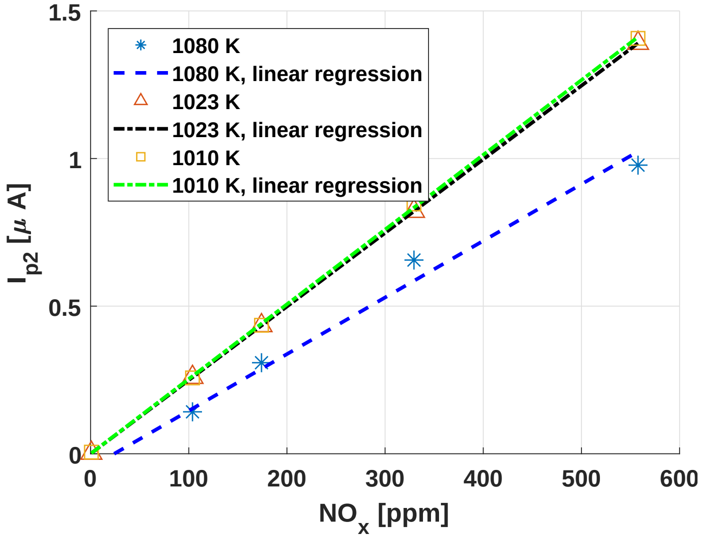

Figure 6.25: The effect of sensor temperature on sensor output I_{P2} as a function of NO_x by examining the sensor sensitivity (slope) and linearity

6.3.4.1 The effect of reference cell potential

The reference cell potential, V_S, represents the partial pressure (and therefore molar fraction) of O_2 inside the O_2 sensing chamber. A closed loop controller maintains the reference cell potential at the set point value by adjusting the potential of the O_2 sensing cell, V_{P1}. The mole fraction of O_2 inside the O_2 sensing chamber decreases by increasing the reference cell potential, according to Eqn. (6.23). Therefore, by reducing the set point value of the reference cell potential, the O_2 concentration increases in the first chamber. Four values of V_S are selected as listed in Table 6.6. This can lead to an offset in the pumping current of the NO_x sensing chamber, particularly at low NO_x concentrations as shown in Figure 6.26. Apart from the effect of reference cell potential on the NO_x sensor response, it also affects the sensor cross-sensitivity to O_2. The presence of O_2 in the sample gas has a more significant effect on the sensor response slope at $V_S = 0.42$ V than $V_S = 0.35$ V as shown in Figure 6.26 and Table 6.6, which reveals that the NO_x sensor response has a higher cross-sensitivity to O_2 at $V_S = 0.42$ V. This effect is mainly due to the difference between the corresponding O_2 sensing cell potential, V_{p1}, as illustrated in Figure 6.27 with the cases described in Table 6.6.

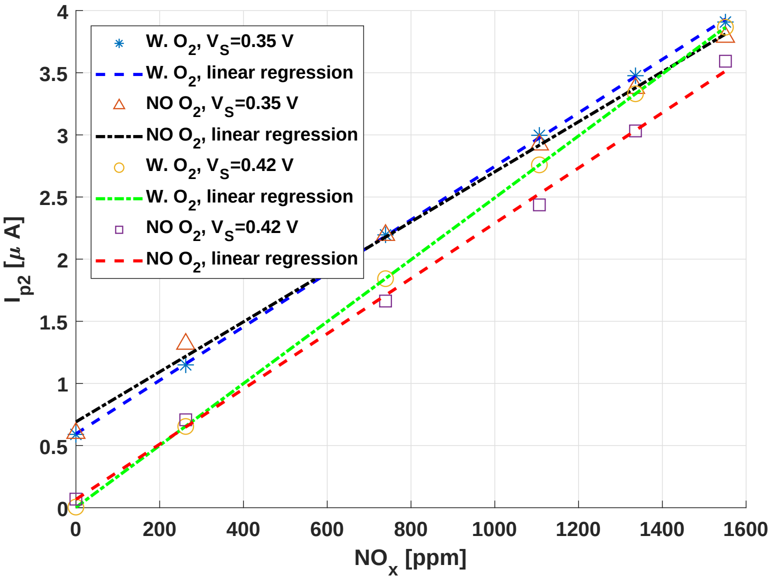

Figure 6.26: The effect of reference potential (V_S) resulting in the presence of O_2 on sensor output I_{P2} as a function of NO_x by examining the sensor sensitivity (slope) and sensor linearity. Cases are explained in Table 6.6.

Table 6.6: Reference cell voltage and linear fit characteristics of the cases shown in Figure 6.26.

Case	Reference cell potential [V]	Presence of O_2?	R^2	Slope [$\mu A/ppm$]
I	0.35	YES	0.99986	0.002152
II	0.35	NO	0.99752	0.002012
III	0.42	YES	0.99999	0.002491
IV	0.42	NO	0.99786	0.002223

6.3.4.2 The effect of second (NO_x sensing) cell potential

The most important factor that affects an amperometric NO_x sensor performance is the potential of the NO_x sensing cell, V_{P2} [51]. To better understand the effect of NO_x sensing cell potential on the sensor sensitivity to NO_x, the slope of the sensor output vs NO_x concentration is calculated at different cell potentials and the

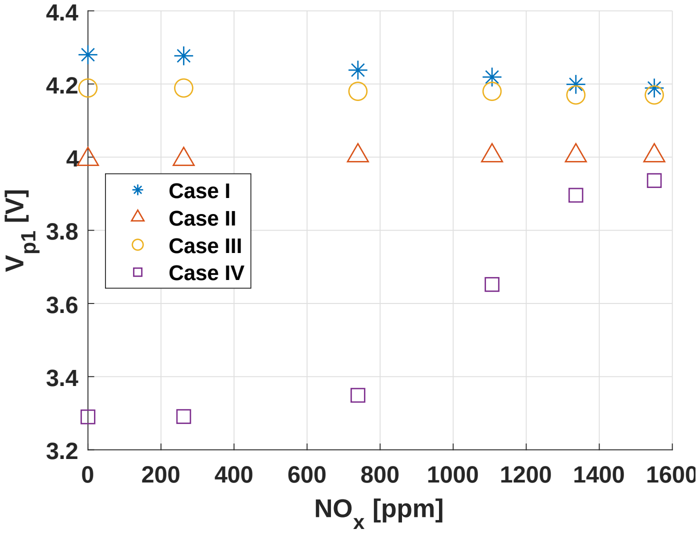

Figure 6.27: The effect of reference potential and presence of O_2 on the O_2 sensing chamber. Cases are explained in Table 6.6.

experimental results are shown in Figure 6.28 along with the corresponding linear regression plot at each NO_x sensing cell potential. The details of each case indicated in Figure 6.28 are listed in Table 6.7.

Table 6.7: NO_x sensing cell potential and linear fit characteristics of the cases shown in Figure 6.28.

Case	NO_x sensing cell potential [V]	R^2	Slope [$\mu A/ppm$]
1	0.138	0.0467	-2.453e-5
2	0.170	0.7268	1.481e-4
3	0.189	0.9218	2.204e-4
4	0.199	0.9773	2.411e-4
5	0.250	0.9946	5.981e-4
6	0.343	0.9986	1.008e-3
7	0.447	0.9999	1.198e-3

The sensitivity of the sensor output to NO_x generally increases with the NO_x sensing cell voltage (V_{P2}) since the reduction rate of NO increases with increasing the NO_x sensing cell potential, according to Eqn. (6.25). Therefore, the mole fraction of NO inside the NO_x sensing chamber decreases according to Eqn. (6.25) which causes an increase in the pumping current. The linearity of the sensor output vs

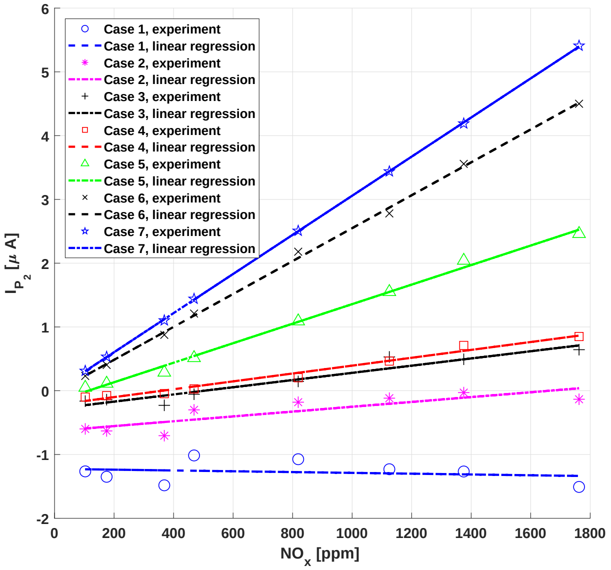

Figure 6.28: I_{p2} vs NO_x concentration at different NO_x sensing cell voltages - from V_{P_2}= 0.138 V to V_{P_2}= 0.447 V (see Table 6.7)

NO_x concentration also increases with the cell voltage. This trend is also shown in Figure 6.29. The most interesting point that can be concluded from the results shown in Figure 6.29, is the different effect of the NO_x sensing cell potential on the sensor response linearity (linear regression R^2) and the sensor sensitivity to NO_x concentration (linear regression slope). The sensor sensitivity increases gradually with the cell potential while the linearity of the sensor dramatically increases at sensor potential ≈ 0.25 V and remains higher than 0.995 for $V_{P2} > 0.25$ V . In other words, although the sensor sensitivity to NO_x gradually increases with the cell potential for cell potentials higher than 0.25 V, the sensor output is almost linear at any points within this range. This behavior can be used to design accurate sensors with different sensitivities to other species such as NH_3 and unburned hydrocarbons as it provides an insight into the sensor sensitivity and operating range. The sensor operating parameters can significantly affect the sensor sensitivity to a specie, as shown in this work. The best sensor performance is achieved when the sensor sensitivity to a de-

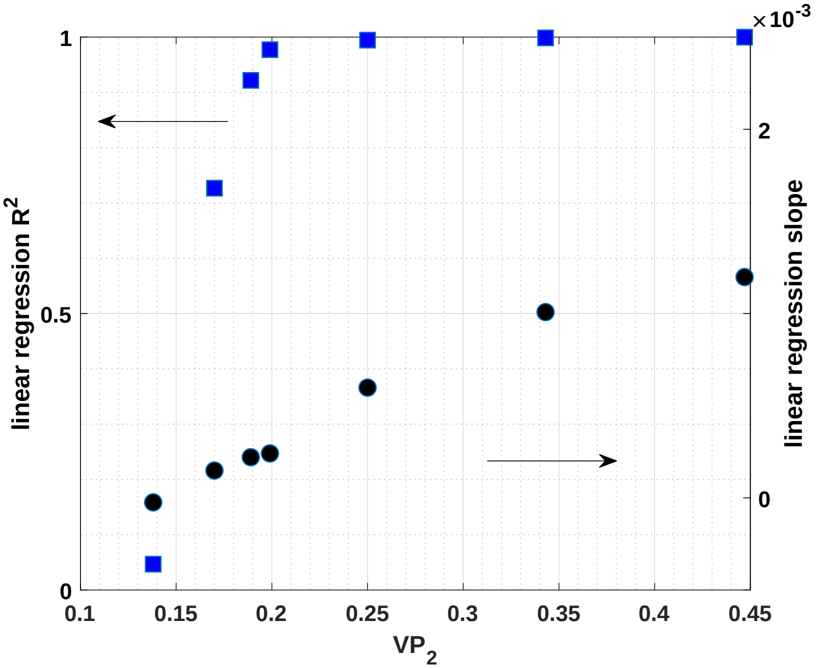

Figure 6.29: The effect of NO_x sensing cell voltage on sensitivity and linearity of the NO_x sensor

sired specie is sufficient and the sensor response vs concentration of desired specie is linear. Simultaneously, the sensor cross sensitivity to the other species should be minimized or at least be predictable. The results of this work provide an insight into the operating region of an amperometric NO_x sensor with sufficient sensitivity and linearity to NO_x.

6.3.5 Summary of the effect of sensor operating parameters

The effect of sensor operating temperatures, the reference cell potential and the NO_x sensing cell potential on an amperometric NO_x-O_2 sensor response linearity and the sensor sensitivity to NO_x were experimentally examined. The effect of these three main operating parameters of the sensor were understood based on a phenomenological model. The experimental results show that:

- The sensor sensitivity to NO_x decreases by increasing the sensor temperature by increasing the reduction rate of NO_x inside the O_2 sensing chamber. Increasing the sensor temperature to more than the sensor design temperature (1023 K), reduces the sensor response linearity to NO_x concentration.

- Reducing the reference cell potential from the typical cell potential (0.42 V) increases the NO_x sensor response offset at low NO_x concentrations but also reduces the sensor cross-sensitivity to O_2 particularly at high NO_x concentrations (>600 [ppm]).
- The sensor sensitivity gradually increases as the NO_x sensing cell potential increases while the sensor output becomes almost linearly dependent on NO_x concentration for cell potentials higher than ≈ 0.25 V.

This improved understanding of the sensor has the potential to remove cross-sensitivity for emission measurements of gases containing NO_x and other species in the exhaust gas such as unburned hydrocarbons and NH_3 by providing an insight into the sensor sensitivity and operating range.

CHAPTER 7

SENSOR ON-BOARD DIAGNOSTICS (OBD)

This chapter presents a physics-based On-Board Diagnostics strategy based on a sensor temperature perturbation method. This strategy also includes a sensor self-calibration procedure that can be used to remove the effect of sensor aging on sensor calibration. The other part of this chapter includes details of a Multiple Input Multiple Output (MIMO) control oriented engine model developed to estimate $\mathrm{NO_x}$ *concentration and engine normalized torque. The model can be used in engine closed-loop control.*

7.1 Motivation

According to the emission regulations [29, 30], any fault in any emission-relevant device must be detected and reported through on-board diagnostics (OBD) [31]. The first OBD standard was passed as a law in 1970 by US congress to reduce the adverse effect of vehicular emissions on environment [32]. In 1996, an updated standard (OBD II) was introduced. OBD II standard mandates monitoring of any electronic powertrain system or component that provides input to, or receives commands from the electronic control unit (ECU) [31].

Exhaust gas sensors are used upstream and/or downstream of after-treatment systems to monitor their efficiency and performance [32, 40, 41]. To meet increasingly stringent emission standards, the accuracy of the emission sensors also needs to be increased [42–46]. This requires reliable on-board diagnostics of emission sensors in addition to the other aftertreatment components. Reliable physics-based diagnostics strategies which require understanding of the sensor performance are needed.

7.2 $\mathrm{NO_x}$ sensor OBD using a phenomenological sensor model [1]

A phenomenological sensor model is developed and then employed to detect the potential faults that can occur to an amperometric $\mathrm{NO_x}$ sensor. As discussed in the previous sections, the diffusion of exhaust gas species through the sensor diffusion barriers and the electrode reactions inside the sensor chambers are the main processes that affect the sensor outputs [108, 109]. As explained in chapter 4, at the sensor operating condition, the diffusion of species through the barriers into the sensor chambers is the rate determining step since the diffusive flow is much slower than the sensor reaction dynamics [110]. As shown in chapter 4, the diffusion of species through the sensor barriers and the electrode reactions of species both depend on the sensor temperature [50, 185]. The dominant diffusion mechanism of the diffusive flow inside the sensor is multi component molecular diffusion [50].

In this section a physics-based model was developed and employed to predict the sensor output to oxygen as a function of sensor temperature and oxygen concentration which is used for sensor OBD and re-calibration. The sensor output is predicted with normal diffusion taken to be the dominant diffusion mechanism through the sensor barriers. Then a two step sensor diagnostics strategy is proposed to evaluate sensor output validity and plausibility by varying the sensor temperature. The model results match the experiments in transient and steady state conditions. Finally, a self-calibration method is developed based on temperature perturbation and an external

---

[1] This section is partly based on the following paper: M. Aliramezani, C.R. Koch, and R. Patrick. Phenomenological model of a solid electrolyte NOx and O2 sensor using temperature perturbation for on-board diagnostics. Solid State Ionics, 321:62 68, 2018 [54]

relative humidity measurement.

7.2.1 Sensor output as a function of temperature and O$_2$ concentration

Combining Eqn. (5.9) and Eqn. (4.4), using ideal gas law and assuming all oxygen is immediately pumped out from the first chamber ($x_{O_2}|_{1st\ chamber} \approx 0$), results in: $I_{p1} \propto T^{0.75}$ and $I_{p1} \propto x_{O_2}$. Where, x_{O_2} is mole fraction of O$_2$ in the surrounding gas. Therefore:

$$I_{p1}(T, x_{O_2}) = \overbrace{k \times T^{0.75}}^{K} \times x_{O_2} \tag{7.1}$$

in which, k is a constant and K is the slope of the linear function of I_{P1} versus x_{O_2}. At a constant O$_2$ concentration ($x_{O_2,0}$, reference concentration), if the sensor temperature changes from T_1 to T_2, the current ratio $\frac{I_{p1}(T_2)}{I_{p1}(T_1)}$ is:

$$\frac{I_{p1}(T_2, x_{O_2,0})}{I_{p1}(T_1, x_{O_2,0})} = \frac{k \times T_2^{0.75} \times x_{O_2,0}}{k \times T_1^{0.75} \times x_{O_2,0}} = \left(\frac{T_2}{T_1}\right)^{0.75}$$

The change in pumping current, I_{P1} between condition two (at T_2) and condition one (at T_1) is:

$$\begin{aligned} \Delta I_{P1}|_{x_{O_2,0}} = I_{p1}(T_2, x_{O_2,0}) - I_{p1}(T_1, x_{O_2,0}) &= k \times T_2^{0.75} \times x_{O_2,0} - k \times T_1^{0.75} \times x_{O_2,0} \\ &= k \times x_{O_2,0} \times T_1^{0.75} \times [(\frac{T_2}{T1})^{0.75} - 1)] \end{aligned}$$

with

$$k = \frac{\Delta I P_1|_{x_{O_2,0}}}{x_{O_2,0} T_1^{0.75}[(\frac{T_2}{T_1})^{0.75} - 1]}$$

and

$$K = \frac{\Delta IP_1|_{x_{O_2,0}}}{x_{O_2,0}T_1^{0.75}[(\frac{T_2}{T_1})^{0.75} - 1]} \times T^{0.75} \tag{7.2}$$

where, $x_{O_2,0}$ is the reference O_2 concentration and $\Delta IP_1|_{x_{O_2,0}}$ is the change in pumping current due to temperature at a given oxygen concentration.

In normal operation, the sensor temperature is kept constant using a temperature controller that measures sensor temperature by measuring ohmic resistance of the reference Nernst cell [50]. This, according to Eqn. (7.1), results in I_{P1} being linearly dependant to changes in x_{O_2}. The slope of the linear I_{P1} function vs x_{O_2} (K) is calibrated by the sensor manufacturer. To do this, external measurements of O_2 via a reference measurement system for at least two O_2 concentrations are needed. This relation varies from sensor to sensor due to manufacturing tolerances and sensor aging. Alternatively, the slope K can be calculated using the temperature perturbation method using only one O_2 concentration. This is schematically shown in Figure 7.1. Since only one O_2 concentration is needed and the temperature can be changed using the sensor heater electronics, the sensor can be recalibrated any time there is a known oxygen concentration - For example at *engine-off* condition (ambient oxygen concentration). This recalibration can be used to remove the effect of mass production variation between different sensors or sensor aging when necessary. In addition, the methodology will be used to develop a sensor diagnostics strategy.

7.2.2 Experiments

The experiments were carried out using a production ECM NO_x sensor (P/N: 06-05) and the corresponding control module (described in chapter 3) connected to a computer via *Kvaser Light HS* CAN interface. The sensor was located in the exhaust pipe (0.30 m upstream of the diesel oxidation catalyst) of a 4 cylinder medium duty

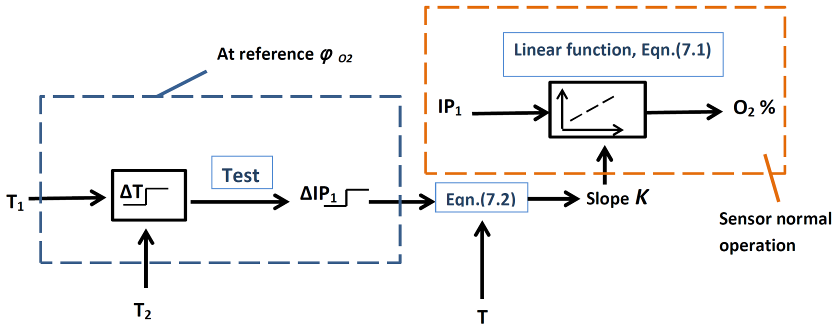

Figure 7.1: I_{P1} vs O_2 linear function calibration using temperature perturbation

diesel engine (Cummins QSB 4.5 160 - Tier 3). All the tests were carried out at *engine-off* (known O_2 concentration).

The sensor control module controls the sensor temperature by controlling the heater power mounted inside the sensor. The impedance of the reference Nernst cell (R_{pvs}) varies with sensor temperature and this was used to measure and control the sensor temperature. A heat transfer model developed in [50] was used to define sensor temperature as a function of R_{pvs} as:

$$T = c_1 (R_{pvs})^{c_2} \tag{7.3}$$

where for this sensor $c_1 = 1396$, $c_2 = -0.0559$ are determined using a *nonlinear least squares* fit [186] with a squared correlation coefficient of R^2=0.991.

To calculate sensor temperature from R_{pvs} during the steady state and transient tests, Eqn. (7.3) was used. The sensor temperature calculated by a heat transfer model [50] is compared to the correlation in Eqn. (7.3) versus R_{pvs}, shown in Figure 7.2(a), with the residuals shown in Figure 7.2(b).

A temperature perturbation test around the sensor normal operation temperature was performed to evaluate the model accuracy for the rising and falling temperature

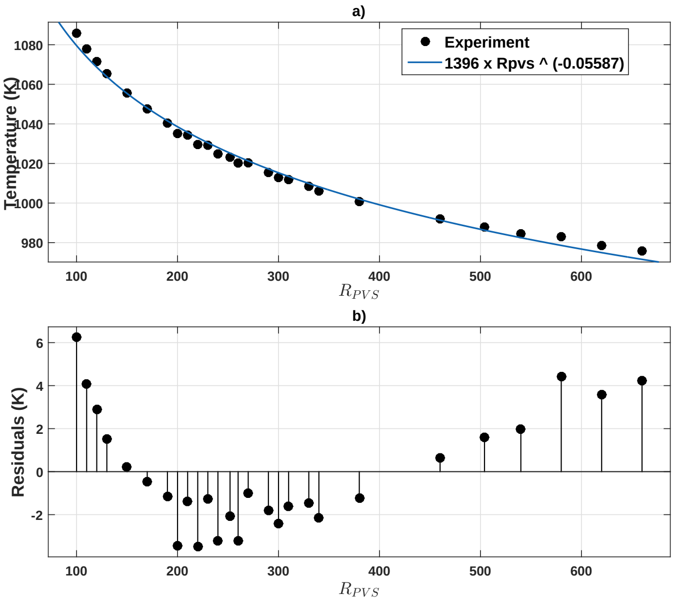

Figure 7.2: a) Sensor temperature from heat transfer model [50] (symbols) and Eqn. (7.3) correlation (line) versus Nernst Cell impedence R_{PVS} b) Temperature error as a function of R_{PVS}

steps. The test was carried out at *engine-off* with the standard $T = 1023$ K as the reference sensor temperature. The sensor output at all other sensor temperatures were defined based on the reference output at T=1023K using Eqn. (7.1). The transient and steady state results of the perturbation test are shown in Figure 7.3 which shows a comparison of desired temperature versus the sensor temperature calculated from Eqn. (7.3). In addition, a comparison of model current I_{p1}, Eqn. (7.1), versus experiment for step changes in set point temperature is also shown in Figure 7.3.

The model is capable of accurately simulating the effect of temperature perturbation on the sensor output in steady state and transient condition as shown in Figure 7.3. The overshoot and undershoot in sensor output shown in Figure 7.3 are caused by the overshoot and undershoot of sensor temperature control as shown in Figure 7.3. The maximum overshoot and undershoot in sensor output were 12.8 % and 8.8 % respectively with the maximum *2% settling time* of 14.6 s. It should be

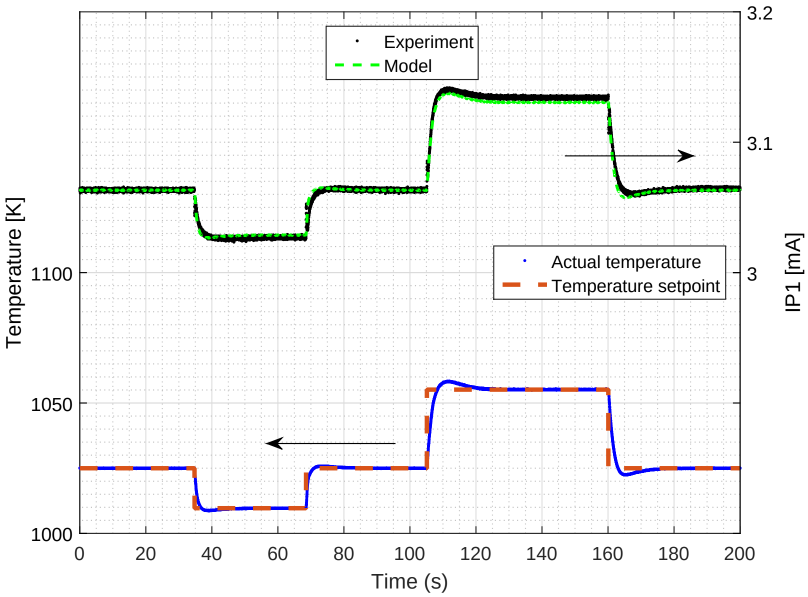

Figure 7.3: Transient sensor behavior during sensor temperature perturbation test

noted that the temperature controller is designed for regulating the temperature at T=1023 K and is not tuned for steps in sensor temperature, so the overshoot is not unexpected.

For T_1= 1010 K and $x_{O_2,0}$= 20.7 %, $\Delta IP_1|_{x_{O_2,0}} = +0.105$ (mA) for $\Delta T = +45$K and therefore the parameter K in Eqn. (7.2) is 0.1543. This point was then used as the reference point to evaluate the effect sensor reference temperature and temperature step size on ΔIP_1. This is shown in Figure 7.4 where increasing reference sensor temperature (T_1) decreases ΔI_{P1} for a fixed ΔT. In other words, the slope of ΔI_{P1} vs. ΔT decreases as the sensor temperature increases. Steady state experiment results are the constant values in Figure 7.3.

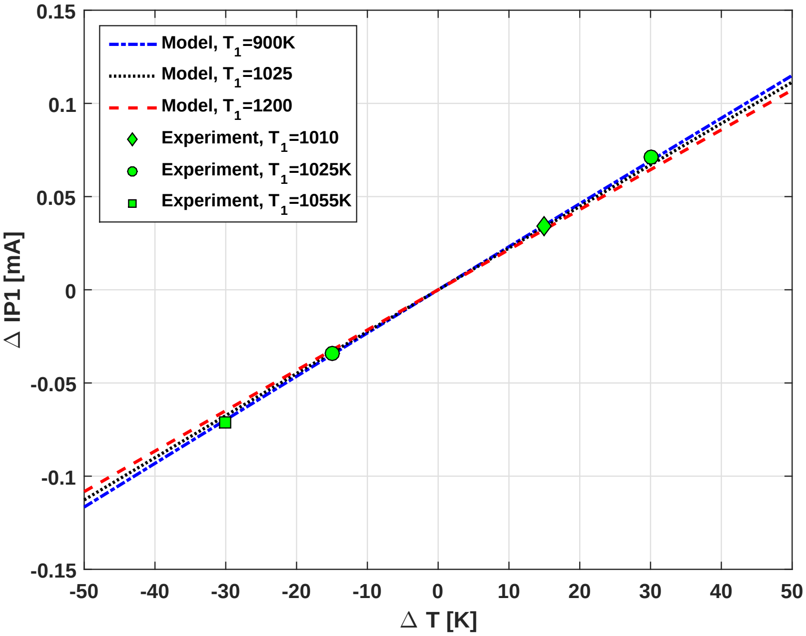

Figure 7.4: The effect of temperature step size and reference temperature (T_1) on ΔIP_1. Experimental results are from Figure 7.3 (steady state).

7.2.3 Sensor diagnostics and self-calibration

First, to check for a valid sensor output, the *engine-off* condition was taken as the reference point[2]. A valid sensor output must be within a certain range defined by oxygen mole fraction in the environment. The O_2 mole fraction in the environment is a function of relative humidity in air [188]. Assuming the atmospheric air as an ideal-gas mixture with total pressure (p_a) which is the sum of the partial pressure of dry air ($p_{a,dry}$) and the partial pressure of water vapor (p_v) [188]:

$$p_a = p_{a,dry} + p_v \tag{7.4}$$

This shows the partial pressure of species in humid air is less than dry air due to the

---

[2] Engine fuel cut-off condition that takes place during long downhill gradients [187], can also be used as the reference point.

partial pressure of water vapor. Therefore, O_2 mole fraction in air is [189]:

$$x_{O_2}(\%) = x_{O_2,dry}(\%) - c_h(T) \times RH \tag{7.5}$$

where, $x_{O_2,dry}$ is O_2 mole fraction in dry air ($\approx$ 20.9%) and is a weak function of environment temperature [188]. The relative humidity is RH and $c_h(T)$ is the temperature correction factor that increases with temperature [189]. It should be noted that the atmospheric pressure (altitude) also affects the absolute partial pressure of O_2 in the atmospheric air. However, the O_2 mole fraction in air is not affected by the atmospheric pressure. Considering the worst case scenario to be 100% relative humidity at 60°C and 101 kPa, the minimum possible value of O_2 % is 16.8 % according to [188]. The maximum possible O_2 % is for dry air and is considered to be 20.9 % [188]. Thus, the acceptable range for O_2 sensor output is defined based on the maximum and minimum valid values. If the sensor output is out of this range, a diagnostic can be generated to indicate the sensor is not working properly and needs to be recalibrated or perhaps even replaced. This is a binary plausibility diagnostic: "*working properly*" | "*problem*".

A more complex diagnostic is to evaluate the sensor performance. Eqn. (7.1) is used to estimate ΔI_{P1} for a given ΔT ($\Delta IP_{1(model)}$). The sensor accuracy and plausibility are evaluated by comparing the $\Delta IP_{1(model)}$ and $\Delta IP_{1(test)}$. The test error, e_t, is:

$$e_t = \Delta IP_{1(test)} - \Delta IP_{1(model)} \tag{7.6}$$

This is schematically shown in Figure 7.5.

Now, a variety of diagnostic tests including a model based methods can be used [190–194] but these are not the subject of this chapter. A high value of e_t means

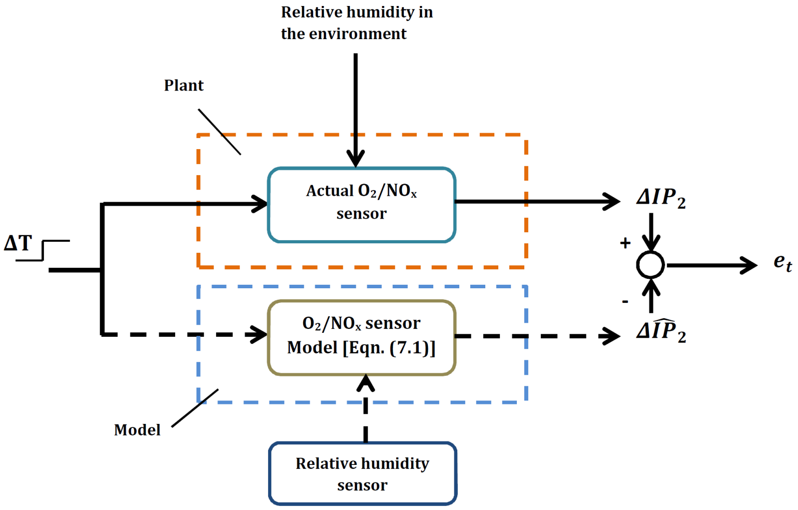

Figure 7.5: Error calculation for temperature perturbation test

either the sensor diffusion barrier is damaged or the sensor temperature controller is not working properly. For instance, according to Eqn. (7.1), for $x_{O_2,dry}$= 20.7 % and T_0=976 K, a 100°C deviation between the actual ΔT and the required ΔT, causes a 0.29 mA increase in e_t and 2 % error in oxygen measurement assuming the sensor barrier is working properly. A damaged diffusion barrier can cause much more deviation than this by effecting the diffusion mechanism inside the sensor. Choosing a maximum allowable error in O_2 measurement of 0.2 %, the maximum value of 0.03 mA was considered for for e_t (et_{MAX} = 0.03 mA).

The effect of sensor aging also increases e_t and this error can be nulled by recalibrating the sensor. External measurement of relative humidity in the environment can be used to recalibrate the sensor according to Eqn. (7.5). The proposed sensor diagnostics and recalibration strategy are shown in Figure 7.6.

The first step of the sensor diagnostics is the plausibility check where the sensor output is evaluated by checking whether it is within a valid range. In the second step, the temperature perturbation test is done to calculate the error, e_t, between the expected $\Delta IP1$ from the model and the actual $\Delta IP1$ from the test result. A simple

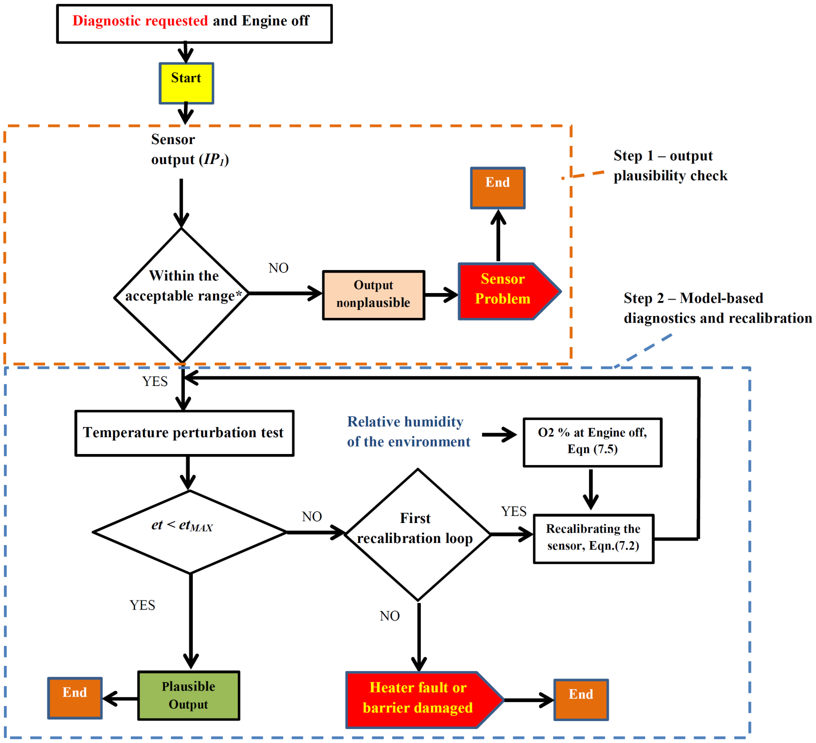

Figure 7.6: Sensor diagnosis schematic (*Engine off condition*)
* Acceptable output range for x_{O_2} is between 16.8 % and 20.9 %

diagnostic is to see if e_t is more than $e_{t\ MAX}$. If it is, a recalibration loop takes place to check if the error can be removed by sensor recalibration. Measuring relative humidity by an external measurement system, increases the reliability of sensor calibration. If the test error is higher than the limit after the first recalibration loop, then either the sensor temperature controller that includes the heater does not work properly or the sensor diffusion barrier is damaged (diagnosed) on an unknown error.

The diagnostics strategy that has been developed, monitors the first diffusion barrier and O_2 sensing cell of a NO_x sensor as well as the performance of sensor temperature controller. This procedure makes O_2 sensor output and NO_x sensor output more reliable as both O_2 and NO_x species pass through the first diffusion barrier. However, any failure in electrochemical performance of NO_x sensing cell is not monitored with this diagnostics strategy and therefore it does not provide an absolute confirmation for NO_x output validity. This diagnostics is a necessary but not sufficient requirement for proper NO_x sensor operation. If the sensor does not pass diagnostic results, neither O_2 nor NO_x output are reliable and the sensor must be replaced. Diagnostics of the electrochemical system of the NO_x sensing cell will be studied in future.

Table 7.1: Interpretation of the diagnostics test result

Diagnostics result	Is O_2 output reliable?	Is NO_x output reliable?
Not passed	NO	NO
Passed	YES	More likely/ Not certainly

7.2.4 Summary of the phenomenological model implementation for OBD

An on-board diagnostics strategy was developed using a physics-based model of an amperometric NO_x-O_2 sensor. The model predicts the sensor O_2 output as a function of sensor temperature and oxygen concentration based on multi component molecular diffusion mechanism of exhaust gas species through the sensor. A temperature perturbation method was proposed and used to calibrate the sensor output with respect to oxygen concentration. To evaluate the accuracy of the model in steady state and transients, temperature perturbation tests for both rising and falling sensor temperature steps are performed experimentally and the model results closely match the experiments.

A two step sensor diagnostics strategy was then proposed to evaluate the sensor output based on the sensor output validity range and a model-based diagnostics strategy that includes a temperature perturbation test. A self-calibration procedure was included in the diagnostics procedure which requires an external relative humidity measurement. The plausibility of the sensor output as well as the performance of sensor heater and diffusion barriers can be evaluated with the proposed physics-based diagnostics strategy.

7.3 A control oriented diesel engine $\mathrm{NO_x}$ emission model for on board diagnostics and engine control with sensor feedback [3]

Fast and accurate emission measurement facilitates improving engine performance and reducing engine emissions by providing real-time feedback for use in engine closed-loop control. Solid-state electrochemical gas sensors have many remarkable properties that make them ideal for real-time engine emission measurement [50]. The reliability, small size, fast response and low price of solid-state electrochemical sensors make them ideal for engine emission measurement [33, 90]. An electrochemical fast response $\mathrm{NO_x}$ sensor is used to measure $\mathrm{NO_x}$ concentration in the exhaust gas.

Based on experimental data, a Multi-Input Multi-Output (MIMO) control oriented diesel engine model is developed to predict engine $\mathrm{NO_x}$ emission and brake mean effective pressure (BMEP). The experimental tests were carried out on a 4.5L medium duty diesel engine at different engine operating conditions with engine speed between 1000 rpm to 2500 rpm and normalized engine output, BMEP, between 1.9 [bar] and 17.4 [bar]. The engine $\mathrm{NO_x}$ emission is measured with a fast response electrochemical $\mathrm{NO_x}$ sensor.

A steady state diesel engine $\mathrm{NO_x}$ emission and BMEP model is first developed based on the experimental data carried out on a medium duty diesel engine. The steady state engine $\mathrm{NO_x}$ is modeled as a function of the engine speed, the amount of injected fuel and the injection rail pressure. The BMEP is assumed to be a function of the injected fuel and engine speed. Then, a control oriented model is developed by adding low-pass filters to the static $\mathrm{NO_x}$ and BMEP models. The engine response to step changes of injection pressure and injected fuel amount is then examined.

---

[3] This section is based on the following paper: M. Aliramezani, A. Norouzi, C.R. Koch and R.E. Hayes. *A control oriented diesel engine NOx emission model for on board diagnostics and engine control with sensor feedback.* Proceedings of Combustion Institute - Canadian Section. Spring 2019 [55].

7.3.1 Experimental setup

To study the engine NO_x emission at different engine operating conditions, an electrochemical NO_x sensor was mounted in the exhaust pipe of a four cylinder medium duty Tier III diesel engine (Cummins QSB4.5 160 - Tier 3/Stage IIIA). The engine and sensor characteristics are listed in chapter 3.

The Cummins Engine Control Unit (ECU) controls the Diesel engine by reading all the stock sensors mounted on the production Cummins engine including the intake manifold temperature, intake manifold pressure, injection rail pressure, coolant temperature, and controlling all of the engine main actuators and operating parameters, including the injection timing(s), turbocharge boost pressure, injection amount, etc. To read the engine main variables and operating parameters, the ECU is connected to a computer using J1939 connector and a hardware interface (INLINE 6).

The NO_x sensor used in the experiments was a production ECM NO_x sensor (P/N: 06-05). The sensor output for NO_x was measured and logged using the corresponding control module (*ECM-NOxCANt* P/N: 02-07) connected to a computer via *Kvaser Light HS* CAN interface. More information about the experimental setup is available in chapter 3. The engine is tested at 14 steady state operating conditions listed in Table 7.2.

7.3.2 Control Oriented Model

The BMEP and engine-out NO_x emission are considered the main outputs of the control oriented model. The steady state experimental data is used to develop the steady state NO_x and BMEP model. For simplification, the dynamics NO_x and BMEP models are obtained by adding a first order low pass filter to the steady state models.

7.3.2.1 Steady state NO_x emission model

The NO_x emissions of a diesel engine are a strong function of the local in-cylinder temperature and local oxygen concentration [195, 196]. Based on the available experimental data of the engine operating parameters that have a direct effect on engine NO_x emission [197], the following polynomial equation is found for the steady-state engine NO_x emission the steady-state engine NO_x emission:

$$NO_{x,ss} = a_o + a_1 mf_i + a_2 mf_i^2 + a_3 mf_i^3 + a_4 P_r + a_5 P_r^2 + a_6 n + a_7 n^2 \tag{7.7}$$

where, $NO_{x,ss}$ is the steady state NO_x concentration [ppm], mf_i is the injected fuel [mg/stroke], P_r is the injection rail pressure [bar] and n is the engine speed [rpm]. Parameters a_o to a_8 are found through fitting to experimental data using a trust-region algorithm [165] with squared correlation coefficient (R^2) of 0.989. The experiments were carried out at 14 engine operating conditions (listed in Table 7.2) with the engine speed of 1000 to 2500 rpm and output torque of 50 to 450 ft.lb. The sensor cross-sensitivity to other exhaust gas species (including H_2O) is neglected in the model. Parameters a_o to a_8 are listed in Table 7.3. The predicted vs experimental NO_x concentration is shown in Fig. 7.7.

7.3.2.2 Steady state BMEP model

A simple model is also developed for the steady state BMEP. The BMEP is assumed to be a function of the injected fuel [mg/stroke] and the engine speed [rpm] [198], as follows:

$$BMEP_{ss} = b_o N^{b_1} mf_i^{b_2} \tag{7.8}$$

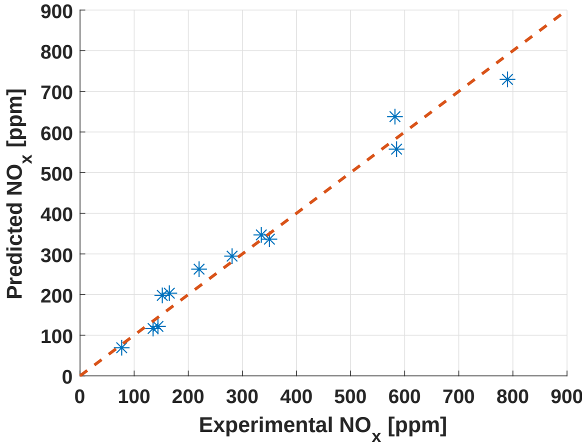

Figure 7.7: Predicted vs Experimental NO_x concentration at steady state

where, $BMEP_{ss}$ is the steady state BMEP. Parameters b_o to b_2 are found through fitting to experimental data using a trust-region algorithm with squared correlation coefficient (R^2) of 0.9914. The model parameters are listed in Table 7.4. The predicted vs experimental BMEP is shown in Fig. 7.8.

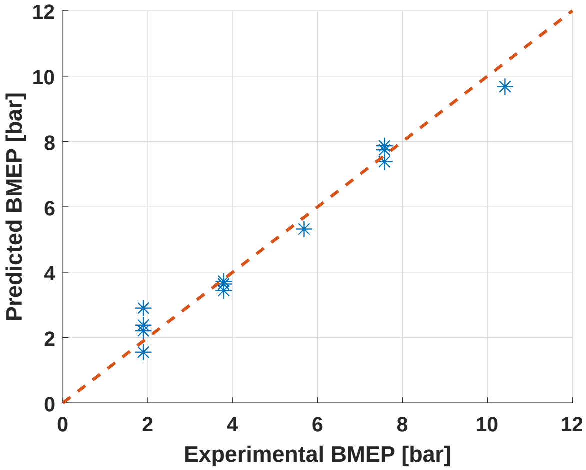

Figure 7.8: Predicted vs Experimental BMEP at steady state

7.3.2.3 Dynamic models

The effect of engine dynamics on the transient NO_x and BMEP are approximated by two separate first order lags as follows:

$$NO_{x,t}(s) = \frac{1}{\tau_{NOx}s+1}NO_{x,ss}(s) \tag{7.9}$$

$$BMEP(s) = \frac{1}{\tau_{BMEP}s+1}BMEP_{ss}(s) \tag{7.10}$$

where, $NO_{x,t}(s)$ and $BMEP(s)$ are the transient $\mathrm{NO_x}$ emission and BMEP respectively while $NO_{x,ss}(s)$ and $BMEP_{ss}(s)$ are the steady state $\mathrm{NO_x}$ and BMEP respectively, all in Laplace domain. The first order lag time constant for $\mathrm{NO_x}$, τ_{NOx}, is larger than the time constant for the BMEP τ_{BMEP} due to the lag associated with the flow of the exhaust gas through the engine exhaust manifold and exhaust pipe [199] and the lag associated with diffusion of species through the $\mathrm{NO_x}$ sensor. The time constant parameters for $\mathrm{NO_x}$ and BMEP are estimated based on the experimental data and are found to be 1 seconds and 0.2 seconds respectively [199].

7.3.2.4 Control oriented model

To derive the discrete control oriented model, first the first order lags are written in discrete form. For a sampling interval of h_t, the $\mathrm{NO_x}$ concentration at step k+1 is calculated as follows:

$$NO_x(k+1) = (1 - \frac{h_t}{\tau_{NOx}+h_t})NO_x(k) + \frac{h_t}{\tau_{NOx}+h_t}NO_{x,ss}(k+1) \tag{7.11}$$

and the BMEP at step k+1 is calculated using the following equation:

$$BMEP(k+1) = (1 - \frac{h_t}{\tau_{BMEP}+h_t})BMEP(k) + \frac{h_t}{\tau_{BMEP}+h_t}BMEP_{ss}(k+1) \tag{7.12}$$

where $NO_{x,ss}(k+1)$ and $BMEP_{ss}(k+1)$ are the steady state $\mathrm{NO_x}$ and output BMEP calculated using Eqn. (7.7) and Eqn. (7.8) respectively.

The model inputs, states, parameters and outputs are formulated as vectors. The vector $\mathbf{x}$ contains two model states:

$$\mathbf{x(k)} = \begin{bmatrix} NO_x(k) & \tau(k) \end{bmatrix} \tag{7.13}$$

The vector $\mathbf{u}$ contains three model inputs:

$$\mathbf{u(k)} = \begin{bmatrix} n(k) & m_f(k) & P_r(k) \end{bmatrix} \tag{7.14}$$

The vector $\boldsymbol{\zeta}$ contains 14 model parameters:

$$\boldsymbol{\zeta} = \begin{bmatrix} T \; \tau_{NOx} \; \tau_{BMEP} \; a_o \; a_1 \; a_2 \; a_3 \; a_4 \; a_5 \; a_6 \; a_7 \; b_o \; b_1 \; b_2 \end{bmatrix} \tag{7.15}$$

The vector $\mathbf{y}$ contains two model outputs:

$$\mathbf{y(k)} = \begin{bmatrix} x_1(k) & x_2(k) \end{bmatrix} \tag{7.16}$$

The control oriented model states result from combining Eqn. (7.7 to 7.8) with Eqn. (7.11 to 7.15) and is:

$$\begin{aligned} \mathbf{x_1}(k+1) = \left(1 - \frac{\zeta_1}{\zeta_2+\zeta_1}\right)x_1(k) + \frac{\zeta_1}{\zeta_2+\zeta_1}\Bigg(\zeta_4 + \zeta_5 u_2(k) + \zeta_6\Big[u_2(k)\Big]^2 + \\ \zeta_7\Big[u_2(k)\Big]^3 + \zeta_8 u_3(k) + \zeta_9\Big[u_3(k)\Big]^2 + \zeta_{10}u_1(k) + \zeta_{11}\Big[u_1(k)\Big]^2\Bigg) \end{aligned} \tag{7.17}$$

$$\mathbf{x_2}(k+1) = \left(1 - \frac{\zeta_1}{\zeta_3+\zeta_1}\right)x_2(k) + \frac{\zeta_1}{\zeta_3+\zeta_1}\zeta_{12}\left(\Big[u_1(k)\Big]^{\zeta_{13}}\Big[u_2(k)\Big]^{\zeta_{14}}\right) \tag{7.18}$$

7.3.3 Results and discussion

To evaluate the effect of transient inputs on the model outputs, the model response to step changes in fuel rail pressure and injection amount are simulated and compared to the measured experimental results in Fig. 7.9. The control oriented model transient response matches the experiments with maximum error of 18.1 % for NO_x and 10.3 % for BMEP. The engine speed is kept constant (1500 rpm) for the simulations. The engine NO_x emission and BMEP both increase as the amount of injected fuel increases. By increasing the injection amount, the overall in-cylinder heat release increases which will increase the indicated engine power and therefore the BMEP at a constant engine speed. This also increases the maximum in-cylinder temperature and consequently increases the NO_x production. On the other hand, the engine NO_x emission decreases by decreasing the injected fuel rail pressure as shown in Fig. 7.9. Reducing the injection rail pressure can reduce the the heat release rate and consequently reduces the maximum in-cylinder temperature [200], and therefore reduces the NO_x production rate [201]. This effect may vary at different engine operating conditions and injection timings including multiple injections, which are not captured by the control oriented model proposed.

7.3.4 Conclusions

A MIMO control oriented diesel engine NO_x emission and output BMEP model is developed based on the experimental data carried out on a on a 4.5L medium duty diesel engine. The engine NO_x emission is measured with a fast response electrochemical NO_x sensor at different engine operating conditions with engine speed between 1000 rpm to 2500 rpm and BMEP between 1.9 bar and 17.4 bar. The injected fuel amount, the injection rail pressure and the engine speed are considered as the model inputs. The model transient response to step changes of injection pressure and injected fuel

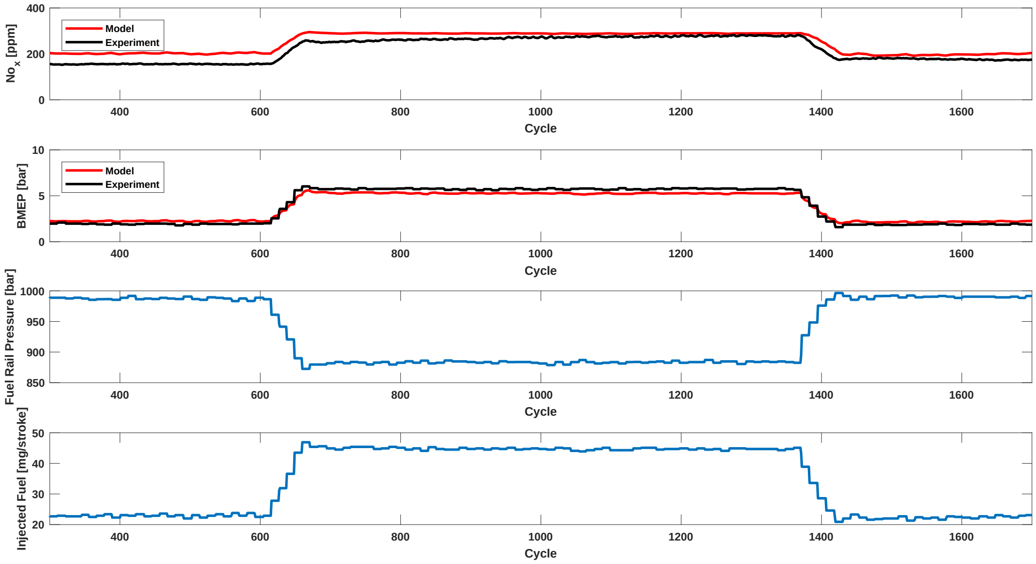

Figure 7.9: NO_x and BMEP transient response of the engine control oriented model compared to measurement for input of injected fuel amount and rail pressure and measured NO_x and BMEP. Engine speed = 1500 rpm

amount is also studied and the model accuracy is compared to the experimental engine transient response. The control oriented model transient response matches the experiments with maximum error of 16 % for NO_x and 7.9 % for BMEP.

The control oriented model is suitable for on board diagnostics and engine control with a fast-response NO_x sensor feedback [202].

Engine Coolant Temperature (^oC)	Engine Speed [RPM]	Injected fuel [mg/stroke]	Fuel rail pressure [bar]	NO_x concentration [ppm]	BMEP [bar]
82	1010	15.8	709	335	1.9
82	1007	29.6	833	585	3.8
83	1514	22.3	990	152	1.9
83	1512	33.1	943	220	3.8
84	1513	57.9	817	281	7.6
87	1514	113.8	1044	790	17.0
87	1514	22	985	317	1.9
87	1514	45.3	885	519	7.6
87	2002	24.8	1042	104	1.9
85	2001	35.3	1024	135	3.8
81	2001	63	832	144	7.6
88	1946	116.3	1206	582	17.0
85	2498	30.1	1058	77	1.9
83	2524	66.3	1031	165	7.6
87	2526	78.1	1420	350	10.4

Table 7.2: Steady state diesel engine test results for NO_x and BMEP

Table 7.3: Steady state $\mathrm{NO_x}$ model parameters

a_0	a_1	a_2	a_3
708.498	19.41075	- 1.627061	0.08590996
a_4	a_5	a_6	a_7
3.8838	-0.0735	- 1.925×10^{-6}	1.413×10^{-3}

Table 7.4: Steady state BMEP model parameters

b_0	b_1	b_2
0.1755	-0.1982	1.277

Chapter 8

Conclusions

Conclusions for experimental and modeling results are presented in this chapter.

8.1 Sensor model summary (Chapters 4 and 5)

Molecular diffusion was found to be the dominant diffusion mechanism of a production amperometric NO_x sensor. The sensor temperature was changed using a sensor control module to evaluate the effect of temperature on sensor outputs which was proportional to the diffusive flux of species through the barriers. The sensor dimensions were obtained from x-ray images of the internal parts (chambers and barriers) and were used in the model.

Knudsen diffusion mechanism, multi component molecular diffusion mechanism and mixture averaged method (molecular and Knudsen diffusion) were evaluated by varying the sensor temperatures and comparing the model output to the experiments. A sensor model is developed based on the molecular diffusion to calculate the sensor outputs for O_2 and NO_x concentrations corresponding to engine off and three engine operating conditions. The sensor model output closely matches the experiments at different engine operating conditions and different concentration of species in the exhaust gas with maximum error of 0.79% for oxygen measurement output (I_{P1}) and maximum error of 4.85% for NO_x measurement output (I_{P2}). The developed sensor model can be used to reduce the effect of manufacturing deviations on the sensor output signals and the measurement error without re-calibrating the sensor. The diffusion model is an essential element of the sensor model and will be used in the future to develop more complex sensor models incorporating electrode reactions and electrochemical models.

The full range of the sensing cell current-voltage curve of an amperometric NO_x sensor was experimentally studied and then simulated. First, diffusion of the sample gas species through the sensor porous diffusion barriers and sensor chambers were modeled. Then, the diffusion model was coupled to an electrochemical model to predict the current-voltage curve of the NO_x sensing cell. The ohmic loss, activation loss and concentration loss have been included in the electrochemical submodel. To validate the sensor model at different operating conditions, the sensor was installed on the exhaust pipe of a medium duty 4.5 L Diesel engine, a 3 L port injection spark ignition engine and a sensor test-rig that provides fully controlled gas mixtures. Experiments were carried out at different engine operating conditions to provide a wide range of NO_x concentrations for NO_x sensor model validation. The sensor model consists of 4 non-linear equations with 3 inputs, 23 parameters and 3 constants. The NO_x sensing cell voltage was changed from the open-circuit cell voltage, which corresponds to zero current density, to 0.45 V that corresponds to the limiting current of the NO_x sensing cell.

It is shown that NO partially reduces in the first chamber which affects the NO_x sensing cell open-circuit potentials. The experimental open-circuit potential at different concentrations were defined and then implemented in the model to simulate NO reduction in the first chamber at $I_{P2} = 0$. The model results for the limiting current and the pumping current of the NO_x sensing cell closely match the experiments for a wide range of cell voltages and different engine operating points with different NO_x concentrations up to more than 2800 ppm.

8.2 Cross sensitivity analysis summary (Chapter 6)

8.2.1 Cross sensitivity to ammonia

Ammonia cross sensitivity of a production NO_x sensor is modeled for slow transients. The most effective factors on cross sensitivity were evaluated to get the best accuracy against the experiments. The model is validated for large amounts of ammonia slip. A dynamic production NO_x sensor model is then developed to remove ammonia cross sensitivity and to decompose the NO_x sensor output signal. A basic model is derived for the cross sensitivity factor based on the experiment data as a function of exhaust gas temperature. The model is then improved for transients by considering a correction factor as a function of normalized ammonia slip rate (NASR). A three-state nonlinear control oriented SCR model is also developed and used to predict the NH_3 concentration downstream of the SCR. The SCR model and the sensor model are finally coupled and NO_x concentration is estimated using the NO_x sensor signal decomposition. The validation results confirms that the model is capable to accurately estimate the actual NO_x concentration based on the NH_3 concentration upstream of the SCR and the NO_x sensor output signal. This model can be used for future engine emission control strategies such as SCR control.

8.2.2 Sensitivity to hydrocarbons

A three-chamber limiting-current-type amperometric HC sensor is used and parameterized to measure propane concentration. First, the sensor stability is optimized by changing the sensor operating parameters including the sensor temperature, the reference cell potential, and the stabilizing cell potential. The stability tests are carried out on a controlled sensor test rig at a reaction rate determining operating condition with propane concentration of 5000 ppm (balanced with nitrogen). Based on the experiments, the sensor has the most stable performance at sensor temperature of

1009 K, the reference cell potential of 0.67 V and the stabilizing cell potential of 0.45 V. It is shown that the presence of CO_2 does not have a significant effect on the sensor sensitivity to propane and the sensor transient behavior.

To find the diffusion-rate-determined operating region, the linearity of sensor steady state response vs propane concentration is experimentally studied at the optimum sensor operating conditions. The sensor is shown to have a linear sensitivity to propane concentration from 0 to 3200 ppm which reveals the diffusion rate determining operating region of the sensor.

To study the sensor transient behavior in diffusion rate determining operating region, the sensor response time is examined for step changes from zero propane concentration to different propane concentrations. It is shown that the sensor response time is almost the same for step changes of propane concentration from zero to different concentrations and is equal to 38 seconds.

8.2.3 The effect of sensor inputs on sensor sensitivity to NO_x

The effect of three main operating parameters of an amperometric NO_x-O_2 sensor on the sensor behavior was experimentally studied and the results were justified with the physical understanding of the sensor working principles. The effect of sensor operating temperatures, the reference cell potential and the NO_x sensing cell potential on the sensor response linearity and the sensor sensitivity to NO_x were examined. The experimental results show that:

- The sensor sensitivity to NO_x decreases by increasing the sensor temperature. Increasing the sensor temperature to more than the sensor typical temperature (1023 K), reduces the sensor response linearity to NO_x concentration.
- Reducing the reference cell potential from the typical cell potential (0.42 V) increases the NO_x sensor response offset at low NO_x concentrations but also re-

duces the sensor cross-sensitivity to O_2 particularly at high NO_x concentrations (>600 [ppm]).

- The sensor sensitivity increases gradually as the NO_x sensing cell potential increases while the sensor output becomes almost linearly dependent on NO_x concentration for cell potentials higher than ≈ 0.25 V.

This improved understanding of the sensor has the potential to remove cross-sensitivity for emission measurements of gases containing NO_x and other species in the exhaust gas such as unburned hydrocarbons and NH_3.

8.3 On Board Diagnostics (OBD) summary (Chapter 7)

8.3.1 Sensor OBD

An on-board diagnostics strategy was developed using a physics-based model of an amperometric NO_x-O_2 sensor. The model predicts the sensor O_2 output as a function of sensor temperature and oxygen concentration based on multi component molecular diffusion mechanism of exhaust gas species through the sensor. A temperature perturbation method was proposed and used to calibrate the sensor output with respect to oxygen concentration. To evaluate the accuracy of the model in steady state and transients, temperature perturbation tests for both rising and falling sensor temperature steps are performed experimentally and the model results closely match the experiments.

A two step sensor diagnostics strategy was then proposed to evaluate the sensor output based on the sensor output validity range and a model-based diagnostics strategy that includes a temperature perturbation test. A self-calibration procedure was included in the diagnostics procedure which requires an external relative humidity measurement.

The plausibility of the sensor output as well as the performance of sensor heater and diffusion barriers can be evaluated with the proposed physics-based diagnostics strategy.

8.3.2 Control oriented engine NO_x model

A MIMO control oriented diesel engine NO_x emission and output BMEP model is developed based on the experimental data carried out on a on a 4.5L medium duty diesel engine. The engine NO_x emission is measured with a fast response electrochemical NO_x sensor at different engine operating conditions with engine speed between 1000 rpm to 2500 rpm and BMEP between 1.9 bar and 17.4 bar. The injected fuel amount, the injection rail pressure and the engine speed are considered as the model inputs. The model transient response to step changes of injection pressure and injected fuel amount is also studied and the model accuracy is compared to the experimental engine transient response. The control oriented model transient response matches the experiments with maximum error of 16 % for NO_x and 7.9 % for BMEP.

The control oriented model is suitable for on board diagnostics and engine control with a fast-response NO_x sensor feedback [202].

References

[1] Asko Vuorinen. *Planning of Optimal Power Systems*. Vammalan Kirjapaino Oy, Vammala, Finland, 2009.

[2] W. Tutak, A. Jamrozik, Á. Bereczky, and K. Lukacs. Effects of injection timing of diesel fuel on performance and emission of dual fuel diesel engine powered by diesel/E85 fuels. *Transport*, 33(3):633–646, 2018.

[3] Timothy V. Johnson. Review of vehicular emissions trends. *SAE Int. J. Engines*, 8, 04 2015.

[4] V. Praveena and M.L.J. Martin. A review on various after treatment techniques to reduce NOx emissions in a CI engine. *Journal of the Energy Institute*, 2017.

[5] P. Geng, Q. Tan, C. Zhang, L. Wei, X. He, E. Cao, and K. Jiang. Experimental investigation on NOx and green house gas emissions from a marine auxiliary diesel engine using ultralow sulfur light fuel. *Science of The Total Environment*, 572(Supplement C):467 – 475, 2016.

[6] I.D. Blanco-Rodriguez. *Modelling and observation of exhaust gas concentrations for diesel engine control*. Springer, 2014.

[7] M Koebel, M Elsener, and M Kleemann. Urea-SCR: a promising technique to reduce NOx emissions from automotive Diesel engines. *Catalysis Today*, 59(34):335 – 345, 2000.

[8] Steven H. Cadle, Patricia A. Mulawa, Eric C. Hunsanger, Ken Nelson, Ronald A. Ragazzi, Richard Barrett, Gerald L. Gallagher, Douglas R. Lawson, Kenneth T. Knapp, and Richard Snow. Composition of Light-Duty Motor Vehicle Exhaust Particulate Matter in the Denver, Colorado Area. *Environmental Science & Technology*, 33(14):2328–2339, 1999.

[9] Jana Moldanov, Erik Fridell, Olga Popovicheva, Benjamin Demirdjian, Victoria Tishkova, Alessandro Faccinetto, and Cristian Focsa. Characterisation of particulate matter and gaseous emissions from a large ship diesel engine. *Atmospheric Environment*, 43(16):2632 – 2641, 2009.

[10] Adam Neer and Umit O. Koylu. Effect of operating conditions on the size, morphology, and concentration of submicrometer particulates emitted from a diesel engine. *Combustion and Flame*, 146(1):142 – 154, 2006.

[11] Yu-Cheng Chang, Wen-Jhy Lee, Tser Son Wu, Chang-Yu Wu, and Shui-Jen Chen. Use of water containing acetonebutanolethanol for nox-pm (nitrogen oxide-particulate matter) trade-off in the diesel engine fueled with biodiesel. *Energy*, 64:678 – 687, 2014.

[12] Thomas Bohl, Andrew Smallbone, Guohong Tian, and Anthony P. Roskilly. Particulate number and NOx trade-off comparisons between HVO and mineral diesel in HD applications. *Fuel*, 215:90 – 101, 2018.

[13] Statistics IEA. International Energy Agency, 2017.

[14] Stefanos Tsiakmakis, Georgios Fontaras, Biagio Ciuffo, and Zissis Samaras. A simulation-based methodology for quantifying European passenger car fleet CO2 emissions. *Applied Energy*, 199:447 – 465, 2017.

[15] Christian Thiel, Johannes Schmidt, Arnold Van Zyl, and Erwin Schmid. Cost and well-to-wheel implications of the vehicle fleet CO2 emission regulation in the European Union. *Transportation Research Part A: policy and practice*, 63:25–42, 2014.

[16] S. Imtenan, M. Varman, H.H. Masjuki, M.A. Kalam, H. Sajjad, M.I. Arbab, and I.M. Rizwanul Fattah. Impact of low temperature combustion attaining strategies on diesel engine emissions for diesel and biodiesels: A review. *Energy Conversion and Management*, 80:329 – 356, 2014.

[17] G Patrick Kealey. Carbon monoxide toxicity. *Journal of Burn Care & Research*, 30(1):146–147, 2009.

[18] Leon D. Prockop and Rossitza I. Chichkova. Carbon monoxide intoxication: An updated review. *Journal of the Neurological Sciences*, 262(1):122 – 130, 2007. Environmental Neurology.

[19] İ.A. Reşitoğlu, K. Altinişik, and A. Keskin. The pollutant emissions from diesel-engine vehicles and exhaust aftertreatment systems. *Clean Technologies and Environmental Policy*, 17(1):15–27, Jan 2015.

[20] Xiaolei Gu, Zuohua Huang, Jian Cai, Jing Gong, Xuesong Wu, and Chia fon Lee. Emission characteristics of a spark-ignition engine fuelled with gasoline-n-butanol blends in combination with EGR. *Fuel*, 93:611 – 617, 2012.

[21] R. Behet, H. Oktay, A. akmak, and H. Aydin. Comparison of exhaust emissions of biodieseldiesel fuel blends produced from animal fats. *Renewable and Sustainable Energy Reviews*, 46:157 – 165, 2015.

[22] H. Li and G. A. Karim. Exhaust emissions from an SI engine operating on

gaseous fuel mixtures containing hydrogen. *International Journal of Hydrogen Energy*, 30(13):1491 – 1499, 2005.

[23] M. M. Maricq, D. H. Podsiadlik, D. D. Brehob, and M. Haghgooie. Particulate Emissions from a Direct-Injection Spark-Ignition (DISI) Engine. In *International Fuels & Lubricants Meeting & Exposition*. SAE International, may 1999.

[24] L.Chen, R. Stone, and D. Richardson. A study of mixture preparation and PM emissions using a direct injection engine fuelled with stoichiometric gasoline/ethanol blends. *Fuel*, 96:120 – 130, 2012.

[25] M. Aliramezani, I. Chitsaz, and A. A. Mozafari. Thermodynamic modeling of partially stratified charge engine characteristics for hydrogen-methane blends at ultra-lean conditions. *International Journal of Hydrogen Energy*, 38(25):10640 – 10647, 2013.

[26] E. P. Brandt, Y. Wang, and J. W. Grizzle. Dynamic modeling of a three-way catalyst for si engine exhaust emission control. *IEEE Transactions on Control Systems Technology*, 8(5):767–776, Sep. 2000.

[27] EPA. 2017 and Later Model Year Light-Duty Vehicle Greenhouse Gas Emissions and Corporate Average Fuel Economy Standards. Regulatory Announcement, EPA-HQ-OAR-2010-0799;FRL-9706-5;NHTSA-2010-0131, October 2012.

[28] T. V. Johnson. Review of vehicular emissions trends. *SAE International Journal of Engines*, 8(3):1152–1167, apr 2015.

[29] F. Posada and A. Bandivadekar. Global overview of on-board diagnostic (OBD) systems for heavy-duty vehicles. *Int. Counc. Clean Transp.*, 2015.

[30] Lev III amendments to the California greenhouse gas and criteria pollutant exhaust and evaporative emission standards and test procedures and to the

on-board diagnostic system requirements for passenger cars, light-duty trucks and medium-duty vehicles and to the evaporative emission requirements for heavy-duty vehicles. California Air Resources Board, 2012.

[31] P. Baltusis. On board vehicle diagnostics. In *Convergence International Congress & Exposition On Transportation Electronics*. Convergence Transportation Electronics Association, oct 2004.

[32] J. Mohammadpour, M. Franchek, and K. Grigoriadis. A survey on diagnostic methods for automotive engines. *International Journal of Engine Research*, 13(1):41–64, 2012.

[33] M. Aliramezani, C.R. Koch, and R.E. Hayes. Estimating tailpipe NOx concentration using a dynamic NOx/ammonia cross sensitivity model coupled to a three state control oriented SCR model. *IFAC-PapersOnLine*, 49(11):8–13, 2016.

[34] F. Tschanz, A. Amstutz, C.H. Onder, and L. Guzzella. Feedback control of particulate matter and nitrogen oxide emissions in Diesel engines. *Control Engineering Practice*, 21(12):1809 – 1820, 2013.

[35] R. Verschaeren, W. Schaepdryver, T. Serruys, M. Bastiaen, L. Vervaeke, and S. Verhelst. Experimental study of NOx reduction on a medium speed heavy duty diesel engine by the application of EGR (exhaust gas recirculation) and Miller timing. *Energy*, 76:614 – 621, 2014.

[36] M. Salazar, S. Hoffmann, L. Tillmann, V. Singer, R. Becker, and W. Grunert. Hybrid catalysts for the selective catalytic reduction (SCR) of NO by NH3: Precipitates and physical mixtures. *Applied Catalysis B: Environmental*, 218(Supplement C):793 – 802, 2017.

[37] B. Guan, R. Zhan, H. Lin, and Z. Huang. Review of state of the art technologies of selective catalytic reduction of NOx from diesel engine exhaust. *Applied Thermal Engineering*, 66(1):395 – 414, 2014.

[38] K. Ebrahimi, M. Aliramezani, and C.R. Koch. An HCCI control oriented model that includes combustion efficiency. *IFAC-PapersOnLine*, 49(11):327–332, 2016.

[39] A. Jain, A. Pratap Singh, and A. Kumar Agarwal. Effect of split fuel injection and EGR on NOx and PM emission reduction in a low temperature combustion (LTC) mode diesel engine. *Energy*, 122(Supplement C):249 – 264, 2017.

[40] T. Ritter, G. Hagen, J. Lattus, and R. Moos. Solid state mixed-potential sensors as direct conversion sensors for automotive catalysts. *Sensors and Actuators B: Chemical*, 2017.

[41] M. Andersson, P. Ljung, M. Mattsson, M. Löfdahl, and A.L. Spetz. Investigations on the possibilities of a MISiCFET sensor system for OBD and combustion control utilizing different catalytic gate materials. *Topics in catalysis*, 30(1-4):365–368, 2004.

[42] A. Iio, H. Ikeda, S. Ayu Anggraini, and N. Miura. Sensing characteristics of YSZ-based oxygen sensors attached with BaxSr1-xFeO3 sensing-electrode. *Solid State Ionics*, 285(Supplement C):234 – 238, 2016. The 40th Symposium on Solid State Ionics in Japan.

[43] A.W. Osburn, C. Ferguson, T.J. Hall, and B.P. Liimatta. NOx sensor diagnostic for an exhaust aftertreatment system, June 30 2016. US Patent App. 14/586,174.

[44] C. Nagel, A. Franz, and T. Pfister. Method for checking the plausibility of a

NOx sensor in an SCR catalytic converter system, May 11 2017. US Patent App. 15/346,227.

[45] X. Gao, T. Liu, X. Zhang, B. He, and J. Yu. Properties of limiting current oxygen sensor with La0.8Sr0.2Ga0.8Mg0.2O3 solid electrolyte and La0.8Sr0.2(Ga0.8Mg0.2)1-xCrxO3- dense diffusion barrier. *Solid State Ionics*, 304(Supplement C):135 – 144, 2017.

[46] A.D. Hunter. Method, apparatus, and system for diagnosing at least one NOx sensor of a diesel engine system, April 12 2017. EP Patent App. EP20,160,177,457.

[47] P. Mock and V. Franco. Developments in automotive emissions in the eu and globally. In *4th International Exhaust Emissions Symposium, Bielsko-Biala (Poland)*, 2014.

[48] J. May, D. Bosteels, and C. Favre. A comparison of light-duty vehicle emissions over different test cycles and in real driving conditions. In *FISITA Conference, Maastricht*, 2014.

[49] T. G. Vlachos, P. Bonnel, A. Perujo, M. Weiss, P. Mendoza Villafuerte, and F. Riccobono. In-use emissions testing with portable emissions measurement systems (PEMS) in the current and future European vehicle emissions legislation: Overview, underlying principles and expected benefits. *SAE International Journal of Commercial Vehicles*, 7(2014-01-1549):199–215, 2014.

[50] M. Aliramezani, C.R. Koch, R.E. Hayes, and R. Patrick. Amperometric solid electrolyte NOx sensors – the effect of temperature and diffusion mechanisms. *Solid State Ionics*, 313(Supplement C):7 – 13, 2017.

[51] M. Aliramezani, C.R. Koch, M. Secanell, R.E. Hayes, and R. Patrick. An electrochemical model of an amperometric NOx sensor. *Sensors and Actuators B*, 290:302–311, 2019.

[52] M. Aliramezani, C.R. Koch, and R. Patrick. A variable-potential limiting-current-type amperometric hydrocarbon sensor. *IEEE Sensors Journal (Submitted)*, 2019.

[53] M. Aliramezani and C. R. Koch. The effect of operating parameters of an amperometric NOx - O2 sensor on the sensor response. *Symposium for Combustion Control, Aachen, 2019*, 2019.

[54] M. Aliramezani, C.R. Koch, and R. Patrick. Phenomenological model of a solid electrolyte NOx and O2 sensor using temperature perturbation for on-board diagnostics. *Solid State Ionics*, 321:62 – 68, 2018.

[55] M. Aliramezani, A. Norouzi, and C. R. Koch. A control oriented diesel engine NOx emission model for on board diagnostics and engine control with sensor feedback. *Proceedings of Combustion Institute - Canadian Section (CICS)*, 2019.

[56] A. G. Konstandopoulos, M. Kostoglou, E. Skaperdas, E. Papaioannou, D. Zarvalis, and E. Kladopoulou. Fundamental studies of diesel particulate filters: transient loading, regeneration and aging. Technical report, SAE Technical Paper, 2000.

[57] W Addy Majewski and Magdi K Khair. *Diesel emissions and their control.* Society of Automotive Engineers, 2006.

[58] M. Zheng, G.T. Reader, and J.G. Hawley. Diesel engine exhaust gas recirculationa review on advanced and novel concepts. *Energy Conversion and Management*, 45(6):883 – 900, 2004.

[59] Y. Kong, T. Kozakiewicz, R. Johnson, C. Huffmeyer, J. Huckaby, J. Abel, J. Baurley, and K. Duffield. Active dpf regeneration for 2007 diesel engines. In *2005 SAE Commercial Vehicle Engineering Conference*. SAE International, nov 2005.

[60] T.P. Kotrba, A.and Gardner, L. Bai, and A. Yetkin. Passive regeneration response characteristics of a DPF system. Technical report, SAE Technical Paper, 2013.

[61] Kiran C. Premchand, Harsha Surenahalli, and John H. Johnson. Particulate matter and nitrogen oxides kinetics based on engine experimental data for a catalyzed diesel particulate filter. In *SAE Technical Paper*. SAE International, 04 2014.

[62] Pingen Chen, Umar Ibrahim, and Junmin Wang. Experimental investigation of diesel and biodiesel post injections during active diesel particulate filter regenerations. *Fuel*, 130:286–295, 2014.

[63] A. Abedi. *The Effect of an Axial Catalyst Distribution on the Performance of a Diesel Oxidation Catalyst and Inverse Hysteresis Phenomena during CO and C3H6 Oxidation*. PhD thesis, 2012.

[64] F. Haaß and H. Fuess. Structural characterization of automotive catalysts. *Advanced Engineering Materials*, 7(10):899–913, 2005.

[65] R.M. Heck and R.J. Farrauto. Automobile exhaust catalysts. *Applied Catalysis A: General*, 221(1):443–457, 2001.

[66] T. C. Watling, M. Ahmadinejad, M. Ţuţuianu, Å. Johansson, and M. AJ. Paterson. Development and validation of a Pt-Pd diesel oxidation catalyst model. *SAE International Journal of Engines*, 5(2012-01-1286):1420–1442, 2012.

[67] A. Aksikas, I. Aksikas, R.E. Hayes, and J.F. Forbes. Model-based optimal boundary control of Selective Catalytic Reduction in diesel-powered vehicles. *Journal of Process Control*, 71:63 – 74, 2018.

[68] H. Zhang and J. Wang. Ammonia coverage ratio and input simultaneous estimation in ground vehicle selective catalytic reduction (SCR) systems. *Journal of the Franklin Institute*, 352(2):708 – 723, 2015. Special Issue on Control and Estimation of Electrified vehicles.

[69] A. Frobert, S. Raux, Y. Creff, and E. Jeudy. About cross-sensitivities of NOx sensors in SCR operation. SAE 2013-01-1512.

[70] D. Wang, S. Yao, M. Shost, J. Yoo, D. Cabush, D. Racine, R. Cloudt, and F. Willems. Ammonia sensor for closed-loop scr control. *SAE Int. J. Passeng. Cars Electron. Electr. Syst.*, 1:323–333, 04 2008.

[71] P. Chavannavar. Development and Implementation of a Mapless, Model Based SCR Control System. *SAE Int. J. Engines*, 7:1113–1124, 07 2014.

[72] P. Forzatti. Present status and perspectives in de-NOx SCR catalysis. *Applied Catalysis A: General*, 222(12):221 – 236, 2001. Celebration Issue.

[73] M. Devarakonda, G. Parker, J.H. Johnson, and V. Strots. Model-based control system design in a urea-SCR aftertreatment system based on NH3 sensor feedback. *International Journal of Automotive Technology*, 10(6):653–662, 2009.

[74] M. Devarakonda, G. Parker, J. H. Johnson, V. Strots, and S. Santhanam. Model-based estimation and control system development in a Urea-SCR aftertreatment system. *SAE Int. J. Fuels Lubr.*, 1:646–661, 04 2008.

[75] J. C. Peyton Jones and M. Geveci. Smart sensing and decomposition of NOx

and NH3 components from production nox sensor signals. *SAE Int. J. Engines*, 4:1393–1401, 04 2011.

[76] H. Zhang, J. Wang, and Y.Y. Wang. Removal of sensor ammonia cross sensitivity from contaminated measurements in Diesel-engine selective catalytic reduction systems. *Fuel*, 150(0):448 – 456, 2015.

[77] F. Willems, R. Cloudt, E. Van den Eijnden, M. Van Genderen, R. Verbeek, B. de Jager, W. Boomsma, and I. Van den Heuvel. Is closed-loop SCR control required to meet future emission targets? SAE 2007-01-1574, 04 2007.

[78] S. Chuepeng, K. Theinnoi, and M. Tongroon. Combustion Characteristics and Particulate Matter Number Size Study of Ethanol and Diesel Reactivity Controlled Compression Ignition Engine. In *13th International Conference on Engines & Vehicles*. SAE International, sep 2017.

[79] C. S. Sluder, R. M. Wagner, S. A. Lewis, and J. M. E. Storey. Exhaust chemistry of Low-NOx, Low-PM Diesel Combustion. In *SAE Technical Paper*. SAE International, 03 2004.

[80] A. Maiboom, X. Tauzia, and J.-F. Hétet. Experimental study of various effects of Exhaust Gas Recirculation (EGR) on combustion and emissions of an automotive direct injection Diesel engine. *Energy*, 33(1):22–34, 2008.

[81] C. Guardiola, J.J. Lpez, J. Martn, and D. Garca-Sarmiento. Semiempirical in-cylinder pressure based model for NOx prediction oriented to control applications. *Applied Thermal Engineering*, 31(16):3275 – 3286, 2011.

[82] H. Haga, H. Kojima, N. Fukushi, N. Ohya, and T. Mito. Optimized NH3 storage control for next generation urea-SCR system. SAE 2013-01-1512.

[83] V. Betageri and R. Mahesh. Effects of the real driving conditions on the NOx emission of a medium duty diesel commercial vehicle. In *Symposium on International Automotive Technology 2017*. SAE International, January 2017.

[84] R. Kaushik, A.and Kumar, S.K. Arya, M. Nair, B.D. Malhotra, and S. Bhansali. Organic–inorganic hybrid nanocomposite-based gas sensors for environmental monitoring. *Chemical Reviews*, 115(11):4571–4606, 2015. PMID: 25933130.

[85] P. Carullo, M. Chino, G.P. Cetrangolo, S. Terreri, A. Lombardi, G. Manco, A. Cimmino, and F. Febbraio. Direct detection of organophosphate compounds in water by a fluorescence-based biosensing device. *Sensors and Actuators B: Chemical*, 255:3257 – 3266, 2018.

[86] C. Di Natale, R. Paolesse, E. Martinelli, and R. Capuano. Solid-state gas sensors for breath analysis: A review. *Analytica Chimica Acta*, 824:1 – 17, 2014.

[87] G.S. Korotchenkov. *Chemical Sensors: Simulation and Modeling Volume 2: Conductometric-Type Sensors.*, volume 2 of *Chemical Sensors*. Momentum Press, 2012.

[88] Y. Liu, J. Parisi, X. Sun, and Y. Lei. Solid-state gas sensors for high temperature applications–a review. *Journal of Materials Chemistry A*, 2(26):9919–9943, 2014.

[89] M. Günter, F. Hammer, C. Koch, K. Kuhn, M. G Rose, and S. Staudacher. Application of a miniaturized solid state electrolyte sensor for tracer gas measurements in a two-stage low pressure turbine. *Experimental Thermal and Fluid Science*, 82:367–374, 2017.

[90] F. Liu, B. Wang, X. Yang, Y. Guan, Q. Wang, X. Liang, P. Sun, Y. Wang, and G. Lu. High-temperature NO2 gas sensor based on stabilized zirconia and

CoTa2O6 sensing electrode. *Sensors and Actuators B: Chemical*, 240:148 – 157, 2017.

[91] T. Ritter, G. Hagen, J. Kita, S. Wiegrtner, F. Schubert, and R. Moos. Self-heated HTCC-based ceramic disc for mixed potential sensors and for direct conversion sensors for automotive catalysts. *Sensors and Actuators B: Chemical*, 248:793 – 802, 2017.

[92] M. Croset, Ph. Schnell, G. Velasco, and J. Siejka. Study of calcia-stabilized zirconia thin-film sensors. *Journal of Vacuum Science and Technology*, 14(3):777–781, 1977.

[93] J. Riegel, H. Neumann, and H. M. Wiedenmann. Exhaust gas sensors for automotive emission control. *Solid State Ionics*, 152:783–800, 2002.

[94] R. Ramamoorthy, P. K. Dutta, and S. A. Akbar. Oxygen sensors: Materials, methods, designs and applications. *Journal of Materials Science*, 38(21):4271–4282, Nov 2003.

[95] J.C. Amphlett, R.M. Baumert, R.F. Mann, B.A. Peppley, P.R. Roberge, and T.J. Harris. Performance modeling of the Ballard Mark IV solid polymer electrolyte fuel cell I. Mechanistic model development. *Journal of the Electrochemical Society*, 142(1):1–8, 1995.

[96] T. Liu, X. Zhang, L. Yuan, and J. Yu. A review of high-temperature electrochemical sensors based on stabilized zirconia. *Solid State Ionics*, 283:91–102, 2015.

[97] J. R. Macdonald. Impedance spectroscopy. *Annals of Biomedical Engineering*, 20(3):289–305, May 1992.

[98] Y. Liu and Y. Lei. Pt-ceo2 nanofibers based high-frequency impedancemetric gas sensor for selective co and c3h8 detection in high-temperature harsh environment. *Sensors and Actuators B: Chemical*, 188:1141 – 1147, 2013.

[99] L. Y. Woo, R. S. Glass, R. F. Novak, and J. H. Visser. Effect of electrode material and design on sensitivity and selectivity for high temperature impedancemetric NOx sensors. *Journal of The Electrochemical Society*, 157(3):J81–J87, 2010.

[100] K. Shimizu, K. Kashiwagi, H.Nishiyama, S. Kakimoto, S. Sugaya, H. Yokoi, and A. Satsuma. Impedancemetric gas sensor based on Pt and WO3 co-loaded TiO2 and ZrO2 as total NOx sensing materials. *Sensors and Actuators B: Chemical*, 130(2):707 – 712, 2008.

[101] L. Dai, L. Ma, W. Meng, Y. Li, Z. He, and L. Wang. Impedancemetric NO2 sensor based on Pd doped perovskite oxide sensing electrode conjunction with phase angle response. *Electrochimica Acta*, 265:411 – 418, 2018.

[102] M. Nakatou and N. Miura. Impedancemetric sensor based on ysz and in2o3 for detection of low concentrations of water vapor at high temperature. *Electrochemistry Communications*, 6(10):995 – 998, 2004.

[103] M. Nakatou and N. Miura. Detection of combustible hydrogen-containing gases by using impedancemetric zirconia-based water-vapor sensor. *Solid State Ionics*, 176(31):2511 – 2515, 2005. 30th Symposium on Solid State Ionics in Japan.

[104] N. Wu, Z. Chen, J. Xu, M. Chyu, and S. X. Mao. Impedance-metric Pt/YSZ/AuGa2O3 sensor for CO detection at high temperature. *Sensors and Actuators B: Chemical*, 110(1):49 – 53, 2005.

[105] R. Wama, M. Utiyama, V.V. Plashnitsa, and N. Miura. Highly sensitive impedance-based propene sensor using stabilized zirconia and zinc oxide sensing-electrode. *Electrochemistry Communications*, 9(12):2774 – 2777, 2007.

[106] N. Kato, K. Nakagaki, and N. Ina. Thick film ZrO2 NOx sensor. Technical report, SAE Technical Paper, 1996.

[107] U. Asad, R. Kumar, M. Zheng, and J.Tjong. Ethanol-fueled low temperature combustion: A pathway to clean and efficient diesel engine cycles. *Applied Energy*, 157:838 – 850, 2015.

[108] T. Nakamura, Y. Sakamoto, K. Saji, and J. Sakata. NOx decomposition mechanism on the electrodes of a zirconia-based amperometric NOx sensor. *Sensors and Actuators B: Chemical*, 93(1):214–220, 2003.

[109] N. Collings, J.A. Harris, and K. Glover. Estimating IC engine exhaust gas lambda and oxygen from the response of a universal exhaust gas oxygen sensor. *Measurement Science and Technology*, 24(9):095101, 2013.

[110] S. Regitz and N. Collings. Fast response air-to-fuel ratio measurements using a novel device based on a wide band lambda sensor. *Measurement Science and Technology*, 19(7):075201, 2008.

[111] H. Kurosawa, Y. Yan, N. Miura, and N. Yamazoe. Stabilized zirconia-based NOx sensor operative at high temperature. *Solid State Ionics*, 79:338–343, 1995.

[112] A. Dutta, N. Kaabbuathong, M.L. Grilli, E. Di Bartolomeo, and E. Traversa. Study of YSZ-based electrochemical sensors with WO3 electrodes in NO2 and CO environments. *Journal of The Electrochemical Society*, 150(2):H33–H37, 2003.

[113] N.F. Szabo and P.K. Dutta. Correlation of sensing behavior of mixed potential sensors with chemical and electrochemical properties of electrodes. *Solid State Ionics*, 171(3):183–190, 2004.

[114] F. Liu, R. Sun, Y. Guan, X. Cheng, H. Zhang, Y. Guan, X. Liang, P. Sun, and G. Lu. Mixed-potential type NH3 sensor based on stabilized zirconia and Ni3V2O8 sensing electrode. *Sensors and Actuators B: Chemical*, 210:795–802, 2015.

[115] E.H. Schenk, P.A. Burke, and M.A. Centanni. Amperometric gas sensor, December 15 2016. US Patent App. 15/246,827.

[116] L. Wang, B. Han, Z. Wang, L. Dai, H. Zhou, Y. Li, and H. Wang. Effective improvement of sensing performance of amperometric NO2 sensor by Ag-modified nano-structured CuO sensing electrode. *Sensors and Actuators B: Chemical*, 207:791 – 800, 2015.

[117] X. Li, T. Xuan, G. Yin, Z. Gao, K. Zhao, P. Yan, and D. He. Highly sensitive amperometric CO sensor using nanocomposite C-loaded PdCl2CuCl2 as sensing electrode materials. *Journal of Alloys and Compounds*, 645:553 – 558, 2015.

[118] Y. Guan, F. Liu, B. Wang, X. Yang, X. Liang, H. Suo, P. Sun, Y. Sun, J. Ma, J. Zheng, Y. Wang, and G. Lu. Highly sensitive amperometric nafion-based CO sensor using Pt/C electrodes with different kinds of carbon materials. *Sensors and Actuators B: Chemical*, 239:696 – 703, 2017.

[119] M. Bashir, S.R. Patri, and K. Ksr. A low power, high accuracy amperometric potentiostat for NOx gas sensors. In *2016 International Conference on Next Generation Intelligent Systems (ICNGIS)*, pages 1–4, Sept 2016.

[120] A. Kalyakin, J. Lyagaeva, D. Medvedev, A. Volkov, A. Demin, and P. Tsiakaras. Characterization of proton-conducting electrolyte based on La0.9Sr0.1YO3–δ and its application in a hydrogen amperometric sensor. *Sensors and Actuators B: Chemical*, 225:446 – 452, 2016.

[121] Y.G. Lee, H.J. Lee, and A. Jang. Amperometric bromate-sensitive sensor via layer-by-layer assembling of metalloporphyrin and polyelectrolytes on carbon nanotubes modified surfaces. *Sensors and Actuators B: Chemical*, 244:157 – 166, 2017.

[122] R. Sharan, M. Roy, A.K. Tyagi, and A. Dutta. Lanthanum gallate based amperometric electrochemical sensor for detecting ammonia in ppm level: Optimization of electrode compositions. *Sensors and Actuators B: Chemical*, 258:454 – 460, 2018.

[123] J.B. Young and B. Todd. Modelling of multi-component gas flows in capillaries and porous solids. *International Journal of Heat and Mass Transfer*, 48(2526):5338 – 5353, 2005.

[124] N. Collings, K. Hegarty, and T. Ramsander. Steady-state modelling of the universal exhaust gas oxygen (UEGO) sensor. *Measurement Science and Technology*, 23(8):085108, 2012.

[125] J.R. Stetter and J. Li. Amperometric gas sensors – a review. *Chemical reviews*, 108(2):352–366, 2008.

[126] J. Mizusaki, K. Amano, S. Yamauchi, and K. Fueki. Electrode reaction at pt, o2/stabilized zirconia interfaces. part I: Theoretical consideration of reaction model. *Solid State Ionics*, 22(4):313–322, 1987.

[127] T.H. Etsell and S.N. Flengas. Overpotential behavior of stabilized zirconia solid electrolyte fuel cells. *Journal of The Electrochemical Society*, 118(12):1890–1900, 1971.

[128] http://www.ecm-co.com/.

[129] http://www.ecm-co.com/product.asp?ncant.

[130] F. Kong, L. Zhang, J. Zeng, and Y. Zhang. Automatic measurement and control system for vehicle ecu based on can bus. In *IEEE International Conference on Automation and Logistics*, pages 964–968. IEEE, 2007.

[131] P. Ran, B. Wang, and W. Wang. The design of communication convertor based on can bus. In *Industrial Technology, 2008. ICIT 2008. IEEE International Conference on*, pages 1–5. IEEE, 2008.

[132] https://www.cummins.com/engines.

[133] G. Symko. Characterization of the exhaust flow through the diesel oxidation catalyst. Master's thesis, University of Alberta, 2018.

[134] https://www.gmpowertrain.com/.

[135] E. Schnaibel, E. Schneider, K. Henkelmann, F. Blischke, and G. Mallebrein. System for operating a heating element for a ceramic sensor in a motor vehicle, April 1 1997. US Patent 5,616,835.

[136] R. V. Klikach. Investigation and analysis of RCCI using NVO on a converted Spark Ignition engine. Master's thesis, University of Alberta, 2018.

[137] R. Moos. A brief overview on automotive exhaust gas sensors based on electroceramics. *International Journal of Applied Ceramic Technology*, 2(5):401–413, 2005.

[138] G. Lu, Q. Diao, Ch.o Yin, S. Yang, Y. Guan, X. Cheng, and X. Liang. High performance mixed-potential type NOx sensor based on stabilized zirconia and oxide electrode. *Solid State Ionics*, 262:292 – 297, 2014. Solid State Ionics 19 Proceedings of the 19th International Conference on Solid State Ionics.

[139] J. Wang, P. Elumalai, D. Terada, M. Hasei, and N. Miura. Mixed-potential-type zirconia-based NOx sensor using PR-loaded NiO sensing electrode operating at high temperatures. *Solid State Ionics*, 177(26):2305 – 2311, 2006. Solid State Ionics 15: Proceedings of the 15th International Conference on Solid State Ionics, Part II.

[140] H. Sasaki, D. Scholl, M. Parsons, H. Inagaki, K. Shiotani, J. Visser, G. Zawacki, T. Kawai, S. Teramoto, and D. Kubinski. Development of an Al2O3/ZrO2-Composite High-Accuracy NOx Sensor. In *SAE Technical Paper*. SAE International, 04 2010.

[141] A. Kunimoto, M. Hasei, Y. Yan, Y. Gao, T. Ono, and Y. Nakanouchi. New total-NOx sensor based on mixed potential for automobiles. Technical report, SAE Technical Paper, 1999.

[142] H. Inagaki, T. Oshima, S. Miyata, and N. Kondo. NOx meter utilizing ZrO2 pumping cell. Technical report, SAE Technical Paper, 1998.

[143] W. J. Fleming. Physical principles governing nonideal behavior of the zirconia oxygen sensor. *Journal of the Electrochemical Society*, 124(1):21–28, 1977.

[144] W. C. Maskell and B. C. H. Steele. Solid state potentiometric oxygen gas sensors. *Journal of Applied Electrochemistry*, 16(4):475–489, Jul 1986.

[145] Y. Fujio, T. Sato, and N. Miura. Sensing performance of zirconia-based gas sensor using titania sensing-electrode added with palladium. *Solid State Ionics*,

262:266 – 269, 2014. Solid State Ionics 19 Proceedings of the 19th International Conference on Solid State Ionics.

[146] A.D. Brailsford, M. Yussouff, and E.M. Logothetis. Steady state model of electrochemical gas sensors with multiple reactions. *Sensors and Actuators B: Chemical*, 36(1-3):392–397, 1996.

[147] A.D. Brailsford, M. Yussouff, and E.M. Logothetis. A first-principles model of the zirconia oxygen sensor. *Sensors and Actuators B: Chemical*, 44(1):321–326, 1997.

[148] D. T. Huang. An integrated computer model for simulating electrothermomechanical interactions of an exhaust oxygen sensor. *Finite elements in analysis and design*, 37(8):657–672, 2001.

[149] S. Klett, M. Piesche, S. Heinzelmann, H. Weyl, H.M. Wiedenmann, U. Schneider, L. Diehl, and H. Neumann. Numerical and experimental analysis of the momentum and heat transfer in exhaust gas sensors. Technical report, SAE Technical Paper, 2005.

[150] James R Welty, Charles E Wicks, Gregory Rorrer, and Robert E Wilson. *Fundamentals of momentum, heat, and mass transfer*. John Wiley & Sons, 2009.

[151] T. S Auckenthaler, C. H. Onder, and H. P. Geering. Modelling of a solid-electrolyte oxygen sensor. Technical report, SAE Technical Paper, 2002.

[152] R. Ramamoorthy, P.K. Dutta, and S.A. Akbar. Oxygen sensors: materials, methods, designs and applications. *Journal of materials science*, 38(21):4271–4282, 2003.

[153] E.M. Logothetis and R.E. Soltis. Method for determining relative amount of oxygen containing gas in a gas mixture, September 8 1992. US Patent 5,145,566.

[154] S. Arcidiacono, I.V. Karlin, J. Mantzaras, and C.E. Frouzakis. Lattice boltzmann model for the simulation of multicomponent mixtures. *Physical Review E*, 76(4):046703, 2007.

[155] R. B. Bird, W. E. Stewart, and E. N. Lightfoot. *Transport phenomena*. John Wiley & Sons, 2007.

[156] R.J. Millington. Gas diffusion in porous media. *Science*, 130(3367):100–102, 1959.

[157] R. E. Hayes and J.P. Mmbaga. *Introduction to Chemical Reactor Analysis*. CRC Press, 2012.

[158] M.F. Hsieh and J. Wang. Development and experimental studies of a control-oriented SCR model for a two-catalyst urea-SCR system. *Control Engineering Practice*, 19(4):409 – 422, 2011.

[159] S. Zhuiykov, T. Ono, N. Yamazoe, and N. Miura. High-temperature NOx sensors using zirconia solid electrolyte and zinc-family oxide sensing electrode. *Solid State Ionics*, 152:801–807, 2002.

[160] T. Ono, M. Hasei, A. Kunimoto, and N. Miura. Improvement of sensing performances of zirconia-based total NOx sensor by attachment of oxidation-catalyst electrode. *Solid State Ionics*, 175(1):503–506, 2004.

[161] R.F. Mann, J.C. Amphlett, M.A. Hooper, H.M. Jensen, B.A. Peppley, and P.R. Roberge. Development and application of a generalised steady-state electrochemical model for a PEM fuel cell. *Journal of power sources*, 86(1-2):173–180, 2000.

[162] M.S. Silberberg, P. Amateis, S.. Lavieri, and R. Venkateswaran. *Chemistry:*

The molecular nature of matter and change. Mosby St. Louis, Missouri, USA, 1996.

[163] F Kundracik, M Hartmanov, J Mllerov, M Jergel, I Kosti, and R Tucoulou. Ohmic resistance of thin yttria stabilized zirconia film and electrodeelectrolyte contact area. *Materials Science and Engineering: B*, 84(3):167 – 175, 2001.

[164] V.M. Janardhanan and O. Deutschmann. Modeling of solid-oxide fuel cells. *Zeitschrift für Physikalische Chemie*, 221(4):443–478, 2007.

[165] A.R. Conn, N.I. Gould, and Ph.L. Toint. *Trust region methods*, volume 1. Siam, 2000.

[166] E. W Lemmon, M. L. Huber, and M. O. McLinden. NIST reference fluid thermodynamic and transport properties - REFPROP. *NIST standard reference database*, 23:v7, 2002.

[167] M. F. Hsieh and J. Wang. An extended Kalman filter for NOx sensor ammonia cross-sensitivity elimination in selective catalytic reduction applications. In *American Control Conference (ACC), 2010*, pages 3033–3038, June 2010.

[168] A. Bonfils, Y. Creff, O. Lepreux, and N. Petit. Closed-loop control of a SCR system using a NOx sensor cross-sensitive to NH3. *Journal of Process Control*, 24(2):368 – 378, 2014. ADCHEM 2012 Special Issue.

[169] C.M. Schar, C. Onder, and H. Geering. Control of an SCR catalytic converter system for a mobile heavy-duty application. *IEEE Transactions on Control Systems Technology*, 14(4):641–653, July 2006.

[170] E. Tronconi, L. Lietti, P. Forzatti, and S. Malloggi. Experimental and theoretical investigation of the dynamics of the SCR - denox reaction. *Chemical*

Engineering Science, 51(11):2965 – 2970, 1996. Chemical Reaction Engineering: From Fundamentals to Commercial Plants and Products.

[171] S. Sasaki, J. Sarlashkar, G. D. Neely, J. Wang, Q. L., and H. Sono. Investigation of alternative combustion, airflow-dominant control and aftertreatment system for clean Diesel vehicles. SAE 2007-01-1937, 07 2007.

[172] M. Upadhyay, D. Van Nieuwstadt. Model based analysis and control design of a Urea-SCR deNOx aftertreatment system. *Journal of Dynamic Systems, Measurement, and Control*, 128:737–741, 2006.

[173] H. K. Gatty, S. Leijonmarck, M. Antelius, G. Stemme, and N. Roxhed. An amperometric nitric oxide sensor with fast response and ppb-level concentration detection relevant to asthma monitoring. *Sensors and Actuators B: Chemical*, 209:639 – 644, 2015.

[174] S. L. Ntella, F. Stradolini, A. Tuoheti, D. Demarchi, A. A. Hatzopoulos, and S. Carrara. Architecture and procedures for ph and temperature monitoring in medical applications. In *2017 IEEE SENSORS*, pages 1–3, Oct 2017.

[175] M. Hossain, J. Saffell, and R. Baron. Differentiating NO2 and O3 at low cost air quality amperometric gas sensors. *ACS Sensors*, 1(11):1291–1294, 2016.

[176] Ronan Baron and John Saffell. Amperometric gas sensors as a low cost emerging technology platform for air quality monitoring applications: A review. *ACS Sensors*, 2(11):1553–1566, 2017. PMID: 29025261.

[177] A. Dutta, T. Ishihara, H. Nishiguchi, and Y. Takita. Amperometric solid-state gas sensor using LaGaO3 based perovskite oxide electrolyte for detecting hydrocarbon in exhaust gas II. improvement of inactive electrode performance. *Journal of The Electrochemical Society*, 151(5):H122–H127, 2004.

[178] A. Dutta, H. Nishiguchi, Y. Takita, and T. Ishihara. Amperometric hydrocarbon sensor using La (Sr) Ga (Fe) O3 solid electrolyte for monitoring in exhaust gas. *Sensors and Actuators B: Chemical*, 108(1-2):368–373, 2005.

[179] J. Riegel, H. Neumann, and H.M. Wiedenmann. Exhaust gas sensors for automotive emission control. *Solid State Ionics*, 152-153:783 – 800, 2002. Proceedings of international conference on solid state ionics, (materials and processes for energy and environment), Cairns, Australia, 8-13 July, 2001.

[180] F. S. de Souza, T.G. Costa, M.J. Feldhaus, B. Szpoganicz, and A. Spinelli. Nonenzymatic amperometric sensors for hydrogen peroxide based on Melanin-Capped Fe 3+, Cu 2+, or Ni 2+ modified Prussian Blue nanoparticles. *IEEE Sensors Journal*, 15(9):4749–4757, 2015.

[181] G. Korotcenkov. *Chemical Sensors: Simulation and Modeling Volume 1: Microstructural Characterization and Modeling of Metal Oxides*, volume 1. Momentum Press, 2012.

[182] W.L. Liu, Y.Y. Liu, and J.S. Do. Room temperature amperometric ammonia sensor based on Pt and Pt–Ir porous ceramic electrodes. *IEEE Sensors Journal*, 16(7):1872–1879, 2016.

[183] I. Soykal, P.H. Matter, L.B. Thrun, R.Q. Long, S.L. Swartz, and U.S. Ozkan. Amperometric NO x sensor based on oxygen reduction. *IEEE Sensors Journal*, 16(6):1532–1540, 2016.

[184] T. Ishihara, M. Fukuyama, A. Dutta, K. Kabemura, H. Nishiguchi, and Y. Takita. Solid state amperometric hydrocarbon sensor for monitoring exhaust gas using oxygen pumping current. *Journal of The Electrochemical Society*, 150(10):H241–H245, 2003.

[185] I.I. Soykal, P.H. Matter, L.B. Thrun, R.Q. Long, S.L. Swartz, and U.S. Ozkan. Amperometric NOx sensor based on oxygen reduction. *IEEE Sensors Journal*, 16(6):1532–1540, March 2016.

[186] P. Teunissen. Nonlinear least squares. *Manuscripta geodaetica*, 15:137–150, 1990.

[187] P.M. Khan, V.G. Halbe, K. Rajakumar, K.N. Manjunath, and K.C. Vora. Development and evaluation of exhaust brake systems for light commercial vehicle. In *SIAT 2005*. The Automotive Research Association of India, jan 2005.

[188] Y.A. Cengel and M.A. Boles. Thermodynamics: an engineering approach. *Sea*, 1000:8862, 2002.

[189] B. Bugbee and M. Blonquist. Absolute and relative gas concentration: understanding oxygen in air. *February*, 27:1–9, 2006.

[190] P.M. Frank. Analytical and qualitative model-based fault diagnosis – a survey and some new results. *European Journal of Control*, 2(1):6 – 28, 1996.

[191] H. Li, Y. Gao, P. Shi, and H. K. Lam. Observer-based fault detection for nonlinear systems with sensor fault and limited communication capacity. *IEEE Transactions on Automatic Control*, 61(9):2745–2751, Sept 2016.

[192] R. Isermann. *Supervision, fault-detection and fault-diagnosis methods – a short introduction*, pages 25–47. Springer Berlin Heidelberg, Berlin, Heidelberg, 2017.

[193] A. B. Youssef, S. K. El Khil, and I. Slama-Belkhodja. State observer-based sensor fault detection and isolation, and fault tolerant control of a single-phase pwm rectifier for electric railway traction. *IEEE Transactions on Power Electronics*, 28(12):5842–5853, Dec 2013.

[194] Z. Gao, C. Cecati, and S.X. Ding. A survey of fault diagnosis and fault-tolerant techniquespart i: Fault diagnosis with model-based and signal-based approaches. *IEEE Transactions on Industrial Electronics*, 62(6):3757–3767, 2015.

[195] Y.A. Zeldovich, D. Frank-Kamenetskii, and P. Sadovnikov. *Oxidation of nitrogen in combustion*. Publishing House of the Acad of Sciences of USSR, 1947.

[196] R. Miller, G. Davis, G. Lavoie, C. Newman, and T. Gardner. A super-extended Zel'dovich mechanism for NOx modeling and engine calibration. Technical report, SAE Technical Paper, 1998.

[197] S. dAmbrosio, R. Finesso, L. Fu, A. Mittica, and E. Spessa. A control-oriented real-time semi-empirical model for the prediction of NOx emissions in diesel engines. *Applied Energy*, 130:265–279, 2014.

[198] M. Kao and J. J. Moskwa. Turbocharged diesel engine modeling for nonlinear engine control and state estimation. *Journal of dynamic systems, measurement, and control*, 117(1):20–30, 1995.

[199] J. R. Hagena, Z. Filipi, and D. N. Assanis. Transient diesel emissions: analysis of engine operation during a tip-in. Technical report, SAE Technical Paper, 2006.

[200] I. Celikten, A. Koca, and M. A. Arslan. Comparison of performance and emissions of diesel fuel, rapeseed and soybean oil methyl esters injected at different pressures. *Renewable Energy*, 35(4):814 – 820, 2010.

[201] K. Ryu. Effects of pilot injection pressure on the combustion and emissions characteristics in a diesel engine using biodieselcng dual fuel. *Energy Conversion and Management*, 76:506 – 516, 2013.

[202] A. Norouzi, M. Aliramezani, and C. R. Koch. Diesel engine NOx reduction using a PD-type fuzzy iterativelearning control with a fast response NOx sensor. *Proceedings of Combustion Institute - Canadian Section , Spring 2019*, 2019.

Appendix A

Ph.D. Publications

A.1 Peer reviewed journal papers

1. M. Aliramezani, C.R. Koch, R.E. Hayes, and R. Patrick. Amperometric solid electrolyte NOx sensors the effect of temperature and diffusion mechanisms. Solid State Ionics, 313(Supplement C):7 - 13, 2017.
2. M. Aliramezani, C.R. Koch, and R. Patrick. Phenomenological model of a solid electrolyte NOx and O2 sensor using temperature perturbation for on-board diagnostics. Solid State Ionics, 321:62 68, 2018.
3. M. Aliramezani, C.R. Koch, M. Secanell, R.E. Hayes and R. Patrick. An electrochemical model of an amperometric NOx sensor. Sensors and Actuators B, 290: 302311, 2019.
4. M. Aliramezani, C. R. Koch and R. Patrick. A variable-potential limiting-current-type amperometric hydrocarbon sensor. IEEE SENSORS JOURNAL (under review).
5. M. Aliramezani, C. R. Koch, and R. Patrick. The effect of operating parameters of an amperometric NOx - O2 sensor on the sensor response. Symposium for Combustion Control, Aachen, 2019 (submitted to Solid State Ionics Journal).

A.2 Refereed conference papers

1. M. Aliramezani, C.R. Koch, and R.E. Hayes. Estimating tailpipe NOx concentration using a dynamic NOx/ammonia cross sensitivity model coupled to a three state control oriented SCR model. IFAC-PapersOnLine, 49(11):813, 2016.
2. K. Ebrahimi, M. Aliramezani, and C.R. Koch. An HCCI control oriented model that includes combustion efficiency. IFAC-PapersOnLine, 49(11):327332, 2016.
3. M. Aliramezani, K. Ebrahimi, C. R. Koch, R. E. Hayes. NOx sensor ammonia cross sensitivity analysis using a simplified physics based model. Proceedings of Combustion Institute Canadian Section (CICS), 2016.
4. M. Aliramezani, K. Ebrahimi, C. R. Koch, R. E. Hayes. Investigating the effect of temperature on NOx sensor cross sensitivity to ammonia using a physics based model. Proceedings of Combustion Institute Canadian Section (CICS),2017.
5. G. Symko, M. Aliramezani, C. R. Koch, R. E. Hayes. Axial insulation rings testing and simulation of pressure drop and temperature transients in engine exhaust catalysts. Proceedings of Combustion Institute - Canadian Section (CICS), 2018.
6. M. Aliramezani, A. Norouzi, and C. R. Koch. A control oriented diesel engine NOx emission model for on board diagnostics and engine control with sensor feedback. Proceedings of Combustion Institute - Canadian Section (CICS), 2019.
7. A. Norouzi, M. Aliramezani, and C. R. Koch. Diesel engine NOx reduction using a pd-type fuzzy iterative learning control with a fast response NOx sensor. Proceedings of Combustion Institute - Canadian Section, 2019.

Appendix B

Summary of test results

B.1 Sensor heat transfer test results

Table B.1: Sensor temperature test results at Engine off

(R_{PVS}) (Ω)	I_{P1} (mA)	**Sensor heater power (W)**	**Estimated temp. (K)**
100	3.241	20.89	1085.8
110	3.232	20.287	1077.9
120	3.222	19.81	1071.5
130	3.215	19.361	1065.4
150	3.199	18.66	1055.6
170	3.184	18.099	1047.6
190	3.166	17.608	1040.4
210	3.151	17.201	1034.3
230	3.135	16.862	1029.2
252	3.123	16.469	1023.2
270	3.111	16.286	1020.3
290	3.1	15.978	1015.4
310	3.091	15.753	1011.8
330	3.084	15.542	1008.4
200	3.151	17.253	1035.1
220	3.135	16.886	1029.6
240	3.122	16.577	1024.8
260	3.111	16.281	1020.2
300	3.088	15.818	1012.9
340	3.076	15.396	1006.1
380	3.065	15.072	1000.7
460	3.059	14.552	992.0
504	3.055	14.313	987.9
540	3.052	14.116	984.5
580	3.041	14.032	983.0
620	3.043	13.779	978.5
660	3.038	13.624	975.8

Table B.2: Sensor heat transfer test results at Diesel engine speed = 1500 rpm and Engine output torque = 200 lb.ft

(R_{PVS}) (Ω)	I_{P1} (mA)	**Sensor heater power (W)**
100	1.701	19.39
110	1.71	18.606
120	1.708	18.046
130	1.696	17.514
150	1.681	16.66
170	1.684	15.971
190	1.653	15.425
210	1.65	14.949
230	1.648	14.553
252	1.615	14.164
270	1.617	13.155
290	1.618	12.856
310	1.598	12.609
330	1.6	12.469
200	1.63	15.296
220	1.637	14.875
240	1.63	14.497
260	1.628	14.132
300	1.61	13.595
340	1.586	13.104
380	1.569	12.683
460	1.565	12.038
504	1.545	11.771
540	1.564	11.547
580	1.56	11.308
620	1.549	11.07
660	1.54	10.817

Table B.3: Sensor heat transfer test results at Diesel engine speed = 2000 rpm and Engine output torque = 100 lb.ft

(R_{PVS}) (Ω)	I_{P1} (mA)	**Sensor heater power (W)**
100	2.337	20.803
110	2.333	20.048
120	2.325	19.488
130	2.313	18.984
150	2.305	18.144
170	2.298	17.486
190	2.277	16.954
210	2.265	16.464
230	2.25	16.072
252	2.239	15.68
270	2.221	15.4
290	2.213	15.162
310	2.205	14.991
330	2.199	14.907
200	2.276	17.122
220	2.27	16.464
240	2.249	16.044
260	2.249	15.694
300	2.214	15.131
340	2.19	14.668
380	2.191	14.248
460	2.178	13.632
504	2.156	13.347
540	2.175	13.095
580	2.168	12.898
620	2.155	12.688
660	2.157	12.506

Table B.4: Sensor heat transfer test results at Diesel engine speed = 2500 rpm and Engine output torque = 30 lb.ft

(R_{PVS}) (Ω)	I_{P1} (mA)	**Sensor heater power (W)**
100	2.699	21.391
110	2.689	20.649
120	2.695	20.174
130	2.665	19.67
150	2.666	18.859
170	2.659	18.214
190	2.63	17.696
210	2.626	17.22
230	2.589	16.828
252	2.564	16.45
270	2.57	16.184
290	2.567	15.932
310	2.559	15.75
330	2.554	15.61
200	2.63	17.374
220	2.592	16.94
240	2.608	16.576
260	2.561	16.24
300	2.544	15.708
340	2.527	15.341
380	2.531	14.949
460	2.497	14.332
504	2.502	14.052
540	2.497	13.842
580	2.48	13.632
620	2.482	13.45
660	2.481	13.436

B.2 Second sensing cell test results

Table B.5: NO_x sensing cell potential vs current at Diesel engine speed = 1500 rpm and Engine output torque = 200 lb.ft. RPVS= 252 Ohms.

I_{P2} (μA)	V_{P2} (V)
0.589	0.293
0.876	0.343
1.037	0.395
1.132	0.446
1.213	0.5
1.331	0.55
1.613	0.6
2.337	0.65
4.061	0.7
6.881	0.75
0.21	0.239
-0.229	0.189
-1.783	0.139
-2.064	0.002

Table B.6: NO_x sensing cell potential vs current at Diesel engine speed = 2000 rpm and Engine output torque = 100 lb.ft. RPVS= 252 Ohms.

I_{P2} (μA)	V_{P2} (V)
0.247	0.292
0.404	0.343
0.48	0.396
0.534	0.447
0.569	0.499
0.646	0.55
0.82	0.6
1.354	0.65
2.691	0.7
5.064	0.75
0.06	0.24
-0.203	0.189
-1.349	0.138
-2.063	0.095
-2.062	0

Table B.7: NO_x sensing cell potential vs current at Diesel engine speed = 2500 rpm and Engine output torque = 30 lb.ft. RPVS= 252 Ohms.

I_{P2} (μA)	V_{P2} (V)
0.137	0.293
0.232	0.343
0.287	0.396
0.311	0.448
0.348	0.499
0.402	0.55
0.545	0.6
0.888	0.65
1.874	0.7
3.745	0.75
-0.027	0.24
-0.203	0.189
-1.265	0.138
-2.062	0.095
-2.06	0

Table B.8: NO_x sensing cell potential vs current at NO_x =2800 ppm. RPVS= 252 Ohms.

I_{P2} (μA)	V_{P2} (V)
-2.064	0
-2.064	0.002
-2.05	0.1
-1.508	0.139
-1.084	0.151
-0.537	0.165
-0.412	0.164
-0.189	0.169
-0.079	0.171
0.104	0.175
0.089	0.176
0.083	0.176
0.197	0.178
0.461	0.185
0.643	0.189
0.847	0.197
1.416	0.216
1.727	0.226
2.02	0.235
2.311	0.244
3.368	0.286
4.377	0.333
5.03	0.386
5.409	0.436

Table B.9: NO_x sensing cell potential vs current at NO_x =2200 ppm. RPVS= 252 Ohms.

I_{P2} (μA)	V_{P2} (V)
-2.064	0
-2.064	0.002
-2.05	0.1
-1.267	0.138
-0.409	0.159
-0.242	0.164
-0.179	0.166
-0.03	0.171
0.046	0.172
0.114	0.175
0.181	0.178
0.275	0.18
0.493	0.188
0.703	0.197
1.178	0.217
1.441	0.226
1.729	0.236
1.934	0.245
2.83	0.287
3.496	0.336
3.946	0.388
4.189	0.439

Table B.10: NO_x sensing cell potential vs current at NO_x =1800 ppm. RPVS= 252 Ohms.

I_{P2} (μA)	V_{P2} (V)
-2.064	0
-2.064	0.002
-2.05	0.1
-1.231	0.138
-0.373	0.159
-0.155	0.161
-0.215	0.166
-0.132	0.169
-0.101	0.171
-0.073	0.174
0.019	0.176
0.054	0.178
0.128	0.181
0.187	0.182
0.253	0.185
0.677	0.194
1.14	0.227
1.486	0.246
2.19	0.288
3.286	0.39
3.438	0.441

Table B.11: NO_x sensing cell potential vs current at NO_x =1310 ppm. RPVS= 252 Ohms.

I_{P2} (μA)	V_{P2} (V)
-2.064	0
-2.064	0.002
-2.05	0.1
-1.074	0.138
-0.369	0.159
-0.356	0.164
-0.172	0.171
-0.126	0.174
-0.091	0.176
-0.057	0.178
0.005	0.181
0.078	0.183
0.098	0.186
0.146	0.189
0.234	0.193
0.386	0.203
0.49	0.207
0.6	0.218
0.802	0.228
0.906	0.238
1.05	0.247
1.692	0.29
2.173	0.339
2.328	0.392
2.507	0.443

Table B.12: NO_x sensing cell potential vs current at NO_x =750 ppm. RPVS= 252 Ohms.

I_{P2} (μA)	V_{P2} (V)
-2.064	0
-2.064	0.002
-2.05	0.1
-1.015	0.137
-0.467	0.159
-0.428	0.164
-0.328	0.169
-0.215	0.176
-0.15	0.181
-0.094	0.187
-0.055	0.189
0.029	0.191
0.021	0.196
0.038	0.199
0.078	0.201
0.098	0.204
0.124	0.206
0.203	0.211
0.193	0.214
0.301	0.229
0.426	0.239
0.85	0.292
1.216	0.341
1.227	0.394
1.441	0.446

B.3 HC sensor test results

Table B.13: Transient sensor response at propane concentration = 5000 ppm. V_{P2}= 0.45 V, T=1023 K and V_S= 0.35 V.

Time (s)	I_{P1} (mA)
0	-0.006
10	-0.004
20	-0.006
30	-0.005
40	-0.01
50	-0.103
60	-0.15
70	-0.178
80	-0.193
90	-0.2
100	-0.201
110	-0.203
120	-0.223
130	-0.27
140	-0.332
150	-0.444
160	-0.628
170	-0.898
180	-1.241
190	-1.594
200	-1.922

Table B.14: Transient sensor response at propane concentration = 5000 ppm. V_{P2}= 0.45 V, T=1023 K and V_S= 0.425 V.

Time (s)	I_{P1} (mA)	Time (s)	I_{P1} (mA)
0	-0.003	330	-0.252
10	-0.004	340	-0.253
20	-0.002	350	-0.258
30	-0.002	360	-0.26
40	0.077	370	-0.265
50	-0.093	380	-0.269
60	-0.183	390	-0.276
70	-0.213	400	-0.284
80	-0.223	410	-0.293
90	-0.228	420	-0.305
100	-0.228	430	-0.318
110	-0.229	440	-0.335
120	-0.225	450	-0.357
130	-0.226	460	-0.381
140	-0.225	470	-0.417
150	-0.225	480	-0.458
160	-0.225	490	-0.504
170	-0.226	500	-0.566
180	-0.229	510	-0.638
190	-0.229	520	-0.729
200	-0.233	530	-0.839
210	-0.233	540	-0.981
220	-0.235	550	-1.158
230	-0.238	560	-1.363
240	-0.236	570	-1.595
250	-0.238	580	-1.851
260	-0.24	590	-2.128
270	-0.24	600	-2.418
280	-0.242	610	-2.708
290	-0.244	620	-2.986
300	-0.246	630	-3.251
310	-0.248	640	-3.497
320	-0.249	650	-3.717

Table B.15: Transient sensor response at propane concentration = 5000 ppm. V_{P2}= 0.45 V, T=1023 K and V_S= 0.672 V.

Time (s)	I_{P1} (mA)	Time (s)	I_{P1} (mA)
0	0	347.7	-0.206
10	-0.004	357.7	-0.206
20	-0.001	367.7	-0.208
30	-0.066	377.7	-0.204
40	-0.136	387.7	-0.205
50	-0.166	397.7	-0.21
60	-0.181	407.7	-0.208
70	-0.191	417.7	-0.212
80	-0.201	427.7	-0.217
90	-0.205	437.7	-0.22
100	-0.205	447.7	-0.223
127.7	-0.207	457.7	-0.229
137.7	-0.202	467.7	-0.234
147.7	-0.206	477.7	-0.242
157.7	-0.205	487.7	-0.244
167.7	-0.205	497.7	-0.254
177.7	-0.204	507.7	-0.262
187.7	-0.207	517.7	-0.267
197.7	-0.207	527.7	-0.277
207.7	-0.205	537.7	-0.284
217.7	-0.206	547.7	-0.302
227.7	-0.207	557.7	-0.313
237.7	-0.207	567.7	-0.33
247.7	-0.206	577.7	-0.348
257.7	-0.205	587.7	-0.373
267.7	-0.207	597.7	-0.399
277.7	-0.207	607.7	-0.432
287.7	-0.206	617.7	-0.464
297.7	-0.206	627.7	-0.508
307.7	-0.204	637.7	-0.551
317.7	-0.204	647.7	-0.602
327.7	-0.205	657.7	-0.66
337.7	-0.202	667.7	-0.728

Table B.16: Transient sensor response at propane concentration = 5000 ppm. V_{P2}= 0.45 V, T=1080 K and V_S= 0.82 V.

Time (s)	I_{P1} (mA)	Time (s)	I_{P1} (mA)
0	-0.004	320	-0.24
10	-0.003	330	-0.244
20	-0.054	340	-0.246
30	-0.154	350	-0.25
40	-0.187	360	-0.253
50	-0.202	370	-0.253
60	-0.214	380	-0.255
70	-0.22	390	-0.262
80	-0.228	400	-0.266
90	-0.23	410	-0.267
100	-0.229	420	-0.269
110	-0.23	430	-0.277
120	-0.23	440	-0.281
130	-0.234	450	-0.283
140	-0.229	460	-0.289
150	-0.23	470	-0.298
160	-0.233	480	-0.305
170	-0.23	490	-0.31
180	-0.228	500	-0.32
190	-0.229	510	-0.335
200	-0.231	520	-0.346
210	-0.229	530	-0.361
220	-0.229	540	-0.379
230	-0.229	550	-0.402
240	-0.229	560	-0.426
250	-0.231	570	-0.456
260	-0.23	580	-0.49
270	-0.235	590	-0.525
280	-0.236	600	-0.57
290	-0.237	610	-0.614
300	-0.239		
310	-0.238		

Table B.17: Transient sensor response at propane concentration = 5000 ppm. V_{P2}= 0.45 V, T=1023 K and V_S= 0.425 V.

Time (s)	I_{P1} (mA)	Time (s)	I_{P1} (mA)
0	-0.003	340	-0.253
10	-0.004	350	-0.258
20	-0.002	360	-0.26
30	-0.002	370	-0.265
40	0.077	380	-0.269
50	-0.093	390	-0.276
60	-0.183	400	-0.284
70	-0.213	410	-0.293
80	-0.223	420	-0.305
90	-0.228	430	-0.318
100	-0.228	440	-0.335
110	-0.229	450	-0.357
120	-0.225	460	-0.381
130	-0.226	470	-0.417
140	-0.225	480	-0.458
150	-0.225	490	-0.504
160	-0.225	500	-0.566
170	-0.226	510	-0.638
180	-0.229	520	-0.729
190	-0.229	530	-0.839
200	-0.233	540	-0.981
210	-0.233	550	-1.158
220	-0.235	560	-1.363
230	-0.238	570	-1.595
240	-0.236	580	-1.851
250	-0.238	590	-2.128
260	-0.24	600	-2.418
270	-0.24	610	-2.708
280	-0.242	620	-2.986
290	-0.244	630	-3.251
300	-0.246	640	-3.497
310	-0.248	650	-3.717
320	-0.249	660	-3.902
330	-0.252		

Table B.18: Transient sensor response at propane concentration = 5000 ppm. V_{P2}= 0.45 V, T=1009 K and V_S= 0.425 V.

Time (s)	I_{P1} (mA)	Time (s)	I_{P1} (mA)
0	-0.004	310	-0.227
10	-0.005	320	-0.228
20	-0.075	330	-0.228
30	-0.156	340	-0.232
40	-0.193	350	-0.231
50	-0.209	360	-0.234
60	-0.217	370	-0.239
70	-0.218	380	-0.244
80	-0.217	390	-0.249
90	-0.212	400	-0.255
100	-0.214	410	-0.265
110	-0.215	420	-0.274
120	-0.218	430	-0.288
130	-0.217	440	-0.306
140	-0.22	450	-0.326
150	-0.219	460	-0.352
160	-0.221	470	-0.382
170	-0.22	480	-0.418
180	-0.222	490	-0.459
190	-0.222	500	-0.512
200	-0.221	510	-0.576
210	-0.221	520	-0.656
220	-0.223	530	-0.757
230	-0.221	540	-0.883
240	-0.224	550	-1.032
250	-0.223	560	-1.209
260	-0.224	570	-1.414
270	-0.225	580	-1.66
280	-0.226	590	-1.942
290	-0.227	600	-2.253
300	-0.227		

Table B.19: Transient sensor response at propane concentration = 5000 ppm. V_{P2}= 0.45 V, T=1080 K and V_S= 0.67 V.

Time (s)	I_{P1} (mA)	Time (s)	I_{P1} (mA)
0	-0.004	367.7	-0.204
10	-0.001	377.7	-0.205
20	-0.066	387.7	-0.21
30	-0.136	397.7	-0.208
40	-0.166	407.7	-0.212
50	-0.181	417.7	-0.217
60	-0.191	427.7	-0.22
70	-0.201	437.7	-0.223
80	-0.205	447.7	-0.229
90	-0.205	457.7	-0.234
100	-0.207	467.7	-0.242
127.7	-0.202	477.7	-0.244
137.7	-0.206	487.7	-0.254
147.7	-0.205	497.7	-0.262
157.7	-0.205	507.7	-0.267
167.7	-0.204	517.7	-0.277
177.7	-0.207	527.7	-0.284
187.7	-0.207	537.7	-0.302
197.7	-0.205	547.7	-0.313
207.7	-0.206	557.7	-0.33
217.7	-0.207	567.7	-0.348
227.7	-0.207	577.7	-0.373
237.7	-0.206	587.7	-0.399
247.7	-0.205	597.7	-0.432
257.7	-0.207	607.7	-0.464
267.7	-0.207	617.7	-0.508
277.7	-0.206	627.7	-0.551
287.7	-0.206	637.7	-0.602
297.7	-0.204	647.7	-0.66
307.7	-0.204	657.7	-0.728
317.7	-0.205	667.7	-0.81
327.7	-0.202	677.7	-0.903
337.7	-0.206	687.7	-1.012
347.7	-0.206	697.7	-1.131
357.7	-0.208	707.7	-1.262

Table B.20: Transient sensor response at propane concentration = 5000 ppm. V_{P2}= 0.45 V, T=1023 K and V_S= 0.67 V.

Time (s)	I_{P1} (mA)	Time (s)	I_{P1} (mA)
0	-0.002	310	-0.205
10	-0.005	320	-0.207
20	-0.086	330	-0.208
30	-0.139	340	-0.214
40	-0.163	350	-0.22
50	-0.18	360	-0.22
60	-0.186	370	-0.225
70	-0.195	380	-0.229
80	-0.197	390	-0.236
90	-0.199	400	-0.242
100	-0.199	410	-0.247
110	-0.198	420	-0.25
120	-0.197	430	-0.257
130	-0.202	440	-0.265
140	-0.199	450	-0.277
150	-0.196	460	-0.288
160	-0.198	470	-0.298
170	-0.199	480	-0.313
180	-0.196	490	-0.33
190	-0.2	500	-0.347
200	-0.197	510	-0.369
210	-0.196	520	-0.397
220	-0.196	530	-0.42
230	-0.195	540	-0.455
240	-0.201	550	-0.491
250	-0.199	560	-0.532
260	-0.197	570	-0.577
270	-0.2	580	-0.627
280	-0.199	590	-0.689
290	-0.204	600	-0.756
300	-0.203		

Table B.21: Transient sensor response at propane concentration = 5000 ppm. V_{P2}= 0.45 V, T=1009 K and V_S= 0.67 V.

Time (s)	I_{P1} (mA)	Time (s)	I_{P1} (mA)
0	-0.004	360	-0.191
10	-0.007	370	-0.189
20	0.072	380	-0.192
30	-0.032	390	-0.192
40	-0.116	400	-0.192
50	-0.156	410	-0.194
60	-0.173	420	-0.194
70	-0.182	430	-0.197
80	-0.19	440	-0.197
90	-0.194	450	-0.202
100	-0.194	460	-0.206
110	-0.198	470	-0.208
120	-0.197	480	-0.215
130	-0.197	490	-0.219
140	-0.197	500	-0.223
150	-0.196	510	-0.231
160	-0.196	520	-0.237
170	-0.195	530	-0.244
180	-0.195	540	-0.253
190	-0.196	550	-0.262
200	-0.194	560	-0.277
210	-0.194	570	-0.291
220	-0.192	580	-0.31
230	-0.192	590	-0.331
240	-0.191	600	-0.359
250	-0.19	610	-0.392
260	-0.191	620	-0.428
270	-0.191	630	-0.476
280	-0.19	640	-0.528
290	-0.188	650	-0.586
300	-0.189	660	-0.653
310	-0.189	670	-0.725
320	-0.189	680	-0.811
330	-0.189	690	-0.902
340	-0.189	700	-0.997
350	-0.191		

Table B.22: Transient sensor response at propane concentration = 5000 ppm. V_{P2}= 0.45 V, T=1023 K and V_S= 0.82 V.

Time (s)	I_{P1} (mA)	Time (s)	I_{P1} (mA)
0	-0.004	310	-0.238
10	-0.003	320	-0.24
20	-0.054	330	-0.244
30	-0.154	340	-0.246
40	-0.187	350	-0.25
50	-0.202	360	-0.253
60	-0.214	370	-0.253
70	-0.22	380	-0.255
80	-0.228	390	-0.262
90	-0.23	400	-0.266
100	-0.229	410	-0.267
110	-0.23	420	-0.269
120	-0.23	430	-0.277
130	-0.234	440	-0.281
140	-0.229	450	-0.283
150	-0.23	460	-0.289
160	-0.233	470	-0.298
170	-0.23	480	-0.305
180	-0.228	490	-0.31
190	-0.229	500	-0.32
200	-0.231	510	-0.335
210	-0.229	520	-0.346
220	-0.229	530	-0.361
230	-0.229	540	-0.379
240	-0.229	550	-0.402
250	-0.231	560	-0.426
260	-0.23	570	-0.456
270	-0.235	580	-0.49
280	-0.236	590	-0.525
290	-0.237	600	-0.57
300	-0.239	610	-0.614

Table B.23: Transient sensor response at propane concentration = 5000 ppm. V_{P2}= 0.45 V, T=1009 K and V_S= 0.82 V.

Time (s)	I_{P1} (mA)	Time (s)	I_{P1} (mA)
0	-0.005	260	-0.217
10	-0.001	270	-0.216
20	-0.063	280	-0.224
30	-0.13	290	-0.224
40	-0.158	300	-0.231
50	-0.179	310	-0.238
60	-0.19	320	-0.241
70	-0.193	330	-0.247
80	-0.2	340	-0.253
90	-0.2	350	-0.262
100	-0.202	360	-0.27
110	-0.203	370	-0.279
120	-0.199	380	-0.287
130	-0.201	390	-0.298
140	-0.201	400	-0.316
150	-0.199	410	-0.325
160	-0.202	420	-0.346
170	-0.199	430	-0.365
180	-0.2	440	-0.389
190	-0.203	450	-0.413
200	-0.204	460	-0.441
210	-0.206	470	-0.474
220	-0.204	480	-0.513
230	-0.208	490	-0.552
240	-0.211	500	-0.597
250	-0.211	560	-0.426

Table B.24: Transient sensor response at propane concentration = 5000 ppm. V_{P2}= 0.45 V, T=990 K and V_S= 0.82 V.

Time (s)	I_{P1} (mA)	Time (s)	I_{P1} (mA)
0	-0.003	230	-0.199
10	-0.008	240	-0.196
20	-0.073	250	-0.204
30	-0.118	260	-0.199
40	-0.152	270	-0.204
50	-0.17	280	-0.218
60	-0.185	290	-0.223
70	-0.193	300	-0.228
80	-0.186	310	-0.228
90	-0.188	320	-0.239
100	-0.189	330	-0.239
110	-0.188	340	-0.258
120	-0.192	350	-0.263
130	-0.189	360	-0.287
140	-0.191	370	-0.306
150	-0.196	380	-0.326
160	-0.195	390	-0.355
170	-0.189	400	-0.396
180	-0.189	410	-0.438
190	-0.195	420	-0.494
200	-0.186	430	-0.554
210	-0.188	440	-0.62
220	-0.198		

Table B.25: Transient sensor response at propane concentration = 5000 ppm. V_{P2}= 0.22 V, T=1023 K and V_S= 0.425 V.

Time (s)	I_{P1} (mA)
0	-0.006
10	-0.005
20	-0.004
30	-0.118
40	-0.182
50	-0.208
60	-0.221
70	-0.224
80	-0.225
90	-0.227
100	-0.225
110	-0.224
120	-0.22
130	-0.223
140	-0.228
150	-0.229
160	-0.232
170	-0.232
180	-0.236
190	-0.239
200	-0.239
210	-0.244
220	-0.244
230	-0.252
240	-0.257
250	-0.263
260	-0.275
270	-0.289
280	-0.311
290	-0.343
300	-0.394
310	-0.476
320	-0.6
330	-0.773
340	-1.004
350	-1.315
360	-1.693
370	-2.139

APPENDIX C

SENSOR TEST RIG RELAYS LAYOUT

Table C.1: Sensor test rig relays layout (see Figure 3.16).

Actuator	Relay #
Valve 1	1 and 2
Valve 2	3 and 4
Valve 3	5 and 6
Valve 4	7 and 8
Valve 5	9 and 10
Valve 6	11 and 12
Tank A	13, 14 and 15
Tank B	16, 17 and 18
Tank C	19, 20 and 21
Tank D	22, 23 and 24